

國立交通大學

應用化學所

博士論文

藉由高分子氫鍵作用力的轉換來控制高分子薄膜表面
特性之研究



Tuning polymer surface free energy through mediating
polymer hydrogen bonding interaction

研究生：廖春雄

指導教授：張豐志 教授

中華民國九十八年三月

藉由高分子氫鍵作用力的轉換來控制高分子薄膜表面
特性之研究

Tuning polymer surface free energy through mediating
polymer hydrogen bonding interaction

研究生：廖春雄 Student：Chun-Hisung Liao

指導教授：張豐志 Advisor：Dr. Feng-Chih Chang

國立交通大學



Submitted to Institute of Applied Chemistry
College of Science
National Chiao Tung University
in partial Fulfillment of the Requirements
for the Degree of
Doctor of Philosophy
in
Applied Chemistry
March 2009
Hsinchu, Taiwan, Republic of China

中華民國九十八年三月

誌謝

轉眼間在新竹求學已經四年多了，這段日子真的是過的非常的快。回想起這段日子，最大的煩惱就是常常覺得不知何時可以畢業。但現在畢業了雖然有種如釋重負的感覺，卻也有種要離開熟悉環境的不捨。在這段求學路上我碰到了許許多多的願意教導我與幫助我的人，因為你們讓我可以順利的拿到博士學位，對於你們我永遠感念在心。

首先，我要感謝張豐志老師提供了這良好的研究環境，讓我可以專心追求自己有興趣的東西。也謝謝老師讓我知道學生不只要做好實驗以外更要懂得與人溝通跟合作這個做人處事的道理。對於老師的諄諄教誨我會永遠謹記在心。

感謝口試委員：林宏洲教授、李俊毅教授、陳建光教授、郭紹偉教授及王志逢教授在學生論文上提供了寶貴的意見與指導，使得學生論文可以更加豐富與完整。

感謝實驗室的畢業學長王志逢、林振隆的教導。感謝你們願意的傾囊相授教導我，引領我踏入這高分子領域。沒有你們，我想我現在還可能是在原地踏步迷失方向的人。更感謝王志逢學長願意擔任我口試委員在我學生生涯的最後指導我。也感謝寶寶與漢清願意常常與我這個固執的人討論並且給予幫忙。也謝謝婉君、懷廣、嘴巴最緊的 didi、倩婷、世堅、志豪、文騰、筱雯、sandy、仁志、宜弘、狗弟與徐婕。謝謝你們讓我的研究所生涯充滿歡笑與回憶。也感謝在工研院 L500 組的各位，雖然我常常裝死也每次遲到但是你們卻仍然沒有苛責過我，謝謝你們。

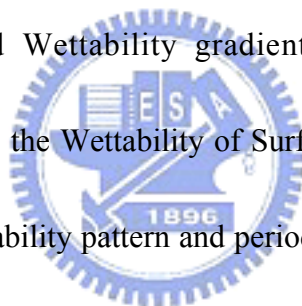
最後將這論文獻給我的家人，感謝父母親對我的栽培及家人的支持，讓我可以順利的完成學業。

謹以這份論文，獻給在我求學路上關心與照顧我的各位。

Outline of Contents

	Pages
Acknowledgments	
Outline of Contents	I
List of Schemes	VI
List of Tables	VI
List of Figures	VIII
Abstract (in Chinese)	XXIV
Abstract (in English)	XXVII
Chapter 1 Introduction	
1.1 Overview on Benzoxazines and Polybenzoxazines	1
1.2 Introduction to Polyhedral Oligomeric Silsesquioxane (POSS)	5
1.2.1 A quick history of Polyhedral Oligomeric Silsesquioxane (POSS)	5
1.2.2 Silsesquioxanes and Polyhedral Oligomeric Silsesquioxane (POSS)	6
1.2.3 POSS Polymers and Copolymers	9
References	10
Chapter 2 Introduction to Surface Free Energy Theory	
2.1 Surface Free Energy	13
2.1.1 Interfacial Thermodynamics	13

2.1.2 Contact Angle Equilibrium: Young Equation	15
2.1.3 Determination of Surface Free Energy	18
2.1.4 Surface Free Energy of Polymer	27
2.2 Superhydrophobic Surfaces	33
2.2.1 The Laws of Wetting	34
2.2.2 Natural Examples	37
2.2.3 Synthetic Substrates	41
2.2.4 Models	46
2.3 Wettability Pattern and Wettability gradient	51
2.3.1 Methods to Control the Wettability of Surface	51
2.3.2 Fabrication of wettability pattern and periodic array of colloid nanocrystals	60
References	67



Chapter 3 Modification of Polymer Substrates with Low Surface Free Energy

Material by Low-Temperature Curing Polybenzoxazine

Abstract	74
3.1 Introduction	75
3.2 Experiment section	76
3.2.1 Materials	76

3.2.2 Contact Angle Measurement	76
3.2.3 Thin-Film Formation and Polymerization	76
3.2.4 Polymer Thin-Film Formation	77
3.3 Results and Discussion	78
3.4 Conclusions	81
References	82
 Chapter 4 Tuning the Surface Free Energy of Polybenzoxazine Thin Films	
Abstract	95
4.1 Introduction	96
4.2 Experiment section	98
4.2.1 Materials	98
4.2.2 Contact Angle Measurement	98
4.2.3 Fourier Transform Infrared (FTIR) Spectroscopy	98
4.2.4 Ultraviolet Irradiation Exposure	99
4.2.5 Electron Spectroscopy for Chemical Analysis (ESCA)	99
4.2.6 Thin-Film Formation and Polymerization	99
4.2.7 Periodic Arrangement of Arrays of CdTe Colloidal Nanocrystals	99
4.3 Results and Discussion	101
4.4 Conclusions	104



References	105
------------	-----

Chapter 5 Fabrication of patterned superhydrophobic Polybenzoxazine-hybrid surfaces

Abstract	118
----------	-----

5.1 Introduction	119
------------------	-----

5.2 Experiment section	121
------------------------	-----

5.2.1 Materials	121
-----------------	-----

5.2.2 Contact Angle Measurement	121
---------------------------------	-----

5.2.3 Fourier Transform Infrared (FTIR) Spectroscopy	121
--	-----

5.2.4 Ultraviolet Irradiation Exposure	122
--	-----

5.2.5 Electron Spectroscopy for Chemical Analysis (ESCA)	122
--	-----

5.2.6 Atomic Force Microscopy (AFM)	122
-------------------------------------	-----

5.2.7 Preparation of polybenzoxazine thin film and superhydrophobic superhydrophobic polybenzoxazine-silica hybrid surface	123
--	-----

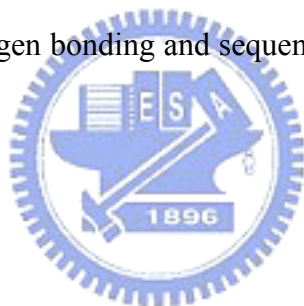
5.3 Results and Discussion	124
----------------------------	-----

5.4 Conclusions	128
-----------------	-----

References	129
------------	-----

Chapter 6 Effect of Molecule Weight and Hydrogen Bonding on Low-Surface-Energy Material of Poly(vinylphenol)

Abstract	143
6.1 Introduction	144
6.2 Experiment section	146
6.2.1 Preparation of PVPh/PMMA Random and Block Copolymers and Blends	146
6.3 Characterizations	147
6.4 Results and Discussion	148
6.4.1 The effect of molecule weight on surface free energy in PVPh system	148
6.4.2 The effect of hydrogen bonding and sequence distribution in PVPh/PMMA system	149
6.5 Conclusions	155
References	156



Chapter 7 Effect of POSS Nanoparticle on Surface Free Energy and Phase

Behavior

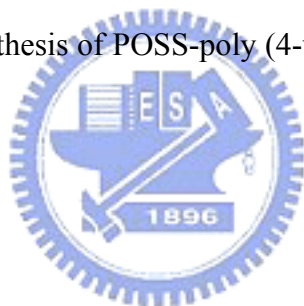
Abstract	170
7.1 Introduction	171
7.2 Experiment section	173
7.2.1 Preparation of PVPh/POSS Block Copolymers and Blends	173
7.3 Characterizations	175

7.4 Results and Discussion	176
7.4.1 The effect of POSS nanoparticle on surface free energy in PVPh system	176
7.4.2 The effect of POSS nanoparticle on phase behavior in POSS-PVPh copolymer	177
7.5 Conclusions	180
References	181
Chapter 8 Conclusions	193
List of Publications	195



List of Schemes

	Pages
Scheme 1-1. The syntheses and thermal curing of (A) monofunctional benzoxazines and (B) difunctional benzoxazines	2
Scheme 4-1. Preparation of the allylamine-based benzoxazine monomer	111
Scheme 4-2. Mechanism of the B-ala photo-oxidation	112
Scheme 4-3. Fabrication of wettability gradients and wettability patterns on B-ala polybenzoxazine films	113
Scheme 7-1. Procedure of synthesis of POSS-poly (4-vinyl phenol) copolymer	184



List of Tables

	Pages
Table 1-1. Comparative polybenzoxazine properties of various high performance polymers	4
Table 2-1. Numerical constant for molecular weight dependence of surface free energy	28
Table 2-2. Macleod's exponent for some polymers	30
Table 3-1. Advancing contact angles for water, ethylene glycol and diiodomethane and their corresponding surface free energy of B-ala and B-ala/AIBN	

polybenzoxazine films	83
Table 3-2. Fraction of hydrogen bonding of B-ala/AIBN=5:1 PBZ film cured at 120 °C for 2, 4, 8, and 24 h	84
Table 3-3. The advancing contact angle for water, ethylene glycol and diiodomethane of poly(4-vinyl phenol), poly(4-vinyl pyridine) and polycarbonate substrates before and after modification with B-ala/AIBN=5/1 PBZ thin film cured 8 h at 120 °C	85
Table 4-1. Advancing contact angles for water, ethylene glycol and diiodomethane and corresponding surface free energies of B-ala PBZ films after thermal curing	108
Table 4-2. Advancing contact angles for water, ethylene glycol and diiodomethane and corresponding surface free energies of B-ala PBZ Films cured for 2 h at 210°C and then subjected to UV exposure	109
Table 4-3. Surface free energy and ESCA analysis of B-ala PBZ Films cured for 2 h at 210°C and the subjected to UV exposure	110
Table 5-1. Contact angle and ESCA oxygen content of B-ala PBZ thin film and super-hydrophobic polybenzoxazine-silica hybrid surface with different UV exposure time.	132
Table 6-1. Formulations and thermal properties of PVPh-co-PMMA copolymers and corresponding Blends	159

Table 6-2. Results of the curve-fitting data for PVPh- <i>co</i> -PMMA and PVPh/PMMA blends with different process at room temperature	160
Table 6-3. Root-mean-square surface roughness, advancing contact angle for water and diiodomethane and surface free energy of PVPh/PMMA Copolymers	161
Table 7-1. Characterization, root-mean-square surface roughness, advancing contact angle for water and diiodomethane and surface Free energy of POSS-PVPh Copolymers	185
Table 7-2. Root-mean-square surface roughness, advancing contact angle for water and diiodomethane and surface free energy of POSS/PVPh Blends.	186



List of Figures

	Pages
Figure 1-1. Plot of the number of POSS publications versus the year	6
Figure 1-2. Structures of silsesquioxanes	7
Figure 1-3. Structures of polyhedral oligomeric silsesquioxane (POSS)	8
Figure 2-1. Work of adhesion	14
Figure 2-2. Work of cohesion	14
Figure 2-3. Contact angle equilibrium on a smooth, homogeneous, planar, and rigid	

Surface	15
Figure 2-4. Advancing contact angle	16
Figure 2-5. Receding contact angle	17
Figure 2-6. Zisman plot for poly(tetrafluoroethylene) (PTFE) using various testing liquids	25
Figure 2-7. Process of adhesion force measurement	26
Figure 2-8. Force-distance curve and adhesion force	27
Figure 2-9. Comparison of surface energy and molecular weight between polymers with and without hydrogen bonds	29
Figure 2-10. Linear additivity of surface tension of random copolymers of ethylene oxide and propylene oxide, and surface-active behavior of blends of poly(ethylene oxide) (PEG 300) and poly(propylene oxide) (PPG 425)	31
Figure 2-11. Surface tension versus composition for ABA block copolymers of ethylene oxide (A block) and propylene oxide (B block). Degree of polymerization are (1) DP = 16, (2) DP = 30, (3) DP = 56.	32
Figure 2-12. Surface tension of blends of compatible homopolymers (1) poly(ethylene oxide) (PEG 300) + poly(propylene oxide) (PPG 425), (2) PPG 2025 + polyepichlorohydrin (PECH 1500), (3) PPG 400 + PECH 2000.	33

Figure 2-13. Liquid droplet on a solid. The liquid contacts the solid over a zone of size ℓ , and joins it at an angle θ . 35

Figure 2-14. Displacing the contact line by a quantity dx (keeping the drop volume unchanged) modifies the surface area of each interface (solid/liquid, solid/vapor, liquid/vapor) 35

Figure 2-15 Water droplets on lotus 38

Figure 2-16. SEM picture of a super-hydrophobic plant. The surface is structured at two levels: bumps at a scale of $20\ \mu\text{m}$ and hairs at a scale of $1\ \mu\text{m}$. These structures together with the wax which coats the leaf provide super-hydrophobicity 38

Figure 2-17. The non-wetting leg of a water strider. (a) Typical side view of a maximal-depth dimple ($4.38\ \text{mm}$) just before the leg pierces the water surface. Inset, water droplet on a leg; this makes a contact angle of 167.6° . (b), (c), Scanning electron microscope images of a leg showing numerous oriented spindly microsetae (b) and the fine nanoscale grooved structures on a seta (c). Scale bars: b, $20\ \mu\text{m}$; c, $200\ \text{nm}$ 40

Figure 2-18. FE-SEM micrograph of the wing surface of *Cicada orni* with regularly aligned nanoposts 40

Figure 2-19. The water-capturing surface of the fused overwings (elytra) of the desert

beetle *Stenocara* sp. (a) Adult female, dorsal view; peaks and troughs are evident on the surface of the elytra. (b) A ‘bump’ on the elytra, stained with Red O for 15 min and then with 60% isopropanol for 10 min, a procedure that tests for waxes. Depressed areas of the otherwise black elytra are stained positively (waxy, coloured), whereas the peaks of the bumps remain unstained (wax-free; black). (c) Scanning electron micrograph of the textured surface of the depressed areas. Scale bars, (a) 10 mm; (b) 0.2 mm; (c) 10 μ m

41

Figure 2-20. SEM images of the fractal alkylketene dimmer (AKD) surface: (a) top view, (b) cross section. Water droplet on AKD surfaces: (c) fractal AKD surface; (d) flat AKD surface.



43

Figure 2-21. The profile of a water drop on (a) a smooth i-PP surface ($CA = 104^\circ$), (b) a superhydrophobic i-PP coating on a glass slide ($CA = 160^\circ$). (c) SEM picture of a superhydrophobic i-PP film

44

Figure 2-22. (a) Illustration of the solvent effect on the morphologies of PP-PMMA copolymer surface. (b) The profile of a water drop on superhydrophobic polymer surface. (c) SEM images of superhydrophobic polymer. (d) Enlarged view of (c)

44

Figure 2-23. SEM images of (a) surface of the PAN nanofibers; (b) cross-sectional

view of the as-synthesized PAN nanofibers. Shapes of water droplets on
(c) the PAN nanofibers with a rough surface; (d) the native PAN film
with smooth surface 45

Figure 2-24. The Wenzel state: the liquid follows the solid surface. 46

Figure 2-25. The Cassie state, the liquid only contacts the top of the asperities, leaving
air below 48

Figure 2-26. Millimetric water drops (of the same volume) deposited on a superhydro-
phobic substrate consisting of dilute pillars ($f_1 = 0.01$). (a) The right drop
has been pressed, which induced a Wenzel state, characterized by a
smaller angle (the roughness is very low, and equal to 1.1). The light
passes below the left drop, indicating a Cassie state. (b) Ten minutes
later, the drop volumes have decreased, owing to evaporation, and angles
became receding ones. The difference of hysteresis between both states is
clearly visible: the Wenzel drop even became hydrophilic 49

Figure 2-27. (a, b) FE-SEM top-images of the as-prepared ZnO nanorod films at low
and high magnifications, respectively. (c) Cross-sectional view of the
aligned ZnO nanorods. (d) XRD pattern of the as-synthesized nanorod
films. (e) Reversible super-hydrophobic-super-hydrophilic transition of
the as-prepared films under the alternation of UV irradiation and dark

storage. (f) Photographs of water droplet shape on the aligned ZnO nanorod films before (left) and after (right) UV illumination. 54

Figure 2-28. (a) Fabrication and (b) Reversible photoisomerization of a roughness-enhanced photoswitchable surface (c) photographs of substrates with patterned extreme wetting properties; angled views of water droplet profiles on the patterned substrate as a result of selective UV irradiation. (d) The relationships between the number of deposition cycles and the water contact angles: water droplet profiles on the smooth substrate (dotted arrows) and on the (PAH/SiO₂)₉ multilayer film (solid arrows) after UV/visible irradiation. (e) Reversible wettability transitions of a smooth substrate (□) and a (PAH/SiO₂)₉ multilayer film (■) 55

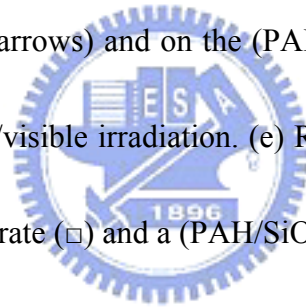


Figure 2-29. Surface-roughness-enhanced wettability of a PNIPAAm-modified surface. (a) The relationships between groove spacing (D) of rough surfaces and the water CAs at low temperature (triangles, 25 °C) and at high temperature (squares, 40 °C). The groove spacing of ∞ represents flat substrate. (b) Water drop profile for thermally responsive switching between superhydrophilicity and superhydrophobicity of a PNIPAAm-modified rough surface with groove spacing of about 6 μm, at 25 °C and 40 °C. The water CAs are about 0° and 149.3±2.5°,

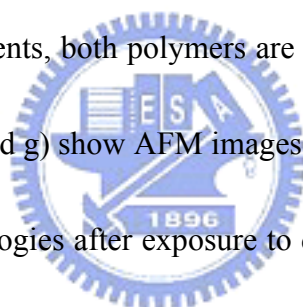
respectively. (c) Temperature (T) dependences of water CAs for PNIPAAm thin films on a rough substrate with groove spacing of about 6 μm (triangles) and on flat substrate (squares). (d) Water CA in at two different temperatures for a PNIPAAm-modified rough substrate with groove spacing of 6 μm 56

Figure 2-30. Typical comparison of SEM images of the colloidal crystal film assembly at different pH values. (a, b) Top view and side view of the films assembled at pH = 6.0. (c, d) Top view and side view of the film assembled at pH = 12.0. (Inset: typical TEM image of core-shell spheres of poly-(St-MMA-AA); the bar is 100 nm. (e) Photographs of water droplet shape on the films assembled from suspensions with pH of 6.0 and 12 and illustrations of the structure of the latex sphere in the films 57

Figure 2-31. Idealized representation of the transition between straight (hydrophilic) and bent (hydrophobic) molecular conformations (ions and solvent molecules are not shown). The precursor molecule MHAE, characterized by a bulky end group and a thiol head group, was synthesized from MHA by introducing the (2-chlorophenyl)diphenylmethyl ester group 58

Figure 2-32. Two-level structure of self-adaptive surfaces (SAS): Schematic representation of needlelike surface morphology of the PTFE surface

(first level) (a) and SEM image of the PTFE film after 600 s of plasma etching (b). Each needle is covered by a covalently grafted mixed brush that consists of hydrophobic and hydrophilic polymers (second level) depicted schematically in panels c-e. Its morphology results from interplay between lateral and vertical phase segregation of the polymers, which switches the morphology and surface properties upon exposure to different solvents. In selective solvents the preferred polymers preferentially occupies the top of the surface (c and e), while in nonselective solvents, both polymers are present in the top layer (d). The lower panels (f and g) show AFM images (model smooth substrate) of the different morphologies after exposure to different solvents



59

Figure 2-33. Colloidal particles assembled on 50 μm carboxylic acid terminated square patterned surfaces on a continuous methylterminated surface at pH=2, 24.5°C, 21% humidity. (a) An optical micrograph of 0.8 μm amidine functionalized microspheres deposited at 0.1% volume fraction. (b) SEM image. (c) An SEM image of 0.8 μm microspheres assembled on a surface patterned with alternating 5 μm carboxylic acid terminated stripes and 5 μm methyl terminated stripes at pH=2, 24.5 °C, 21% humidity, and 0.01% volume fraction

62

Figure 2-34. (a), (b) LVSEM image at higher magnification showing the stepwise increase of the thickness from the edge to the center of the stripe. (c) LVSEM image of the topmost layer showing the excellent crystal quality. (d) LVSEM image of the cross-section through a colloidal crystal stripe

63

Figure 2-35. (a) SEM Images of the gold photonic crystal structures, (b) AFM height image of the gold photonic crystal structures, (c) AFM phase image of the gold photonic crystal structures, (d) Measurements of contact angles of water on the ITO and on the PR surfaces: $\theta = 44-45^\circ$, $\theta = 73-75^\circ$. (e) Mechanisms for the confinement of the gold nanoparticles into the grating grooves when the PR channel is small enough. (f) Two gaps will form for structures with large PR channel

64

Figure 2-36. (a) Illustration of creating the photopatterned monolayer, (b) illustration of the UV-induced reaction of SAM **6** and (c) AFM image of the photopatterned monolayer surface. (d) AFM image of the UV-patterned HD-UV-PA-modified surface after drop-casting SWCNTs form a H₂O/methanol solution (3:1 volume). The higher resolution images on the left and right illustrate the high selectivity of the deposition

65

Figure 2-37. (a) Fabrication of a biomimetic dual-scale hierarchical structure by

direct UV-replica molding with the template and (b) fabrication of selectively wetting surface (c) SEM and AFM image of the template with dual-scale roughness (d) selective wetting of water on the DUV-modified surface obtained with a SUS mask	66
Figure 3-1. The ^1H NMR spectrum of B-ala monomer	86
Figure 3-2. The ^{13}C NMR spectrum of B-ala monomer	87
Figure 3-3. The Mass spectrum of B-ala monomer	88
Figure 3-4. DSC diagram of B-ala and B-ala/AIBN molar ratio = 5:1	89
Figure 3-5. DSC diagram of B-ala and B-ala/phenol molar ratio = 5:1	90
Figure 3-6. FTIR spectra of B-ala and B-ala/AIBN PBZ film. (a) B-ala, (b) B-ala and B-ala/AIBN = 5:1 cured at 120 °C, (c) B-ala and B-ala/AIBN = 5:1 cured at 120 °C, and (d) B-ala and different molar ratio of B-ala/AIBN cured for 8h at 120°C	91
Figure 3-7. Curve fitting for the FTIR spectra of B-ala/AIBN=5:1 PBZ film cured at 120 °C for (a) 2, (b) 4, (c) 8, and (d) 24 h	92
Figure 3-8. Surface free energy of B-ala and B-ala with different molar ratio of AIBN cured at 120°C	93
Figure 3-9. The advancing contact angle for water, ethylene glycol, and diiodomethane of (a) poly(4-vinyl pyridine) thin film (b) modified with	

Figure 4-1. Advancing contact angles of (●)water, (▲)diiodomethane, and (▼)ethylene glycol and the respective surface free energies (γ_s) (■) of B-ala PBZ films 114

Figure 4-2. Curve fitting of the FTIR spectra of B-ala P BZ films cured at 210 °C for (a) 1, (b) 2, (c) 4, and (d) 8 h 115

Figure 4-3. Water drops on (a) wettability pattern, (b) wettability gradient B-ala PBZ films 116

Figure 4-4. Fluorescence microscope images of periodic arrangement of arrays of CdTe Colloidal nanocrystals on line patterned PBZ thin film in a magnification of (a)200 (b)400 (c)600 and square patterned PBZ thin film in a magnification of (a)200 (b)400 (c)600 117

Figure 5-1. FTIR spectrum and structure of (a) B-ala monomer (b) the unirradiated B-ala polybenzoxazine (c) the B-ala polybenzoxazine irradiated for 60min and (d) the difference spectrum of (b) and (c) 133

Figure 5-2. C(1s) ESCA spectrum of B-ala polybenzoxazine thin film cured 1h at 210°C with different UV exposure time (a) 0min (b) 5min (c) 10min (d) 20min (e) 40min (f) 60min 134

Figure 5-3. C(1s) ESCA spectrum of (a) phenol (b) 1, 4-benzoquinone (c) 1,

4-benzoquinone mix with phenol at molar ratio of 2:1 (d) B-ala polybenzoxazine thin cured at 210°C for 1h (e) d after 60min UV exposure 135

Figure 5-4. O(1s) ESCA spectrum of (■) 1, 4-benzoquinone (◆) 1, 4-benzoquinone mix with phenol at molar ratio of 2:1 (▲) B-ala polybenzoxazine thin film(cured at 210°C for 1h (▼) B-ala polybenzoxazine thin film (cured at 210°C for 1h) after 60min UV exposure 136

Figure 5-5. Water contact angles for (■) polybenzoxazine thin films and (●) superhydrophobic polybenzoxazine-silica hybrid surfaces with different UV exposure time 137



Figure 5-6. SEM image and their corresponding contact angle of (a) polybenzioxazine-silica hybrid surface (b) polybenzioxazine-silica hybrid surface modified with 0.1% pure B-ala polybenzoxazine thin film (c) b after 60min UV irradiation (d) c wash with acetone and methanol. 138

Figure 5-7. AFM images of (a) polybenzioxazine-silica hybrid surface (b) polybenzoxazine- silica hybrid surface modified with 0.1% pure B-ala polybenzoxazine thin film (c) b after 60min UV irradiation 139

Figure 5-8. AFM images with different UV exposure time (a) 0min (b) 20min (c) 40min (d) 60min 140

Figure 5-9. (a) Water drops on selective wetting polybenzoxazine-silica hybrid surface (b) CdTe quantum dot containing solution drops on the UV-modified polybenzoxazine-silica hybrid surface obtained with a LUV mask. Shapes of $5\mu\text{l}$ water droplets on the superhydrophobic polybenzoxazine -silica hybrid surface after 5min UV exposure with different tilt angles (c) 180° (d) 90° 141

Figure 5-10. Transfer Process of a water droplet from a superhydrophobic surface to a hydrophilic one 142

Figure 6-1. Surface energy of PVPh homopolymers with different molecule weight (■) at room temperature and (●) after 180°C thermal treatment process 162

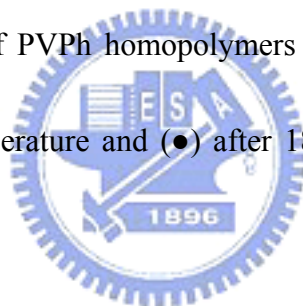


Figure 6-2. The FTIR spectra of pure PVPh homopolymer ($M_w = 9697$) (a) solvent casting (b) spin coating (c) 180°C 24h thermal treatment 163

Figure 6-3. The FTIR spectra of samples having similar PVPh contents preparing by different coating process (a) 、(b) solvent casting and (c) 、(b) spin coating 164

Figure 6-4. FTIR spectra of (a) 、(b) PVPh/PMMA blends, (c) 、(d) PVPh-b-PMMA copolymers and (e) 、(f) PVPh-r-PMMA copolymers at room temperature 165

Figure 6-5. FTIR spectra of (a) 、(b) PVPh/PMMA blends, (c) 、(d) PVPh-b-PMMA copolymers and (e) 、(f) PVPh-r-PMMA copolymers after the 180°C thermal treatment procedure 166

Figure 6-6. FTIR spectra of (a) PVPh/PMMA blends, (b) PVPh-b-PMMA copolymers and (c) PVPh-r-PMMA copolymers in 2800cm⁻¹~3800cm⁻¹ 167

Figure 6-7. FTIR spectra of (a) PVPh/PMMA blends, (b) PVPh-b-PMMA copolymers and (c) PVPh-r-PMMA copolymers 1660cm⁻¹~1800cm⁻¹ 168

Figure 6-8. Surface energy of PVPh/PMMA random copolymers (▲), block copolymers (●) and their blends (■) (a) before (b) after the thermal treatment process 169

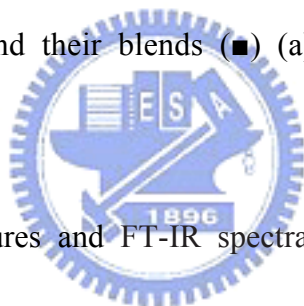


Figure 7-1. Chemical structures and FT-IR spectra of (a)T7-POSS, (b)POSS-Cl, (c)POSS-PAS copolymer and (d) POSS-PVPh copolymer 187

Figure 7-2. ¹H NMR spectra of (a)T7-POSS, (b)POSS-Cl, (c)POSS-PAS copolymer and (d) POSS-PVPh copolymer 188

Figure 7-3. Transmission electron micrographs of POSS-PVPh in acetonitrile solution (a) POSS-PVPh₉, (b) POSS-PVPh₃₅, (c) POSS-PVPh₁₂₀ and (d) POSS-PVPh₂₆₄ 189

Figure 7-4. Transmission electron micrographs of POSS-PVPh₁₂₀ in different solution (a) 0.1ml toluene + 4.0ml THF, (b) 0.5ml toluene + 4.0ml THF,

(c) 1ml toluene + 4.0ml THF and (d) 2ml toluene + 4.0ml THF 190

Figure 7-5. Transmission electron micrographs of POSS-PVPh₁₂₀ in acetonitrile at different concentrations: (a) 0.5 mg/mL, (b) 1.0 mg/mL, (c) 2.0 mg/mL, (d) 4.0 mg/mL and (e) 8.0 mg/ml 191

Figure 7-6. SEM image and corresponding water contact angle of POSS-PVPh superhydrophobic surface 192



摘要

本論文中以討論高分子氫鍵作用力及多面體聚矽氧烷奈米粒子對於高分子薄膜表面特性的為主體，分為五大主題：

1. 利用低溫交聯的 Polybenzoxazine 薄膜去修飾高分子薄膜表面

在我們以前的研究發現 Polybenzoxazine 薄膜為一低表面能材料，可以用來修飾無機固體表面如金屬、玻璃或矽晶圓等等。但是對於高分子材料其熱交聯製程溫度太高因此無法去修飾高分子表面。在本章中我們發現 AIBN 此自由基起始劑在 120°C 製程下由於起始劑化學鍵斷鍵所產生的熱能可以產生一些寡聚物，而這些寡聚物會對熱交聯反應產生催化效果。因此我們利用此低溫製程成功的修飾高分子基材，使的這些高分子表面也具有低表面能特性。

2. 控制 Polybenzoxazine 薄膜表面能之研究

Polybenzoxazine 薄膜由於具有極強的高分子內氫鍵而擁有極低的表面能，我們利用了熱與紫外光這兩種方式來控制 Polybenzoxazine 薄膜中分子內與分子間作用力的比例。藉由這兩種方式我們可以輕易的控制 Polybenzoxazine 薄膜的表面能。此外，我們更利用紫外光照時間與區域的不同在 Polybenzoxazine 薄膜上製造親疏水性圖案的陣列與梯度。並且成功的製造出銻化鎘量子點的規則陣列。

3. 製造擁有超疏水及超親水特性的 Polybenzoxazine 有機無機混成表面

我們利用混摻二氧化矽奈米粒子提高表面粗糙度以製造具有蓮花效應的超疏水表面。再利用紫外光照讓某些特定區域形成超親水的表面，藉此我們可以得到同時具有超疏水及超親水兩種極端特性的表面。此外，在紫外光照後我們發現表面對於水滴產生極強的吸附力。我們將表面光照後產生的此特性應用在能轉移微小水滴的機械手臂上。此外我們更利用表面分析化學分析影像能譜儀對光照後的表面化學組成改變作更深入的探討。

4. 分子量及高分子氫鍵作用力對於低表面能材料 Poly(4-vinyl phenol)表面特性

影響之探討

在我們先前研究發現 Poly(4-vinyl phenol) 為一低表面能材料。在此章中我們更深入的探討分子量、多面體聚矽氧烷奈米粒子及高分子氫鍵作用力對於 Poly(4-vinyl phenol) 高分子薄膜表面特性的影響。為了探討高分子氫鍵的影響我們合成了不同比例的 Poly(4-vinyl phenol)/Poly(methyl methacrylate) 團塊塊體共聚合物及不規則共聚合物。在其中我們發現 Poly(4-vinyl phenol)/Poly(methyl methacrylate) 團塊塊體共聚合物及不規則共聚合物系統不同於混摻系統呈現非常低的表面能，這是因為團塊塊體共聚合物及不規則共聚合物系統在熱處理在快速冷卻的過程中降低了分子間的作用力。而混摻系統雖然也降低了 Poly(4-vinyl phenol) 之間的分子作用力卻也增加了 Poly(4-vinyl phenol) 與 Poly(methyl methacrylate) 分子鏈之間的作用力。所以混摻系統的表面能會隨著 Poly(methyl

methacrylate)的含量增加而增加。

5. 多面體聚矽氧烷奈米粒子對於 poly(4-vinyl phenol)表面特性與溶液相行為影響之探討

多面體聚矽氧烷奈米粒子本身為一具有低表面能的奈米粒子，所以不管當我們是混摻或是接枝上去 poly(4-vinyl phenol)此種高分子上面，我們均發現隨著多面體聚矽氧烷奈米粒子的量越多，高分子薄膜的表面能降的越低。此外我們也發現在末端帶有多面體聚矽氧烷奈米粒子的 Poly(4-vinyl phenol) 團塊塊體共聚合物在溶液中呈現非常獨特的自組裝行為。



Abstract

In this study, we focus on four major subjects which based on the effect of hydrogen bonding and POSS nanoparticle on surface free energy:

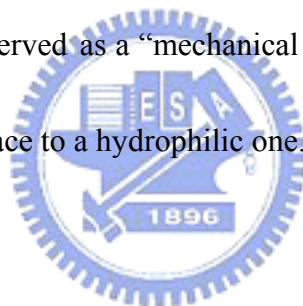
1. Tuning the Surface Free Energy of Polybenzoxazine Thin Films

A novel approach to manipulate the surface free energy and wettability on polybenzoxazine thin films can be achieved simply by varying time of thermal treatment or UV exposure. Fraction of the intramolecular hydrogen bonding of the as cured sample will convert into intermolecular hydrogen bonding upon thermal treatment or UV exposure and thus results in increase of hydrophilicity and wettability. This UV approach provides a simple method to generate wettability patterns or wettability gradients on the surface of polybenzoxazine film. In addition, we have applied this technique to the preparation of a large-area periodic array of CdTe colloidal nanocrystals on polybenzoxazine thin films.

2. Fabrication of patterned superhydrophobic Polybenzoxazine-hybrid surfaces

The hydrophilicity of B-ala PBZ film and superhydrophobic

polybenzoxazine-hybrid surface can be controlled through UV exposure to change ratio of intra- to intermolecular hydrogen bonds. Fraction of the intramolecular hydrogen bonding of the as cured sample will convert into intermolecular hydrogen bonding upon UV exposure and thus results in increase of hydrophilicity. This simple method allows for manipulating the hydrophilicity at selected regions on superhydrophobic polybenzoxazine-hybrid surface to create patterned surface with superhydrophobic and superhydrophilic regions. Besides, we have found that the superhydrophobic polybenzoxazine-silica hybrid surface exhibits good adhesion of water droplets after UV exposure which can be served as a “mechanical hand” to transfer water droplets from a superhydrophobic surface to a hydrophilic one.



3. Effect of Molecule Weight, Nanoparticle and Hydrogen Bonding on Low-Surface-Energy Material of Poly(vinylphenol)

We discovered that a series of poly(vinylphenol-*co*-methylmethacrylate) (PVPh-*co*-PMMA) block and random copolymers possess extremely low surface energy after a simple thermal treatment procedure, even lower than that of poly(tetrafluoroethylene) (22.0 mJ/m^2) calculated on the basis of the two-liquid geometric method. Besides, the effects of molecule weight and nanoparticle on surface free energy were investigated carefully in this chapter. The decrease of the

intermolecular hydrogen-bonding fraction between hydroxyl groups of PVPh in PVPh/PMMA systems through a simple thermal treatment procedure tends to decrease the surface energy and the sequence distribution of the vinylphenol group in PVPh-*co*-PMMA copolymers plays an important role in dictating the final surface energy after thermal treatment.

4. Modification of Polymer Substrates with Low Surface Free Energy Material by Low-Temperature Curing Polybenzoxazine

The B-ala/AIBN PBZ system has a higher extent of the ring-opening of oxazine because phenol-containing oligomers are formed at the early stage of the curing process. As a result, the B-ala/AIBN PBZ system possesses a relatively stronger intramolecular hydrogen bonding and lower surface energy than the pure B-ala system at low temperature curing. In this context, Poly(4-vinyl pyridine), Poly(4-vinyl phenol) thin film and polycarbonate substrates which lack liquid resistance possess low surface free energy after modification with B-ala/AIBN = 5/1 PBZ.

Chapter 1

Introduction

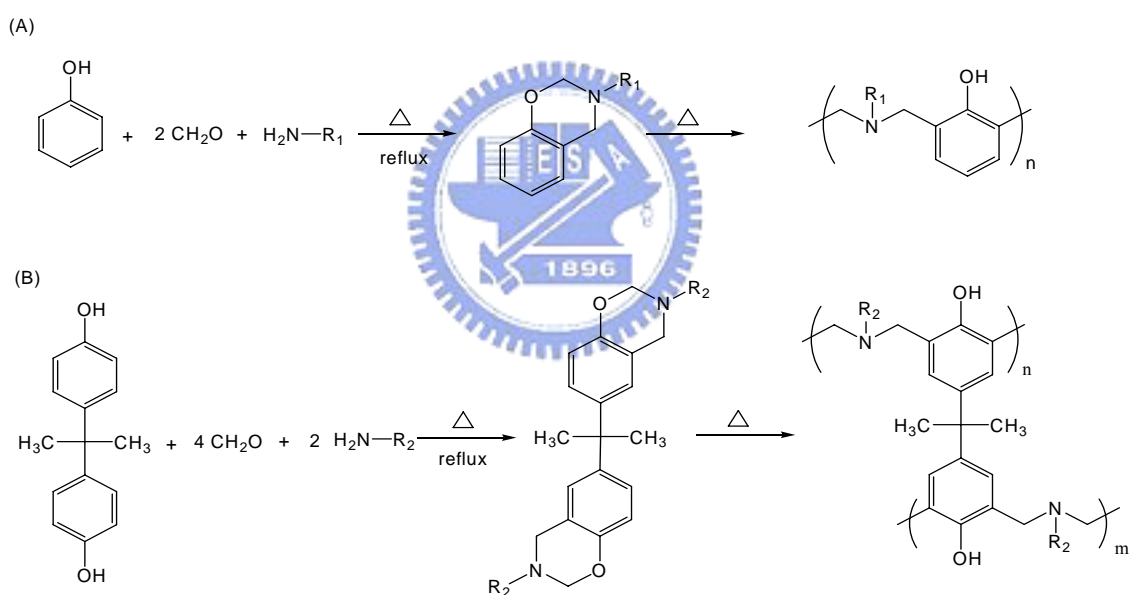
1.1 Overview on Benzoxazines and Polybenzoxazines

An interesting addition-cure phenolic system is based on oxazine-modified phenolic resin that encounters a ring-opening polymerization to give polybenzoxazine, which is mainly a poly (amino-phenol). The benzoxazine monomers are formed from amines and phenol in the presence of formaldehyde, which were first synthesized by Holly and Cope [1]. These structures were not recognized as phenolic resin precursors until Schreiber [2] reported in 1973 that a hard and brittle phenolic material was formed from benzoxazine precursors, but no further details about structures and properties were included. In 1986, Riess et al. reported the synthesis and reactions of monofunctional benzoxazine compound. [3] The compounds that they obtained were oligomer phenolic structures because the thermo-dissociation of the monomer was always competing with the chain propagation. The bifunctional benzoxazine precursor synthesized by Ning and Ishida [4] overcame the low degree of crosslinking of above compounds. Furthermore, these samples possess high mechanical integrity and can be easily prepared from inexpensive raw materials. [5-7]

In phenolic chemistry, both the ortho- and para- position on the benzene ring are reactive toward electrophilic substitution reactions due to the directing effect of the hydroxyl group. Benzoxazines also show multiple reactivities of the benzene ring due to directing effect of both the alkoxy and alkyl groups connected to the benzene ring as shown in Scheme 1-1. Benzoxazines can be polymerized without by using strong acid or basic catalyst, and produce no byproducts through the heterocyclic ring opening reaction. The free ortho- position on a benzene ring in the benzoxazine system has high reactivity toward thermal and phenol-initiated ring-opening

polymerizations and form a phenolic Mannich base (-CH₂-NR-CH₂-) polymer structure. In addition, the free para- position also shows reactivity toward a similar type of polymerization. [3, 8]

The ring-opening polymerization can also be catalyzed by acidic catalysts that permit a wide curing temperature. In the presence of acidic catalysts [9], the curing temperature can be reduced from 160-220 °C to about 130-170 °C and increase the application range. In recent years, thermosetting polybenzoxazines have attracted an intense amount of interest from both academia and industry because of their fascinating characteristics, such as high performance, low cost, and ease of processing. [10-13]



Scheme 1-1. The synthesis and thermal curing of (A) monofunctional benzoxazines and (B) difunctional benzoxazines

In addition to these advantageous features, which they share with traditional phenolic resins, the polybenzoxazines also possess unique properties, such as low degrees of water absorption [14, 15] (despite the large number of hydroxyl groups present in their backbone structure), high moduli, [16] excellent resistance to

chemicals [17] and UV light, [18] near-zero volumetric shrinkage/expansion upon polymerization, [19] and high glass transition temperatures, even at a relatively low cross-linking density. [20] The polybenzoxazines overcome several defects of traditional novolac and resole-type phenolic resins, while retaining their advantages. Polybenzoxazine resins are supposed to replace traditional phenolics, polyesters, vinyl esters, epoxies, cyanate esters and polyimides in many respects. [21] The molecular structure of polybenzoxazine offers excellent design flexibility that allows properties of the cured material to be controlled for specific requirements of a wide variety of individual requirements. The resin allows development of new applications by utilizing some of their unique features such as [19, 20, 22]:

- ◆ Near zero volumetric change upon polymerization
- ◆ No release of volatiles during curing
- ◆ Low melting viscosity (for benzoxazine)
- ◆ High glass transition temperature (T_g)
- ◆ High thermal stability (T_d)
- ◆ Low CTE
- ◆ Low water absorption
- ◆ Good mechanical properties
- ◆ Excellent electrical properties

Table 1-1 compares the properties of polybenzoxazine with those of the state-of-the-art matrices. The relative benefits of polybenzoxazines are obvious.

Table 1-1 Comparative polybenzoxazine properties of various high performance polymers

Property	Epoxy	Phenolics	Toughened BMI	Bisox-phen (40:60)	Cyanate ester	P-T resin	Polybenzoxazine
Density (g/cc)	1.2–1.25	1.24–1.32	1.2–1.3	1.3	1.1–1.35	1.25	1.19
Max use temperature (°C)	180	200	~200	250	150–200	300–350	130–280
Tensile strength (MPa)	90–120	24–45	50–90	91	70–130	42	100–125
Tensile modulus (GPa)	3.1–3.8	03/05	3.5–4.5	4.6–5.1	3.1–3.4	4.1	3.8–4.5
Elongation (%)	3–4.3	0.3	3	1.8	02/04	2	2.3–2.9
Dielectric constant (1 MHz)	3.8–4.5	04/10	3.4–3.7	–	2.7–3.0	3.1	3–3.5
Cure temperature (°C)	RT–180	150–190	220–300	175–225	180–250	177–316	160–220
Cure shrinkage (%)	>3	0.002	0.007	<1	~3	~3	~0
TGA onset (8C)	260–340	300–360	360–400	370–390	400–420	410–450	380–400
Tg (°C)	150–220	170	230–380	160–295	250–270	300–400	170–340
G _{IC} (J/m ²)	54–100	–	160–250	157–223	–	–	168
K _{IC} (MPa m ^{1/2})	0.6	–	0.85	–	–	–	0

1.2 Introduction to Polyhedral Oligomeric Silsesquioxane (POSS)

1.2.1 A quick history of Polyhedral Oligomeric Silsesquioxane (POSS)

In 1991, Lichtenhan and the Air Force Research Laboratory received funding from the Air Force Office of Scientific Research for his proposed development of POSS macromers containing a polymerizable functional group and the subsequent synthesis of a POSS-copolymer [23, 24]. The University-Government collaboration between Lichtenhan and Feher rapidly expanded to include more academic coaborators including Laine and Sellinger [25], Mather et al. [26] and others who were all intrigued by the physical and mechanical property improvements imparted by incorporation of these nanostructured materials into polymer systems. In the late nineties not only was government and academic interest growing, but also that of the industrial sector which desired lowers costs and larger quantities of the material.

The fall of 1998 marked the start-up of Hybrid Plastics in Fountain Valley, CA, which transitioned the government scale-up facilities to the commercial sector through a cooperative research and development agreement. In addition, the award of a 3 year multimillion dollor NIST Advanced Technology Program grant in 1998 to Hybrid Plastics was critical in both reducing the prices of the POSS feedstocks and macromers (\$ 5000- \$ 10000 down to \$ 50- \$ 2000 per pound) and increasing production (<20 to >2000 lb/year) to satisfy the more than 100 companies now investigating how the incorporation of POSS improves material properties for their applications. In the summer of 2003, Hybrid Plastics launched critical agreements with Southern Mississippi State University and the City of Hattiesburg for their development of a 26000 sq ft production facility and a 1500 sq ft R&D center.

The nearly exponential increase in the number of academic researchers, academic publications (Figure 1-1), government programs, and industrial research

efforts on POSS nanostructured chemicals has made it one of the top nanomaterials in the nanoscience/nanotechnology field. Indeed, the versatility of the POSS molecule, the more than one hundred demonstrated compatible polymer systems and the innumerable applications makes it difficult to understand and discern the current and future direction. However, it is clear that at least one concerted effort with a single-minded goal of predicting and controlling structure-property relationships is needed, and is being pursued by a number of research groups working with POSS nanostructured chemicals.

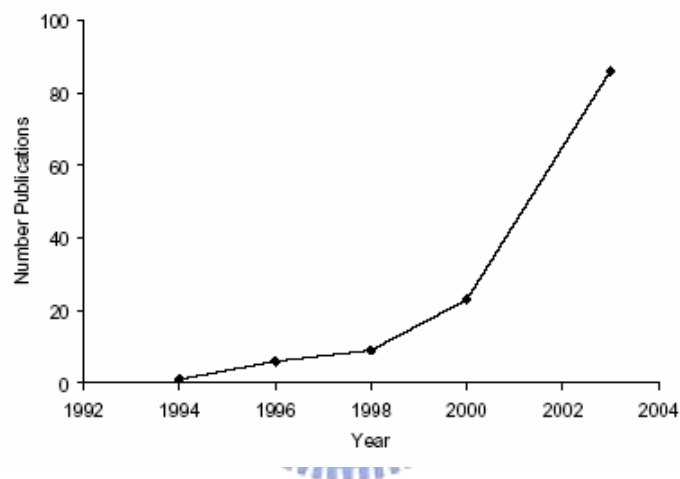


Figure 1-1. Plot of the number of POSS publications versus the year

1.2.2 Silsesquioxanes and Polyhedral Oligomeric Silsesquioxane(POSS)

The term silsesquioxane refers to all structures with the empirical formula $R_{Si}O_{1.5}$, where the R is hydrogen or any alkyl, alkylene, aryl, arylene, or organofunctional derivative of alkyl, alkylene, aryl, or arylene groups. The silsesquioxanes include random structures, ladder structures, cage structures, and partial cage structures, as illustrated in Figure 1-2. [27]

In 1995, Baney et al. reviewed the structure, preparation, properties, and applications of silsesquioxanes, especially the ladder-like polysilsesquioxanes shown

in Figure 1-2 (structure b). These include poly(phenylsilsesquioxane) (PPSQ) [28, 29], poly(methyl silsesquioxane) (PMSQ) [30-32], and poly(hydridosilsesquioxane) (PHSQ) [33, 34]. These ladder-like polymers have an outstanding thermal stability and they exhibit oxidative resistance even at temperatures of more than 500°C. In addition, these ladder-like polymers have good insulating properties and gas permeabilities.

Therefore, the ladder-like silsesquioxane polymers have a variety of applications in areas such as photoresist coatings [35, 36] for electronics and optical devices, interlayer dielectrics and protective coating films [37, 38] for semiconductor devices, liquid crystal display elements [39], magnetic recording media [40], optical fiber coatings [41], gas separation membranes [42], binders for ceramics [43]. However, in the past few years, much more attention has been paid to the silsesquioxanes with specific cage structures [Figure 1-2 structure c-f]. These Polyhedral Oligomeric Silsesquioxane have been designated by the abbreviation POSS.

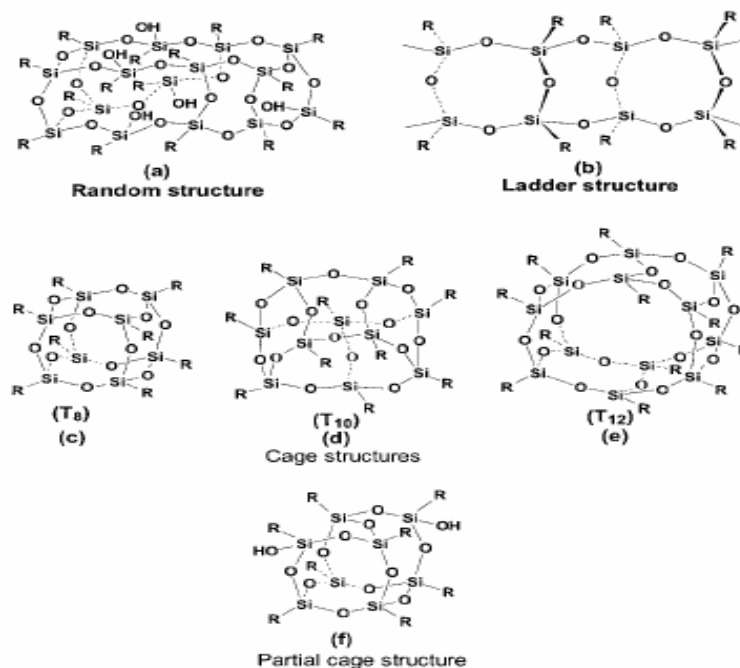


Figure 1-2. Structures of silsesquioxanes

POSS compounds embody a truly hybrid (inorganic-organic) architecture, which contains an inner inorganic framework made up of silicon and oxygen ($\text{SiO}_{1.5}$)_x, that is externally covered by organic substituents. These substituents can be totally hydrocarbon in nature or they can embody a range of polar structures and functional groups. POSS nanostructured chemicals, with sizes of from 1 to 3 nm in diameter, can be thought of as the smallest possible particles of silica, as shown in Figure 1-3. They may be viewed as molecular silicas. However, unlike silica, silicones, or fillers, each POSS molecule contains organic substituents on its outer surface that make the POSS nanostructure compatible with polymers, biological systems, or surfaces. Furthermore, these groups can be specially designed to be nonreactive or reactive.

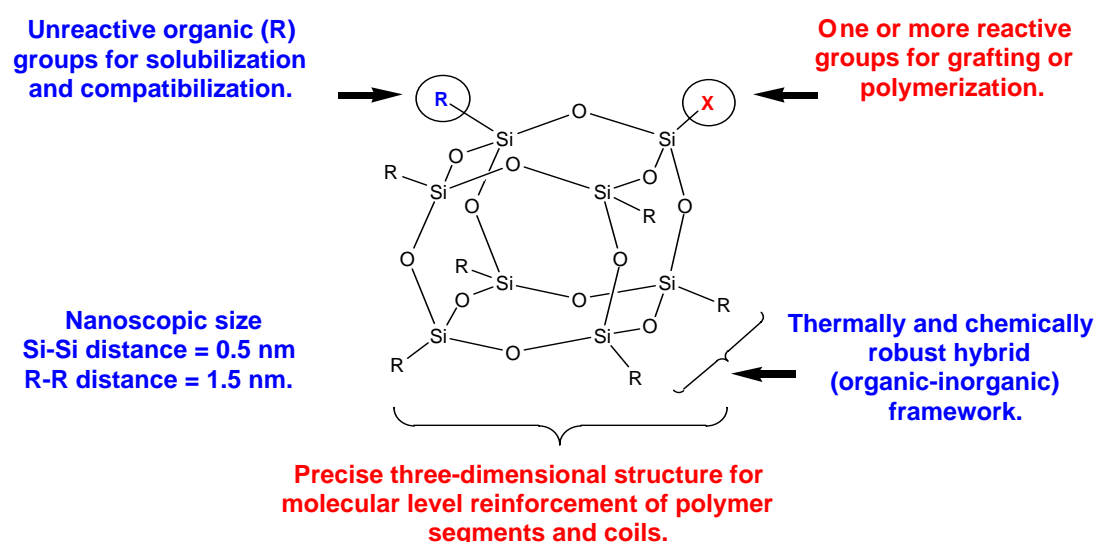


Figure 1-3. Structures of polyhedral oligomeric silsesquioxane (POSS)

A variety of POSS nanostructured chemicals have been prepared which contain one or more covalently bonded reactive functionalities that are suitable for polymerization, grafting, surface bonding, or other transformations [44]. Unlike traditional organic compounds, POSS chemicals release no volatile organic components, so they are odorless and environmentally friendly.

1.2.3 POSS Polymers and Copolymers

The incorporation of POSS derivatives into polymeric materials can lead to dramatic improvements in polymer properties which include, but are not limited to, increases in use temperature, oxidation resistance, surface hardening, and improved mechanical properties, as well as reductions in flammability, heat evolution, and viscosity during processing. These enhancements have been shown to apply to a wide range of thermoplastics and a few thermoset systems [45]. It is especially convenient that the use of POSS monomers doesn't require dramatic changes in processing. Monomers are simply mixed and copolymerized. As long as the POSS monomer is soluble in the monomer mixture, it is incorporated in a true molecular dispersion into the copolymer. No phase separation will occur although some aggregation of POSS units bound with polymer will occur. This is a significant advantage over current filler technologies. POSS nanostructures have also shown significant promise for use in catalyst supports and biomedical applications as scaffolds for drug delivery, imaging reagents, and combinatorial drug development.

References

- [1] Holly, F. W.; Cope, A. C. *J. Am. Chem. Soc.* **1944**, *66*, 1875.
- [2] Scheriber, H. G. *Offen.* **1973**, 225
- [3] Riess, G.; Schwob, J. M.; Guth, G.; Roche, M.; Lande, B. in “*Advances in Polymer Science*” (Eds B. M. Culbertson and J. E. Mcgrath), Plenum, New York, **1986**.
- [4] Ning, X.; Ishida, H. *J. Polym. Sci., Polym. Phys. Ed.* **1994**, *32*, 921.
- [5] Ishida, H. *J. Appl. Polym. Sci.* **1995**, *58*, 1751.
- [6] Burke, W. J.; Murdoch, K. C.; Ec, G. *J. Am. Chem. Soc.* **1954**, *76*, 1677.
- [7] Burke, W. J.; Glennie, E. L. M.; Weatherbee, C. *J. Org. Chem.* **1964**, *24*, 909.
- [8] Shen, S. B.; Ishida, H. *J. Appl. Polym. Sci.* **1996**, *61*, 1595.
- [9] Dunkers, J.; Ishida, H. *J. Polym. Sci. Part A: Polym. Chem.* **1999**, *37*, 1913.
- [10] Ning, X.; H. Ishida, *J. Polym. Sci., Part A: Polym. Chem.* **1994**, *32*, 1121.
- [11] Takeichi, T.; Komiya, I.; Takayama, Y. *Kyoka-Purasutikkus* (in Japanese) **1997**, *43*, 109.
- [12] Wang, Y. X.; Ishida, H. *Polymer* **1999**, *40*, 4563.
- [13] Macko, J. A.; Ishida, H. *Polymer* **2001**, *42*, 227.
- [14] Furukawa, N. *Benzoxazine-based thermosetting polymers and their manufacture, compositions, and heat- and fire-resistant dielectric cured products with low water absorption.* Jpn. Kokai Tokkyo Koho, **2004**, p18.
- [15] Wang, Y. X.; Ishida, H. *Polym. Mater. sci. eng.* **1999**, *80*, 211.
- [16] Ishida, H.; Allen, D. J. *J. Polym. Sci., Part B: Polym. Phys.* **1996**, *34*, 1019.
- [17] Kim, H. D.; Ishida, H. *J. Appl. Polym. Sci.* **2001**, *79*, 1207.
- [18] Macko, J.; Ishida, H. *J. Polym. Sci., Part B: Polym. Phys.* **2000**, *38*, 2687.
- [19] Ishida, H.; Low, H. Y. *Macromolecules* **1997**, *30*, 1099.

- [20] Ishida, H.; Rodriguez, Y. *Polymer* **1995**, *36*, 3151.
- [21] Nair, C. P. R. *Prog. Polym. Sci.* **2004**, *29*, 401.
- [22] Agag, T.; Takeichi, T. *Macromolecules* **2001**, *34*, 7257.
- [23] Lichtenhan, J. D.; Feher, F. J.; Gilman, J. W. *Macromolecules* **1993**, *26*, 2141.
- [24] Lichtenhan, J. D.; Otonari, Y.; Carr, M. J. *Macromolecules* **1995**, *28*, 8435.
- [25] Laine, R. M.; Sellinger, A. *Macromolecules* **1996**, *29*, 2327.
- [26] Mather, P. T.; Haddad, T. S.; Oviatt, H. W.; Schwab, J. J.; Chaffee, K. P.; Lichtenhan, J. D. *Polym Prepr* **1998**, *39*, 611.
- [27] Baney, R. H.; Itoh, M.; Sakakibara, A.; Suzuki, T. *Chem. Rev.* **1995**, *95*, 1409.
- [28] Zhang, X.; Shi, L. C. *J. Polym. Sci.* **1987**, *5*, 197.
- [29] Brown, Jr. J. F. *J. Polym. Sci. C* **1987**, *1*, 83.
- [30] Xie, Z.; He, Z.; Dai, D.; Zhang, Chin. R. *J. Polym. Sci.* **1989**, *7*, 183.
- [31] Maciel, G. E.; Sullivan, M. J.; Sindorf, D. W. *Macromolecules* **1981**, *14*, 1607.
- [32] Engelhavdt, G.; Jancke, H.; Lippmaa, E.; Samoson, A. *J. Organomet. Chem.* **1981**, *210*, 295.
- [33] Frye, C. L.; Collins, W. T. *J. Am. Chem. Soc.* **1970**, *92*, 5586.
- [34] Belot, V.; Corriu, R.; Leclerq, D.; Mutin, P. H.; Vioux, A. *Chem. Mater.* **1991**, *3*, 127.
- [35] Adachi, H.; Hayashi, O.; Okahashi, K. *Japanese Patent Kokoku-H-2-15863*.
- [36] Adachi, H.; Hayashi, O.; Okahashi, K. *Japanese Patent Kokai-S-60-108841*.
- [37] Adachi, E.; Aiba, Y.; Adachi, H. *Japanese Patent Kokai-H-2-277255*.
- [38] Aiba, Y.; Adachi, E.; Adachi, H. *Japanese Patent Kokai-H-3-6845*.
- [39] Shoji, F.; Sudo, R.; Watanabe, T. *Japanese Patent Kokai-S-56-146120*.
- [40] Imai, E.; Takeno, H. *Japanese Patent Kokai-S-59-129939*.
- [41] Mishima, T.; Nishimoto, H. *Japanese Patent Kokai-H-4-247406*.

[42] Saito, Y.; Tsuchiya, M.; Itoh, Y. *Japanese Patent Kokai-S-58-14928*.

[43] Mine, T.; Komasaki, S. *Japanese Patent Kokai-S-60-210570*.

[44] Lichtenhan, J. D.; Schwab, J. J.; Reinerth, Sr. W. A. *Chem. Innovat.* 1, 3.

[45] Ellsworth, M. W.; Gin, D. L. *Polym. News* 24, 331.



Chapter 2

Introduction to Surface Free Energy Theory

2.1 Surface Free Energy

2.1.1 Interfacial Thermodynamics

The interface (surface) is a region of finite thickness (usually less than 0.1 μm) in which the composition and energy vary continuously from one bulk phase to other. The pressure (force field) in the interfacial zone is therefore nonhomogeneous, having a gradient perpendicular to the interfacial boundary. In contrast, the pressure in a bulk phase is homogeneous and isotropic. Consequently, no net energy is expended in reversibly transporting the matter within a bulk phase. However, a net energy is required to create an interface by transporting from the bulk phase to the interfacial zone. The reversible work required to create a unit surface area is the surface free energy, that is,

$$\gamma = \left(\frac{\partial G}{\partial A} \right)_{T, P, n} \quad (2.1)$$

Where γ is the surface free energy, G the Gibbs free energy of the total system, A the interfacial area, T the temperature, P the pressure, and n the total number of moles of matter in the system.

The work required separating reversibly the interface between two bulk phases α and β from their equilibrium separation to infinity is the work of adhesion.

$$W_a = W_{\alpha\beta} = \gamma_\alpha + \gamma_\beta - \gamma_{\alpha\beta} \quad (2.2)$$

Where W_a is the work of adhesion, γ_α the surface free energy of phase α , γ_β the surface free energy of phase β , and $\gamma_{\alpha\beta}$ the interfacial energy between phase α and β (Figure 2-1).

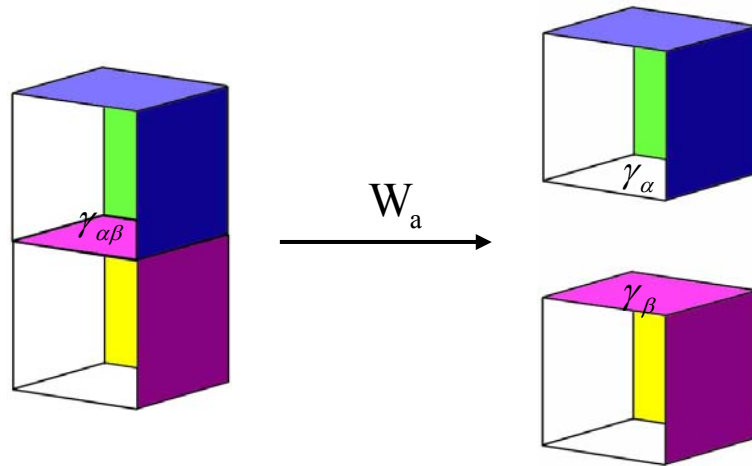


Figure 2-1. Work of adhesion.

This was apparently first purpose by Dupré.[1] When the two phase are identical, the reversible work is the work of cohesion (Figure 2-2),

$$W_c = W_{jj} = \gamma_j + \gamma_j - 0 = 2\gamma_j \quad (2.3)$$

Where W_c is the work of cohesion for phase j.

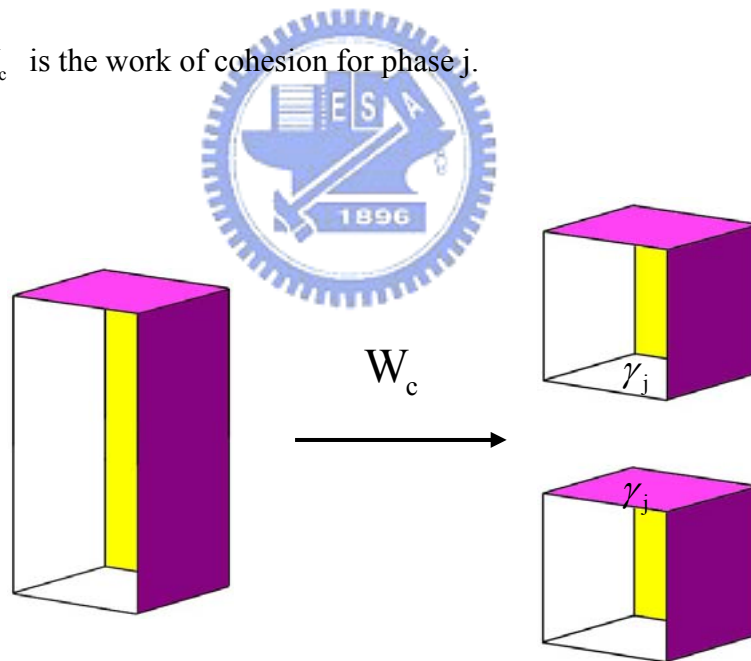


Figure 2-2. Work of cohesion.

The work of adhesion is the decrease of Gibbs free energy per unit area when an interface is formed from two individual surfaces. Thus, the greater the interfacial attraction, the greater the work of adhesion will be. Rearrangement of Eq. (2.1) gives

$$\gamma_{\alpha\beta} = \gamma_\alpha + \gamma_\beta - W_a \quad (2.4)$$

indicating that the greater the interfacial attraction, the smaller the interfacial energy will be. The works of adhesion can be related to the cohesion theoretically. Thereby, the interfacial energy can be linked to the properties of the two individual phases.

Thermodynamic discussions of adhesion in solid-liquid systems should be carried out in terms of surface free energy rather than surface tension. Discussions that involve the shape of liquid-gas or liquid-liquid interfaces can be carried out either in terms of surface tension or surface free energy.

2.1.2 Contact Angle Equilibrium: Young Equation

A liquid in contact with a solid will exhibit a contact angle (Figure 2-3). If the system is at rest, a static contact angle is obtained. If the system is in motion, a dynamic contact angle is obtained. Here, static contact angles are discussed. A system at rest may be in stable equilibrium (the lowest energy state), or in meta stable equilibrium (an energy through separated from neighboring states by energy barriers).

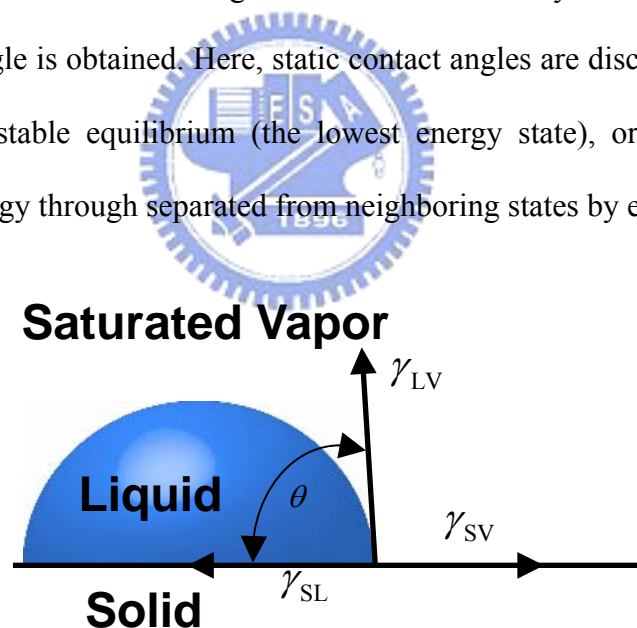


Figure 2-3. Contact angle equilibrium on a smooth, homogeneous, planar, and rigid surface

Stable equilibrium will be obtained if the solid surface is ideally smooth, homogeneous, planar, and nondeformable; the angle formed is the equilibrium contact angle, θ .

On the other hand, if the solid surface is rough or compositionally heterogeneous, the system may reside in one of many stable states; the angle formed is a metastable contact angle. The amount of mechanical energy in the liquid drop (such as vibrational energy) determines which metastable state is to be occupied. Therefore, metastable contact angle vary with drop volume, external mechanical energy (such as vibration), and how the angle is formed (whether by advancing or receding the liquid front on the solid). The stable equilibrium contact angle may sometimes (but rarely) be observed on a rough or heterogeneous surface. This equilibrium angle corresponds to the lowest energy state.

The angle formed by advancing the liquid front on the solid is termed advancing contact angle, θ_a (Figure 2-4). The angle formed by receding the liquid front on the solid is termed receding contact angle, θ_r (Figure 2-5).

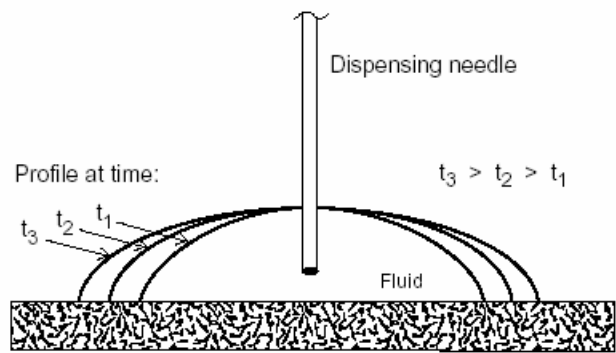


Figure 2-4. Advancing contact angle

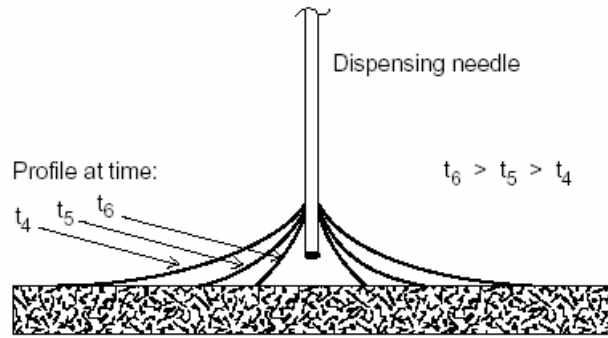


Figure 2-5. Receding contact angle

Advancing contact angle are usually greater than receding contact angle when the system is in a metastable state. On the other hand, the advancing and the receding angles are identical when equilibrium angles are formed. Many real surfaces are rough or heterogeneous. Thus, variable contact angles are often observed. This has previously led to concern as to whether is a true thermodynamic quality. The origin of variable contact angle has now been clearly established and the thermodynamic status of contact angle ascertained.

The equilibrium contact angle (abbreviated θ here) for liquid drop on an ideally smooth, homogeneous, planar, and nondeformable surface (Figure 2-3) is related to the various interfacial tensions by

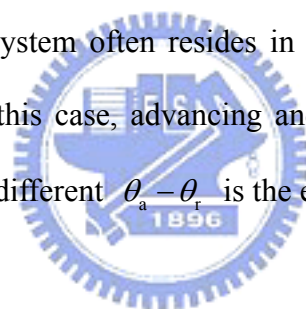
$$\gamma_{LV} \cos \theta = \gamma_{SV} - \gamma_{SL} \quad (2.5)$$

Where γ_{LV} is the surface tension of the liquid in equilibrium with its saturated vapor, γ_{SV} the surface free energy of the solid in equilibrium with the saturated vapor of the liquid, and γ_{SL} the interfacial tension between the solid and the liquid. This is known as the Young equation. Young [2] described the relation in words, and did not attempt to prove it. Several proofs were offered later by others. [3-5]

Many real surfaces are rough or heterogeneous. A liquid drop resting on such a surface may reside in the stable equilibrium (the lowest energy state), or in a

metastable equilibrium (energy trough separated from neighboring states by energy barriers). The equilibrium contact angle θ_e corresponds to the lowest energy state for a system. On an ideally smooth and compositionally homogeneous surface, the equilibrium contact angle is the Young's angle θ_Y , which is also the microscopic local contact angle on any rough or heterogeneous surface, hence also known as the intrinsic contact angle θ_0 . The fact that θ_0 equals θ_Y has been proved theoretically as the condition for minimization of system free energy.

The equilibrium contact angle on a rough surface is Wenzel's angle θ_w . The equilibrium contact angle on a heterogeneous surface is Cassie's angle θ_c . These angles correspond to the lowest energy state, but are often not observed experimentally. Instead, the system often resides in a metastable state, exhibiting a metastable contact angle. In this case, advancing and receding angles are different, known as hysteresis (H). The different $\theta_a - \theta_r$ is the extent of hysteresis.



2.1.3 Determination of Surface Free Energy

The surface free energy of a solid polymer cannot be measured directly, as reversible formation of its surface is difficult. Many indirect methods have been proposed, including the polymer melt (temperature dependence) method, Good-Girifalco Method, Owens, Wendt, and Kaelble's Method (Two-Liquid Geometric Method), Wu's Method (Two-Liquid Harmonic Method), Lifshitz-van der Waals Acid-Base Theory (Three-Liquid Acid-Base Method), critical surface tension and others.

Good–Girifalco Method

Good and Girifalco in the 1950s proposed the following equation to describe the surface energy of interfacial phase systems: [6-8]

$$\gamma_{ab} = \gamma_a + \gamma_b - 2\Phi(\gamma_a\gamma_b)^{1/2} \quad (2.6)$$

The subscripts a and b refer to the two phases, which may be liquid or solid. Φ is a constant between interfaces of a system and is defined as:

$$-\frac{\Delta F_{ab}^a}{(\Delta F_a^c \Delta F_b^c)^{1/2}} = \Phi \quad (2.7)$$

Where ΔF_{ab}^a = the free energy of adhesion for the interface between phases A and B, per cm^2 , $= \gamma_{ab} - \gamma_a - \gamma_b$ and ΔF_n^c = free energy of cohesion for phase N $= 2\gamma_n$. Equation (2.6) can be rewritten as the well known Good and Girifalco equation:

$$\gamma_{SL} = \gamma_S + \gamma_{LV} - 2\Phi(\gamma_S\gamma_{LV})^{1/2} \quad (2.9)$$

Combined equations 2.5 and 2.9 yield:

$$\gamma_{LV}(1 + \cos \theta) = 2\Phi(\gamma_S\gamma_{LV})^{1/2} \quad (2.10)$$

Or

$$\gamma_S = \frac{\gamma_{LV}(1 + \cos \theta)^2}{4\Phi^2} \quad (2.11)$$

Suppose the value of Φ is known for a pair of the testing solid and liquid, γ_S can be calculated from contact angle data with eq. (2.11). In the zeroth order approximation, Good and Girifalco suggested that Φ was equal to unity.

Fowkes' Method

Fowkes [9,10] proposed that “the surface tensions are a measure of the attractive forces between surface layers and liquid phase, and that such forces and

their contribution to the free energy are additive.” He designated, in the case of the surface tension of water, the surface tension could be considered the sum of contributions from dispersion forces (γ^d) and dipole interactions, mainly hydrogen bonds (γ^h):

$$\gamma_{\text{H}_2\text{O}} = \gamma_{\text{H}_2\text{O}}^d + \gamma_{\text{H}_2\text{O}}^h \quad (2.12)$$

where superscript h refers to hydrogen bonding, and d to dispersion. In addition, at the interface between a liquid and solid, as Fowkes pointed out, the interfacial molecules are attracted by the bulk liquid from one side and from the other side by the intermolecular forces between the two phases. Fowkes defined the dispersion force contribution to surface tension of the solid in terms of the interaction with the dispersion forces of the liquid. As a result, the Young–Good–Girifalco equation can be modified as:

$$\gamma_{SL} = \gamma_S + \gamma_{LV} - 2(\gamma_S^d \gamma_{LV}^d)^{1/2} \quad (2.13)$$

Combine eqs. (2.5) and (2.13) results in:

$$\gamma_{LV}(1 + \cos \theta) = 2(\gamma_S^d \gamma_{LV}^d)^{1/2} \quad (2.14)$$

Strictly speaking, eq. (2.14) provides a method to estimate the value of γ_S^d , but not total γ_S , from a single contact angle measurement, where only dispersion forces operate in the liquid, such as a hydrocarbon liquid. The γ_S^d of any solid can be determined using a “dispersion force only” liquid.

Owens, Wendt, and Kaelble’s Method

(Two-Liquid Geometric Method)

Owens and Wendt [11] and Kaelble [12] extended Fowkes’ equation to a more general form:

$$\gamma_{SL} = \gamma_S + \gamma_{LV} - 2(\gamma_S^d \gamma_{LV}^d)^{1/2} - 2(\gamma_S^p \gamma_{LV}^p)^{1/2} \quad (2.15)$$

Combine eqs. (2.5) and (2.15) yield:

$$\gamma_{LV}(1 + \cos \theta) = 2(\gamma_S^d \gamma_{LV}^d)^{1/2} + 2(\gamma_S^p \gamma_{LV}^p)^{1/2} \quad (2.16)$$

Where superscript d refers to a dispersion (nonpolar) component, and p refers to a polar (nondispersion) component, including all the interactions established between the solid and liquid, such as dipole– dipole, dipole-induced dipole and hydrogen bonding, etc.

Since γ_S is the sum of surface tension components contributed from dispersion and polar parts:

$$\gamma_S = \gamma_S^d + \gamma_S^p \quad (2.17)$$

Equations (2.15) and (2.16) provide a method to estimate surface tension of solids.

Using two liquids with known γ_L^d and γ_L^p for contact angle measurements, one could easily determine γ_S^d and γ_S^p by solving the following two equations:

$$\begin{aligned} \gamma_{LV1}(1 + \cos \theta_1) &= 2(\gamma_S^d \gamma_{LV1}^d)^{1/2} + 2(\gamma_S^p \gamma_{LV1}^p)^{1/2} \\ \gamma_{LV2}(1 + \cos \theta_2) &= 2(\gamma_S^d \gamma_{LV2}^d)^{1/2} + 2(\gamma_S^p \gamma_{LV2}^p)^{1/2} \end{aligned} \quad (2.18)$$

The values of γ_L^d and γ_L^p of reference liquids have been provided by Kaelble.

Wu's Method (Two-Liquid Harmonic Method)

This method uses the contact angles of two testing liquids and the harmonic-mean equation. The result agree remarkable well with the liquid homolog method, polymer melt method, and the equation of state method.

Based on “harmonic” mean and force addition, Wu proposed the following equations: [13, 14]

$$\gamma_{SL} = \gamma_S + \gamma_{LV} - \frac{4\gamma_S^d \gamma_{LV}^d}{\gamma_S^d + \gamma_{LV}^d} - \frac{4\gamma_S^p \gamma_{LV}^p}{\gamma_S^p + \gamma_{LV}^p} \quad (2.19)$$

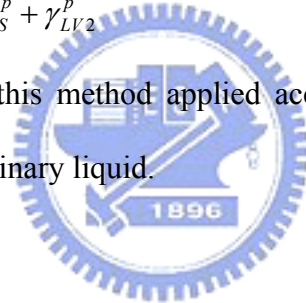
Equation (2.19) can be written as follows with the aid of eq. (2.5):

$$\gamma_{LV}(1 + \cos \theta) = \frac{4\gamma_S^d \gamma_{LV}^d}{\gamma_S^d + \gamma_{LV}^d} + \frac{4\gamma_S^p \gamma_{LV}^p}{\gamma_S^p + \gamma_{LV}^p} \quad (2.20)$$

Equations (2.19) and (2.20) provide a method to estimate surface tension of solids. Using two liquids with known γ_L^d and γ_L^p for contact angle measurements, one could easily determine γ_S^d and γ_S^p by solving the following two equations:

$$\begin{aligned} \gamma_{LV1}(1 + \cos \theta) &= \frac{4\gamma_S^d \gamma_{LV1}^d}{\gamma_S^d + \gamma_{LV1}^d} + \frac{4\gamma_S^p \gamma_{LV1}^p}{\gamma_S^p + \gamma_{LV1}^p} \\ \gamma_{LV2}(1 + \cos \theta) &= \frac{4\gamma_S^d \gamma_{LV2}^d}{\gamma_S^d + \gamma_{LV2}^d} + \frac{4\gamma_S^p \gamma_{LV2}^p}{\gamma_S^p + \gamma_{LV2}^p} \end{aligned} \quad (2.21)$$

Wu [13] claimed that this method applied accurately between polymers and between a polymer and an ordinary liquid.



Lifshitz–van der Waals Acid-Base Theory (Three-Liquid Acid-Base Method)

Van Oss et al. have proposed a methodology that represents both Fowkes–Owens–Wendt–Kaelble and Wu. This methodology introduces a new meaning of the concepts, “apolar” and “polar,” the later cannot be represented by a single parameter such as γ^p .

As shown in eq. (2.12), surface tension γ could be divided into an apolar component and a hydrogen bonding component or (more generally) acidbase interaction. One may follow Fowkes’ approach [15,16] and separate surface energy into several components as:

$$\gamma = \gamma^d + \gamma^{\text{dip}} + \gamma^{\text{ind}} + \gamma^{\text{h}} + \dots \quad (2.22)$$

$$\gamma = \gamma^d + \gamma^{AB} \quad (2.23)$$

Where the superscripts, d, dispolar and h refer to (London) dispersion, (Keesom) dipole– dipole, (Debye) induction and hydrogen bonding forces, respectively. And the superscript AB refers to the acid-base interaction.

By regrouping components in eq. 18–1, van Oss and Good expressed the surface energy as:

$$\gamma = \gamma^{LW} + \gamma^{AB} \quad (2.24)$$

$$\gamma^{LW} = \gamma^d + \gamma^{dip} + \gamma^{ind} \quad (2.25)$$

Where LW stands for Lifshitz–van der Waals. Because a hydrogen bond is a proton-sharing interaction between an electronegative molecule or group and electropositive hydrogen, a hydrogen bonding is an example of Lewis acid (electron acceptor) and Lewis base (electron donor). Van Oss et al., [17-23] therefore, treated hydrogen bonding as Lewis acid-base interactions. In addition, van Oss et al. [17- 19] created two parameters to describe the strength of Lewis acid and base interactions:

γ^+ = Lewis acid parameter of the surface free energy

γ^- = Lewis base parameter of the surface free energy

$$\gamma^{AB} = 2\sqrt{\gamma^+\gamma^-} \quad (2.26)$$

Based on these definitions, a material is classified as a bipolar substance if both its γ^+ and its γ^- are greater than 0 ($\gamma^{AB} \neq 0$). In other words, it has both nonvanishing γ^+ and γ^- . A monopolar material is one having either an acid or a base characters, which means either $\gamma^+ = 0$ and $\gamma^- > 0$ or $\gamma^+ > 0$ and $\gamma^- = 0$. An apolar material is neither an acid nor a base (both its γ^+ and its γ^- are 0). For both monopolar and apolar materials, their $\gamma^{AB} = 0$. Therefore, according to the Fowkes

notation, the criterion for a substance to be apolar, is, $\gamma^{AB} = 0$. This is not true in the van Oss and Good's methodology.

How do we calculate these surface energy parameters? van Oss, Good, and their coworkers, have developed a “three-liquid procedure” (Equation 2.27) to determine γ_s by using contact angles techniques and a traditional matrix scheme.

$$\begin{aligned}\gamma_{LV1}(1 + \cos \theta_1) &= 2(\sqrt{\gamma_S^{LW} \gamma_{LV1}^{LW}} + \sqrt{\gamma_S^+ \gamma_{LV1}^-} + \sqrt{\gamma_S^- \gamma_{LV1}^+}) \\ \gamma_{LV2}(1 + \cos \theta_2) &= 2(\sqrt{\gamma_S^{LW} \gamma_{LV2}^{LW}} + \sqrt{\gamma_S^+ \gamma_{LV2}^-} + \sqrt{\gamma_S^- \gamma_{LV2}^+}) \\ \gamma_{LV3}(1 + \cos \theta_3) &= 2(\sqrt{\gamma_S^{LW} \gamma_{LV3}^{LW}} + \sqrt{\gamma_S^+ \gamma_{LV3}^-} + \sqrt{\gamma_S^- \gamma_{LV3}^+})\end{aligned}\quad (2.27)$$

In short, to determine the components of γ_s of a polymer solid, it was recommended [24, 25] to select three or more liquids from the reference liquids table, with two of them being polar, the other one being apolar. Moreover, the polar pairs—water and ethylene glycol, and water and formamide— were recommended to give good results, while apolar liquids are either diiodomethane or *a*-bromonaphthalene. Because the LW, Lewis acid, and Lewis base parameters of γ_{LV1} , γ_{LV2} , and γ_{LV3} are available, one can determine the LW, Lewis acid, and base parameters of γ_s by solving these three equations simultaneously.

Critical Surface Tension – Zisman plot

The concept of critical surface tension was first proposed by Fox and Zisman [26-28]. An empirical rectilinear relation was found between $\cos \theta$ and γ_{LV} for a series of testing liquid on a given solid. When homogeneous liquids are used as the testing liquids, a straight line is often obtained. When nonhomologous liquids are used, however, the data are often scattered within a rectilinear band or give a curved line.

The intercept of the line at $\cos\theta = 1$ is the critical surface tension γ_c . When a band is obtained, the intercept of lower line of the band is defined as the critical surface tension. The $\cos\theta$ versus γ_{LV} plot is known as the Zisman plot. The example is given in Figure 2-6.

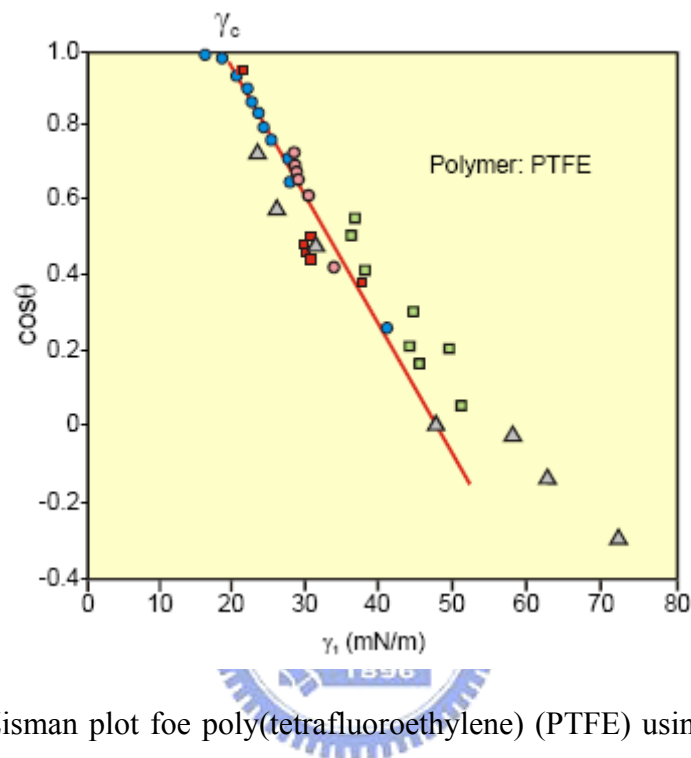


Figure 2-6. Zisman plot for poly(tetrafluoroethylene) (PTFE) using various testing liquids.

Adhesion Force Measurements - Johnson, Kendall, and Roberts (JKR) theory

Although contact angle goniometry is the method of choice for the determination of surface energies, atomic force microscopy may be a more readily accessible alternative. Atomic force microscopy can be used to measure the force of adhesion between polymer surfaces and an AFM tip (Figure 2-7). [29] The work of adhesion is related to the surface free energy of the polymer using Johnson, Kendall, and Roberts (JKR) theory of adhesion mechanics. [30,31] According to this model, the “pull-off” force, F_{ad} , required to separate an AFM tip of radius R from a planar surface is given

by

$$F_{ad} = 2\pi RW_{SMT}$$

$$W_{SMT} = \gamma_{SM} + \gamma_{TM} + \gamma_{ST}$$

$$W_{SMT} = 2\pi RW_{SMT} \quad (2.28)$$

W_{SMT} is the thermodynamic work of adhesion for separating the sample and tip; γ_{SM} and γ_{TM} are the surface free energies of the sample (S) and tip (T), respectively, in contact with the medium M; and, γ_{ST} is the interfacial surface free energy of the two interacting solid surfaces. [32] Indeed, a correlation has been reported between work of adhesion, as determined from force-distance curves (Figure 2-8), and surface free energies obtained from other techniques. [33, 34]

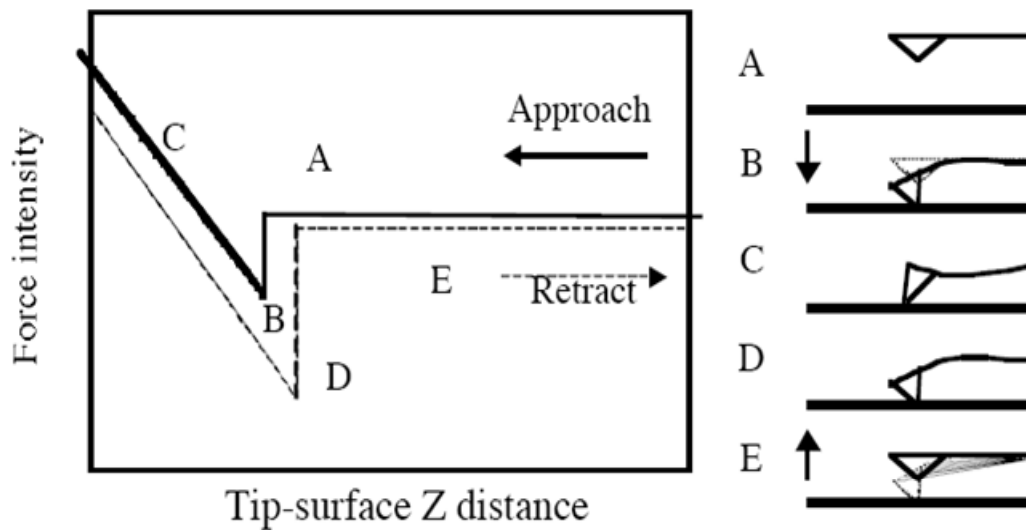


Figure 2-7. Process of adhesion force measurement

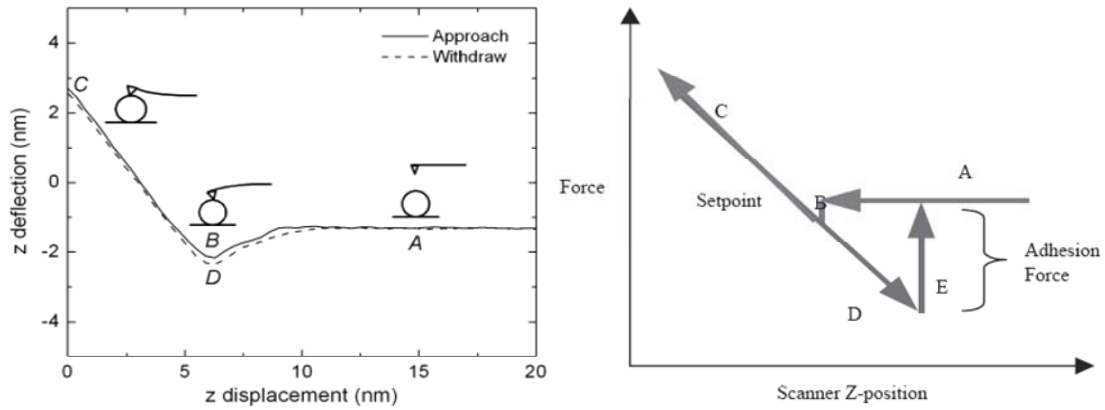


Figure 2-8. Force-distance curve and adhesion force

Adhesion Force Measurements - Derjaguin-Muller-Toporov (DMT) theory

The work of adhesion is related to the surface free energy of the polymer using Derjaguin-Muller-Toporov (DMT) theory of adhesion mechanics. [30] According to this model, the “pull-off” force, F_{ad} , required to separate an AFM tip of radius R from a planar surface is given by

$$F_{ad} = 2\pi RW_{SMT} \quad (2.29)$$

According to previous report, [35] the interfacial surface energy can be approximated by the following expression:

$$W_{D=0} = 2\sqrt{\gamma_1\gamma_2} \quad (2.30)$$

The γ_1 and γ_2 are the surface energy of the two bodies in contact. Therefore, the Derjaguin approximation (DMT theory) becomes:

$$F_{(D=0)} = 4\pi R\sqrt{\gamma_1\gamma_2} \quad (2.31)$$

2.1.4 Surface Free Energy of Polymer

Molecular-Weight Dependence

The surface free energy of homologous series tends to increase, while the

surface entropy tends to decrease, with increasing molecular weight. At infinite molecular weight, both the surface free energy and the surface entropy are, however, finite. The surface free energy of homologous series varies linearly with $M_n^{-2/3}$, [36, 37]

$$\gamma = \gamma_\infty - \frac{k_e}{M_n^{2/3}} \quad (2.32)$$

Where γ_∞ is the surface free energy at infinite molecular weight and k_e is a constant. This equation fits the data for n-alkanes with standard deviations in γ about 0.05 dyne/cm, and for prefluoroalkanes, polyisobutylenes, polydimethylsiloxanes, and polystyrenes with standard deviations in γ about 0.2 dyne/cm (Table 2-1).

Table 2-1. Numerical constant for molecular weight dependence of surface free energy.

polymer	Temp. °C	γ_∞ dyne/cm	k_e	σ^a
n-alkanes	20	37.81	385.9	0.03
Polyisobutylenes	24	35.62	382.7	0.34
Polydimethylsiloxanes	20	21.26	166.1	0.09
Prefluoroalkanes	20	25.85	682.8	0.30
Polystyrenes	176	29.97	372.7	0.08
Poly(ethylene oxide)- dimethyl ether	24	44.35	342.8	0.44

^a σ is the standard deviations in γ

The surface free energy variation decreases with increasing molecular weight. The k_e values in Table 2-1 indicate that γ will be smaller than γ_∞ by less than 1 dyne/cm when the molecular weight is greater about 3000. Accordingly, for instance, the surface free energy of poly(vinyl acetate) melts having molecular weight 11,000-120,000 are found to be practically independent of molecular weight (Figure

2-9). [38]

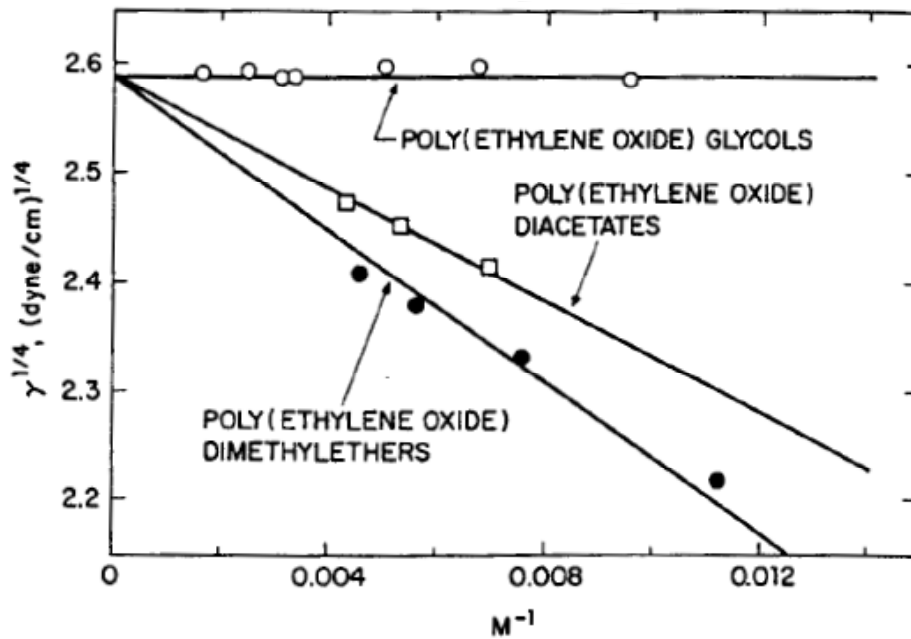
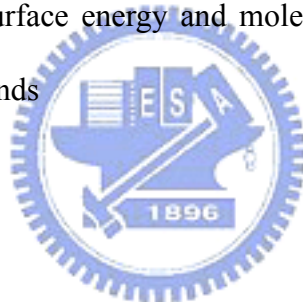


Figure 2-9. Comparison of surface energy and molecular weight between polymers with and without hydrogen bonds



Effects of Phase Transitions

At the crystal-melt transition, the surface free energy of crystalline phase γ^c is related to that of the amorphous phase γ^a by [39]

$$\gamma^c = \left(\frac{\rho_c}{\rho_a} \right)^n \gamma^a \quad (2.33)$$

where ρ_c is the crystalline density, ρ_a the amorphous density, and n the Macleod's exponent (Table 2-2).

Table 2-2. Macleod's exponent for some polymers

polymer	Macleod's exponent
Polychloroprene	4.2
Poly(methyl methacrylate)	4.2
Poly(n-butyl methacrylate)	4.2
Polystyrene	4.4
Poly(vinyl acetate)	3.2
Poly(ethylene oxide)	3.0
Polybutylene	4.1
Polypropylene	3.2
Polyethylene, linear	3.2
Polyethylene, branched	3.3
polydimethylsiloxane	3.5

Thus, at the crystal-melt transition, the surface free energy changes discontinuously, since the density is discontinuous. As ρ_c is usually greater than ρ_a , the crystalline phase will have higher surface free energy than amorphous phase. For instance, polyethylene has $n = 3.2$, $\gamma^a = 35.7$ dyne/cm, and $\rho_a = 0.855$ g/ml at 20 °C. The crystalline density ρ_c is 1.000 g/ml. Thus γ^c is calculated by eq. (2.33) to be 58.9 dyne/cm, which compares rather well with an experimental value of 53.6 dyne/cm. [40]

Semicrystalline polymers tend to be covered with an amorphous surface layer. As the amorphous phase has lower surface free energy, it tends to migrate to the surface.

Copolymers and Blends

Low-energy components in copolymers or blends tend to preferentially adsorb on the surface, just as in small-molecule liquids, as this will lower the free energy of

the system.

Random Copolymers

The surface free energy of a random copolymer usually follows the linear relation [41]

$$\gamma = x_1\gamma_1 + x_2\gamma_2 \quad (2.34)$$

where γ is the surface free energy and x is the mole fraction. The subscripts 1 and 2 refer to the components 1 and 2, respectively. Such behavior is shown for random copolymers of ethylene oxide and propylene oxide in Figure 2-10.

Block and Graft Copolymers

However, block and graft copolymers show considerable surface activity of the lower energy component, when the lower-energy blocks or grafts are sufficient long that they can accumulate and orient on the surfaces independently of the rest of the molecule.

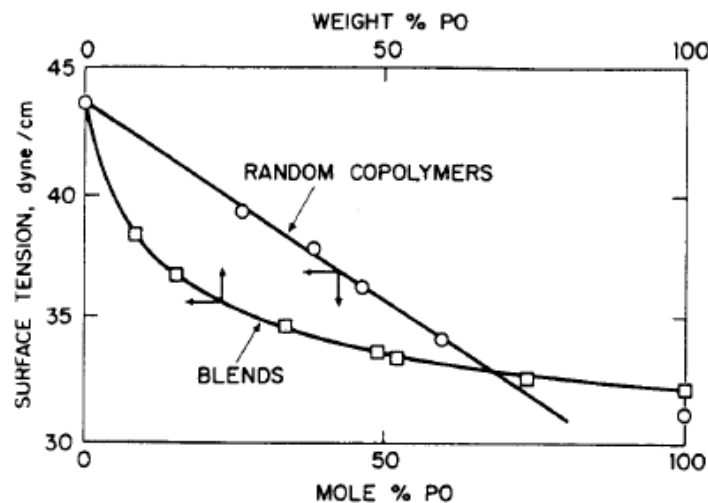


Figure 2-10. Linear additivity of surface tension of random copolymers of ethylene oxide and propylene oxide, and surface-active behavior of blends of poly(ethylene oxide) (PEG 300) and poly(propylene oxide) (PPG 425). [41]

For instance, pronounced surface activity is observed for ABA block copolymers of ethylene oxide (A block, higher surface free energy) and propylene oxide (B block, lower surface free energy) (Figure 2-11). [41]

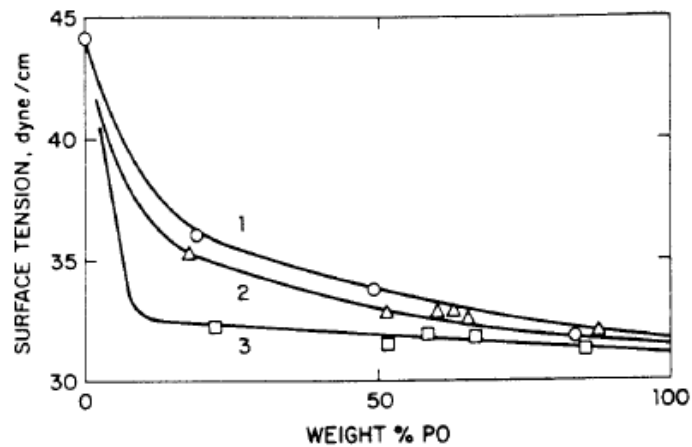
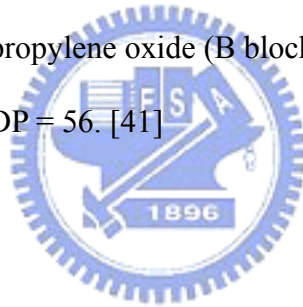


Figure 2-11. Surface tension versus composition for ABA block copolymers of ethylene oxide (A block) and propylene oxide (B block). Degree of polymerization are (1) DP = 16, (2) DP = 30, (3) DP = 56. [41]



Blends of Polymers

Blends of both compatible and incompatible polymers show pronounced surface activity, incompatible blends being more pronounced than compatible blends. The surface activity of an incompatible blends is further complicated by heterogeneous phase structure.

Surface activity of compatible blend of poly(ethylene oxide) and poly(propylene oxide) is shown in Figure 2-12. [41] The surface activity increases with increasing molecular weight, apparently because of increased in compatibility.

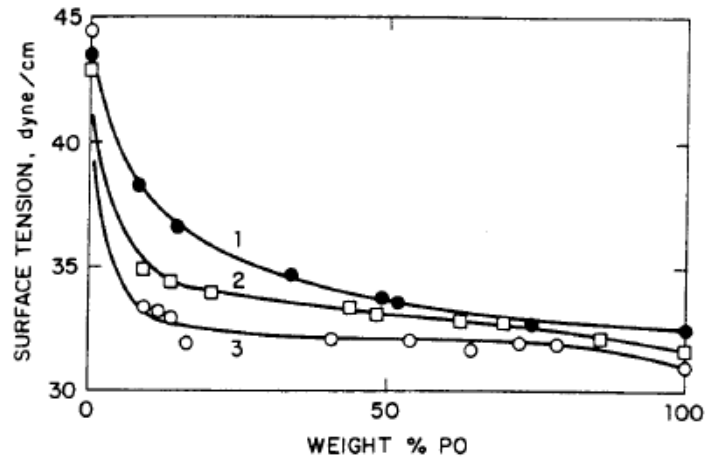


Figure 2-12. Surface tension of blends of compatible homopolymers. (1) poly(ethylene oxide) (PEG 300) + poly(propylene oxide) (PPG 425), (2) PPG 2025 + polyepichlorohydrin (PECH 1500), (3) PPG 400 + PECH 2000. [41]

2.2 Superhydrophobic Surfaces

Wettability is a fundamental property of a solid surface, which plays important roles in daily life, industry, and agriculture. Functional surfaces with special wettability have aroused much interest because of their great advantages in applications. For example, the superhydrophilic surface [42] with a water contact angle (CA) of almost 0° generated by UV irradiation has been successfully used as a transparent coating with antifogging and self-cleaning properties. On the other hand, various phenomena, such as contamination, snow sticking, erosion, and even current conduction are expected to be inhibited on superhydrophobic surfaces [43-46] with a CA larger than 150° and a sliding angle (SA) less than 10° . [47] The chemical compositions [48,49] determine the surface free energy and thus have great influence on wettability. However, it has certain limitation. For example, the $-CF_3$ - terminated surface was reported to possess the lowest free energy and the best hydrophobicity, while on flat surfaces, the maximum CA could only reach about 120° . [50] The

surface topographic structure is also an important factor that influences the wettability.

Conventionally, superhydrophobic surfaces have been produced mainly in two ways. One is to create a rough structure on a hydrophobic surface ($CA > 90^\circ$), and the other is to modify a rough surface by materials with low surface energy. Up to now, many methods have been developed to produce rough surfaces, including solidification of melted alkylketene dimmer (AKD, a kind of wax), [51] plasma polymerization/etching of polypropylene (PP) in presence of polytetrafluoroethylene (PTFE), [43] microwave plasma-enhanced chemical vapor deposition (MWPE-CVD) of trimethylmethoxysilane (TMMOS), [52] anodic oxidization of aluminum, [53] immersion of porous alumina gel films in boiling water, [54] mixing of a sublimation material with silica or boehmite, [55] phase separation, [56] and molding [57] To obtain superhydrophobic surfaces, coating with low-surface-free-energy materials such as fluoroalkylsilane (FAS) is often necessary. [53-57] While the water CA has commonly been used as a criterion for the evaluation of hydrophobicity of a solid surface, this alone is insufficient to assess the sliding properties of water droplets on the surface. [58] A fully superhydrophobic surface should exhibit both high CA and low sliding angle, where sliding angle can also be expressed as the difference between advancing and receding contact angle (hysteresis).

2.2.1 The Laws of Wetting

Young's Relation

Let us start with the academic case of a drop deposited on an ideal (i.e. homogeneous) solid (Figure 2-13). The drop contacts its substrate on a disc of radius l , whose border is a line (the so-called contact line) where the three phases of the

system coexist. Close to this line, and whatever the size of the drop, we can observe that the liquid joins the solid at an angle θ , whose value defines the size, l , of the contact.

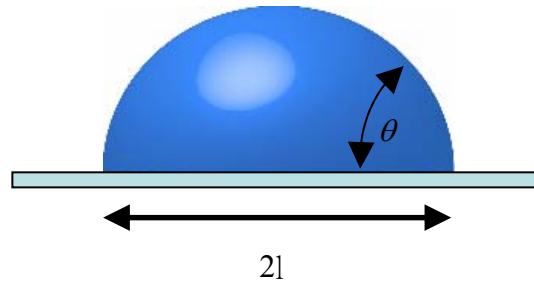


Figure 2-13. Liquid droplet on a solid. The liquid contacts the solid over a zone of size l , and joins it at an angle θ .

The value of the contact angle was first discussed by Young. [2] Each interface draws the contact line so as to minimize the corresponding surface area, so that balancing the surface tensions on the direction of potential motion (i.e. the horizontal) yields a relation attributed to Young (although it does not explicitly show up in Young's paper):

$$\gamma_{LV} \cos \theta = \gamma_{SV} - \gamma_{SL} \tag{2.5}$$

Equation (2.5) can alternatively be derived by calculating the variation of surface energy associated with a motion dx of the contact line (Figure 2-14).

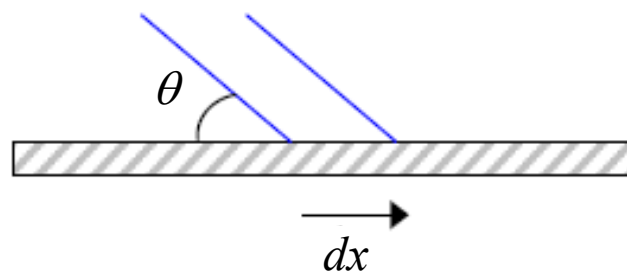


Figure 2-14. Displacing the contact line by a quantity dx (keeping the drop volume unchanged) modifies the surface area of each interface (solid/liquid, solid/vapor, liquid/vapor).

We find

$$dE = (\gamma_{SL} - \gamma_{SV})dx + \gamma dx \cos \theta \quad (2.31)$$

At equilibrium, E is minimum, which indeed yields equation (2.5).

From Complete Wetting to Complete Drying

Depending on the values of the different surface tensions (which are typically in the range of 20 to 500 mNm⁻¹ for pure liquids or solids), an angle may or may not be deduced from equation (2.5). Two limits are particularly interesting:

(a) If $(\gamma_{SV} - \gamma_{SL})$ is larger than γ_{LV} , the drop tends to spread completely on the solid, and the contact angle is considered as null ($\theta = 0^\circ$). As first identified by Marangoni, this condition (which can also be written $\gamma_{SV} > \gamma_{SL} + \gamma_{LV}$) indicates that the solid lowers its (surface) energy by being wetted. [59] Complete wetting happens for solids of high surface energy, such as glass or noble metals—but such solids often get polluted by aerosols (which wet them), so that their actual surface energy often decreases with time (and at the same time, these solids lose their ideality). This is the case with glass, which is wetted by water when it comes fresh out of a factory, but only shows partial wetting later, in most cases. Cleaning the glass very efficiently (with a strong acid) allows it to recover (transiently) a complete hydrophilicity. Complete wetting will also be observed with liquids of low surface tension ($\gamma_{LV} = \gamma_{SV}$), such as light alkanes or silicone oils, which wet completely glass, steel and most plastics. Surfactants, which lower the liquid/vapor surface tension, are often added to a paint to increase its wettability, in order to make the film of paint stable.

A drop deposited on a solid that it wets completely will spread spontaneously, and the question of the final contact (i.e. the size l) it develops with its substrate has been discussed extensively over the last 20 years. We could think that the final stage

of the drop is a monomolecular pancake (which defines l for a given volume), but long range forces may thicken this pancake (in particular close to the wetting transition, where the spreading force, $\gamma_{SV} - \gamma_{SL} - \gamma_{LV}$, vanishes). [60]

(b) If $(\gamma_{SL} - \gamma_{SV})$ is larger than γ_{LV} , the drop should be in a pure non-wetting situation ($\theta = 180^\circ$). This can be easily observed by inverting the two fluids in a complete wetting situation (inverting indices L and V in equation (2.5) transforms θ in $\pi - \theta$): silicone oil wets most solids, so that an air bubble injected in a box filled with silicone oil will join the box ceiling at a contact angle of 180° . However, the important case of a solid which will not be wetted at all by water (with air around) cannot be achieved: on the most hydrophobic solids we know (waxes, or fluorinated materials such as Teflon), water drops make contact angles of the order of 120° or 130° , quite far from the maximum value of 180° . [61] One of our aims in this review is to show the different tricks which allow us to approach this limit, and to quantify the (expected) reduction of adhesion of the drops in such a limit.

2.2.2 Natural Examples

Several natural materials exhibit super-hydrophobicity, with advancing contact angles between 150° and 165° . Neinhuis and Barthlott reported that this is the case for the leaves of about 200 plants, including asphodelus, eucalyptus, euphorbia, Indian Cress, Lady's Mantle, lotus and tulipa (Figure 2-15). [62-64] These surfaces have generally three common features: (a) they are coated by an epicuticular film of wax, or by wax crystalloids, making them hydrophobic (Young contact angle greater than 90°); (b) they are decorated by textures such as bumps, at a scale of typically $10\mu\text{m}$; (c) a secondary texture, of much smaller size (about $1\mu\text{m}$ in many cases) and different morphology (often hairs) is superimposed on the first one. [62-64]

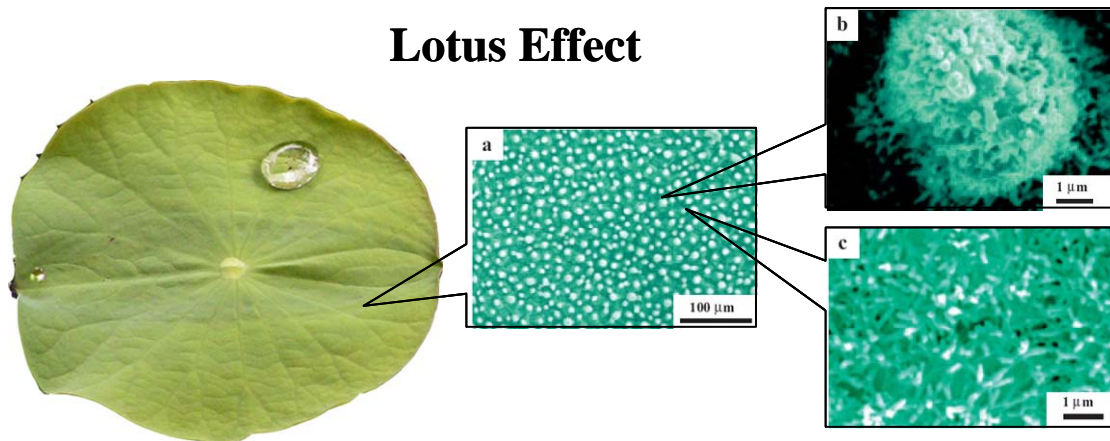


Figure 2-15 Water droplets on lotus [65]

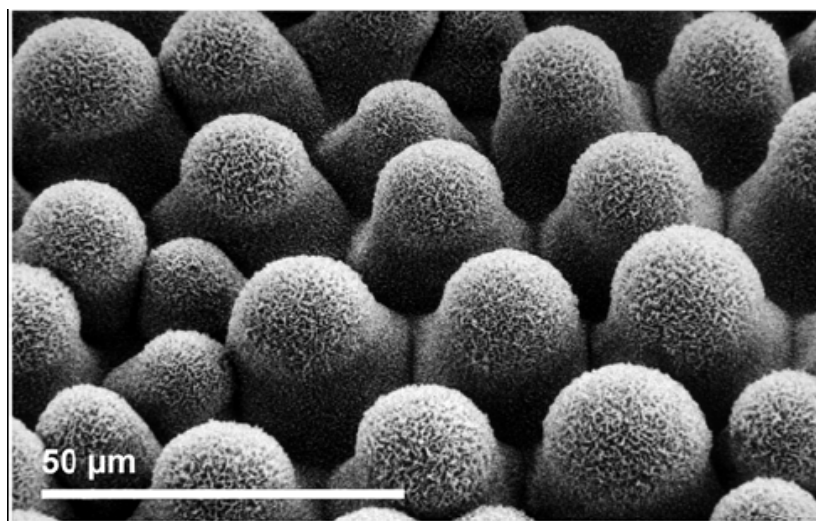


Figure 2-16. SEM picture of a super-hydrophobic plant (*Colocasia esculenta*). The surface is structured at two levels: bumps at a scale of $20\ \mu\text{m}$ and hairs at a scale of $1\ \mu\text{m}$. These structures together with the wax which coats the leaf provide super-hydrophobicity. [65]

Figure 2-16 shows as an example the upper surface of a leaf of *Colocasia esculenta* (Araceae), also called elephant ear, as observed under scanning electron microscopy (SEM)

Similarly, animals can be super-hydrophobic, owing to micro-structures at a scale between $100\ \text{nm}$ and several micrometres. This is the case for example for water

strider legs (Figure 2-17), butterfly wings (and indeed lepidopter means ‘having wings with scales’) (Figure 2-18), duck feathers and some bugs. [66-68] In many cases, this is a strategy for allowing a safe interaction with water: a duck coming out of water immediately de-wets, and water striders are supported by the surface of a pond. Butterflies close their wings during the night, and dew condensation between the wings would stick them together if they were wettable. There is a Namibian beetle (Figure 2-19), *Stenocara*, which has a different reason for having part of its elytrae super-hydrophobic [69]: it survives in very desert areas, where water is only obtainable from a morning fog. Little spots in the elytrae are hydrophilic, so that the drops condense and grow there; once they are large enough, they detach and roll down the tilted beetle, following super-hydrophobic tracks (which, as we shall show, ensures a quick transportation without leakage) till they reach the beetle’s mouthparts.



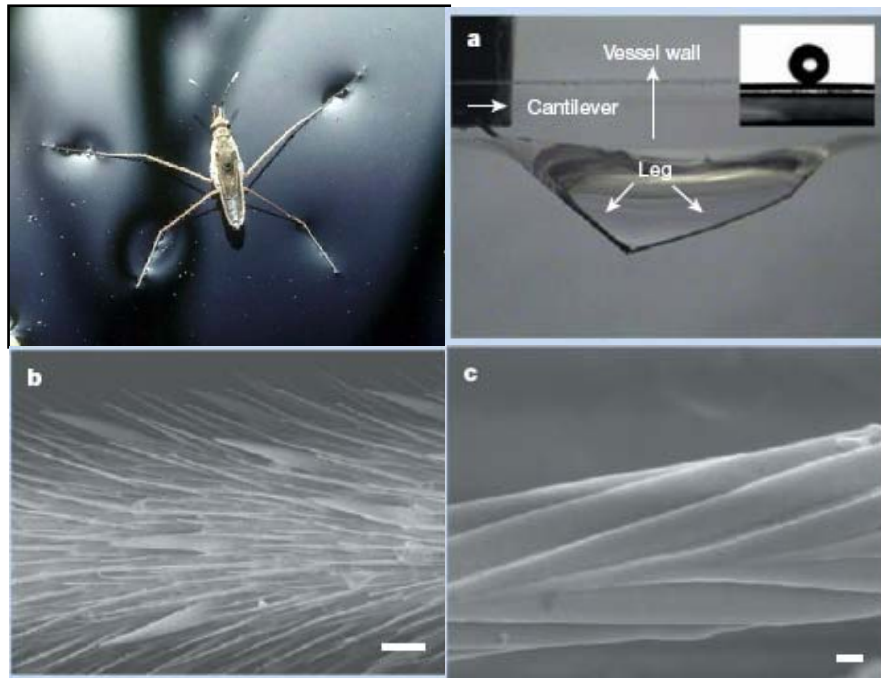


Figure 2-17. The non-wetting leg of a water strider. (a) Typical side view of a maximal-depth dimple (4.38 mm) just before the leg pierces the water surface. Inset, water droplet on a leg; this makes a contact angle of 167.6° . (b), (c), Scanning electron microscope images of a leg showing numerous oriented spindly microsetae (b) and the fine nanoscale grooved structures on a seta (c). Scale bars: b, $20\ \mu\text{m}$; c, $200\ \text{nm}$.

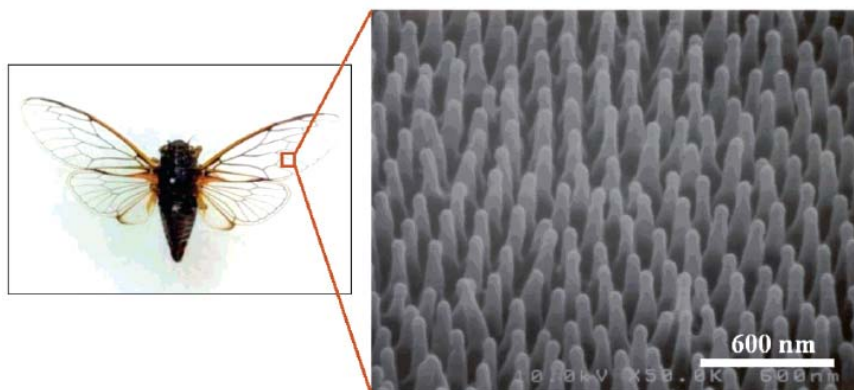


Figure 2-18. FE-SEM micrograph of the wing surface of *Cicada orni* with regularly aligned nanoposts.

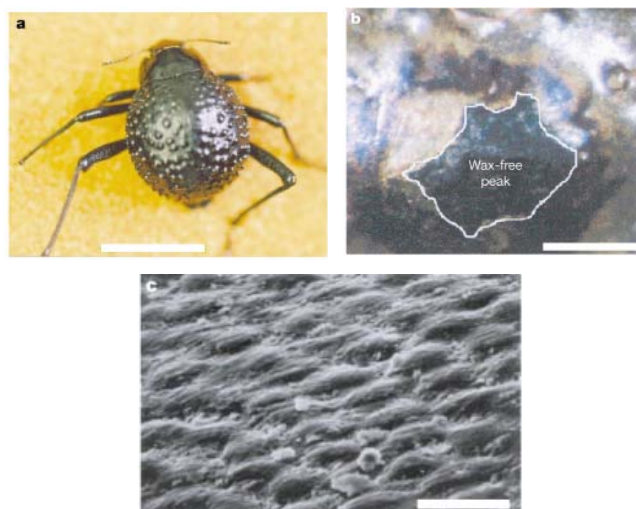


Figure 2-19. The water-capturing surface of the fused overwings (elytra) of the desert beetle *Stenocara* sp. (a) Adult female, dorsal view; peaks and troughs are evident on the surface of the elytra. (b) A ‘bump’ on the elytra, stained with Red O for 15 min and then with 60% isopropanol for 10 min, a procedure that tests for waxes. Depressed areas of the otherwise black elytra are stained positively (waxy, coloured), whereas the peaks of the bumps remain unstained (wax-free; black). (c) Scanning electron micrograph of the textured surface of the depressed areas. Scale bars, (a) 10 mm; (b) 0.2 mm; (c) 10 μ m.

As a conclusion, all these natural materials clearly show that the hydrophobicity of a solid is enhanced by textures. We further examine what the mechanisms are of this effect and propose partial answers to the (open) question of why double structures are often present. But we first describe how many synthetic super-hydrophobic materials have been developed (in particular in the past few years) and discuss their properties.

2.2.3 Synthetic Substrates

Many synthetic materials have been developed like these natural examples in order to obtain water-repellency. Some applications are quite obvious: stone, wood

and concrete need to be protected from the effects of rain. In other cases (fabrics), we need enhanced water-proofing. One can also try to get rid of droplets which affect the transparency of glass (window panes, windshields, greenhouses) or reflection (mirror). It is also expected (or hoped) that a water-repellent substrate will be anti-frost and anti-dew. But one of the most important properties of these substrates is their ability to let liquids move very quickly on them: this can be extremely interesting in microfluidic devices, where we often desire a reduction of the friction associated with a flow. This also explains why these materials are often referred to as self-cleaning: raindrops are efficiently removed, taking with them the dirt particles which were deposited on the solids [70]. We can see the same phenomenon when pouring liquid nitrogen on the ground: the very mobile drops take with them the dust present on the surface, the particles lowering interfacial energy by adsorbing at the interface. Many of the plants which are super-hydrophobic indeed look cleaner because of this effect— which could be one of the reasons for the reverence of the lotus in India.

One method to improve the liquid repellency of a surface is to combine a suitable chemical structure (surface energy) with a topographical microstructure (roughness); previous attempts have included preparing fractal surface (Figure 2-20), [51] plasma treating polymer surfaces, [71, 72] preparing gel-like roughened polymers through solvent processing (Figure 2-21), [73] preparing roughened block copolymers through solvent processing (Figure 2-22), [74] densely packing aligned carbon nanotubes [75-77] and preparing aligned polyacrylonitrile nanofibers (Figure 2-23). [78] Both super-hydrophobic and super-amphiphobic surfaces can result from increased surface roughness; this effect occurs naturally on the lotus leaf, for example. [73, 79] The surfaces of these leaves possess a micron-level roughness covered with nano-sized crystals of wax; [78] the water contact angles of these leaves

can be as high as 160° because air is trapped between the water droplets and the wax crystals at the plant surface to minimize the contact area. [80]

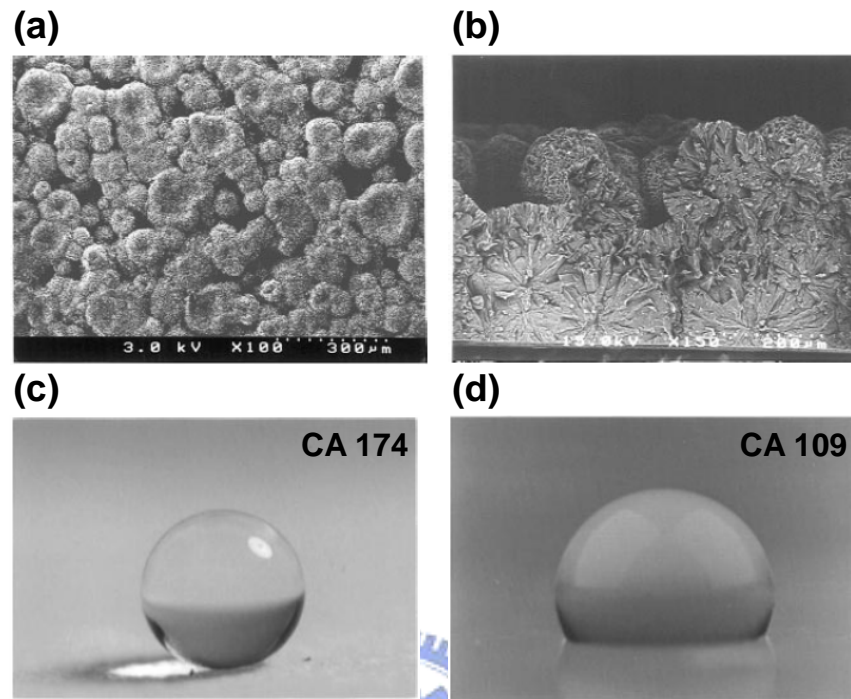


Figure 2-20. SEM images of the fractal alkylketene dimmer (AKD) surface: (a,) top view, (b) cross section. Water droplet on AKD surfaces: (c) fractal AKD surface; (d) flat AKD surface. [51]

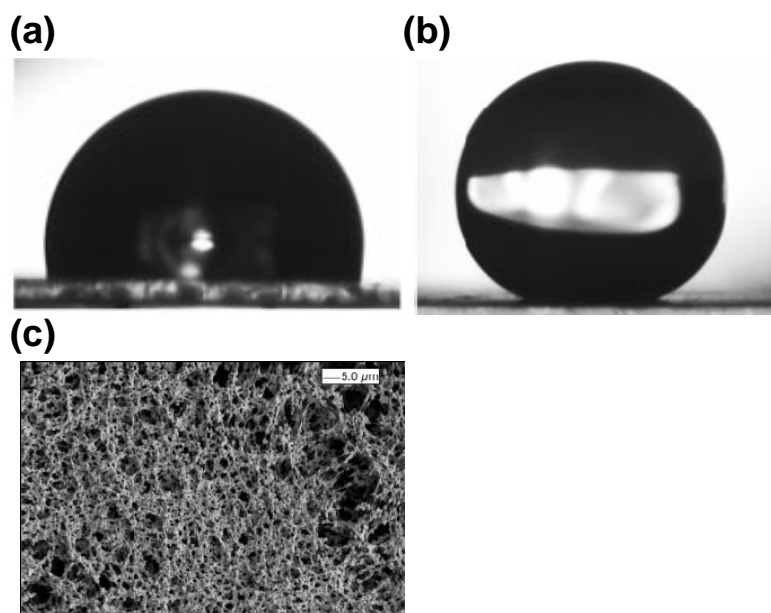


Figure 2-21. The profile of a water drop on (a) a smooth i-PP surface ($CA = 104^\circ$), (b) a superhydrophobic i-PP coating on a glass slide ($CA = 160^\circ$). (c) SEM picture of a superhydrophobic i-PP film. [73]

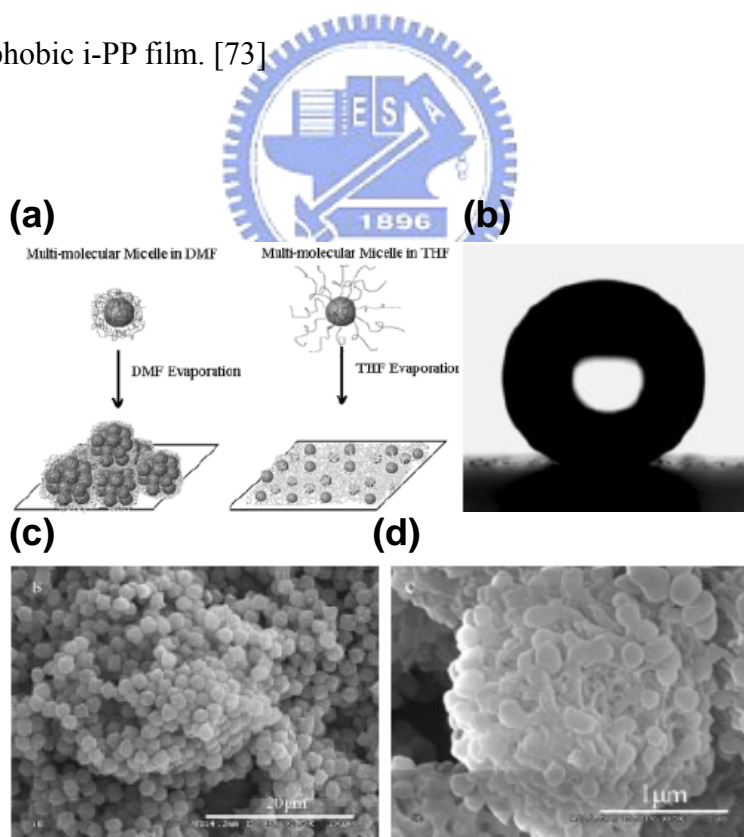


Figure 2-22. (a) Illustration of the solvent effect on the morphologies of PP-PMMA copolymer surface. (b) The profile of a water drop on superhydrophobic polymer surface. (c) SEM images of superhydrophobic polymer. (d) Enlarged view of (c). [74]

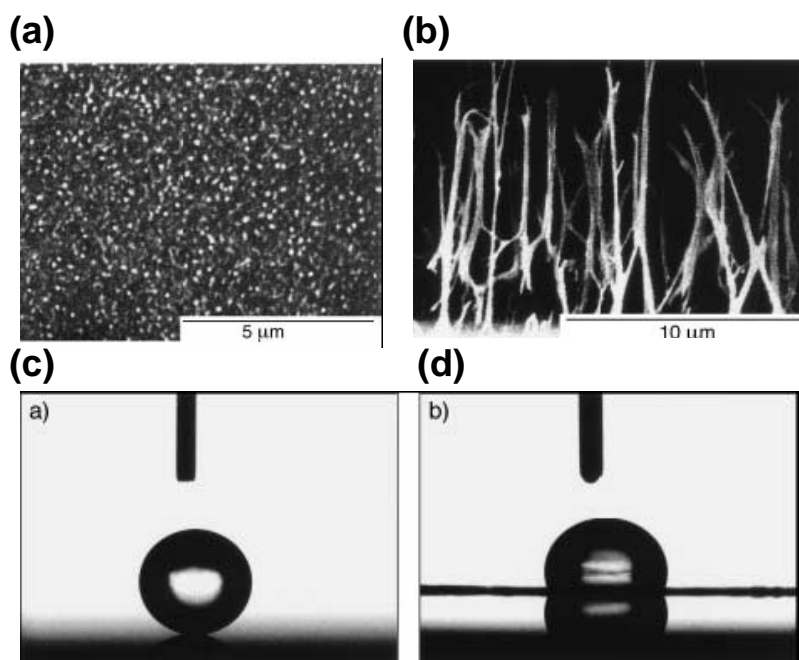


Figure 2-23. SEM images of (a) surface of the PAN nanofibers; (b) cross-sectional view of the as-synthesized PAN nanofibers. Shapes of water droplets on (c) the PAN nanofibers with a rough surface; (d) the native PAN film with smooth surface. [79]

Whatever its nature, natural or artificial, regularly patterned or highly disordered, a structured hydrophobic material is super-hydrophobic. This property a priori sounds interesting, since it should provide a strong reduction of adhesion of the drops—but the situation is not that simple: we saw that in some cases the hysteresis of the contact angle can be extremely small, which defines a slippery surface, but that in other cases this quantity can be large, which implies a sticky state (in spite of a very high contact angle), of less obvious practical interest. We now give some hints about the mechanisms responsible for these different effects, and stress in particular that indeed two different super-hydrophobic states can exist and even coexist.

2.2.4 Models

The Wenzel Equation

The first attempt to understand the effect of roughness on wettability is that of Wenzel (1936). Wenzel was interested in ways of improving the water-proofing of fabrics, which are naturally textured materials (at the scale of the monofilaments which make the yarns). [81] He had noticed that the natural tendency of a material (hydrophilic or hydrophobic) is enhanced by the presence of textures. Wenzel's interpretation of these facts is based on the increasing of the surface area of a material because of its roughness: a liquid will tend to spread more on a rough hydrophilic substrate, since it allows it to develop more solid/liquid contact (which is favorable in a hydrophilic situation). Conversely, a rough hydrophobic material appears (apparently) more hydrophobic, because the liquid would have to develop a much larger (unfavorable) contact with the solid if the contact angle is kept unchanged.

The key parameter is thus the roughness factor, defined by Wenzel as the ratio of the true surface area A (taking into account the peaks and valleys on the surface) to the apparent surface area A' is defined as the roughness factor $r = A/A'$. It is thus a dimensionless number, larger than unity, and all the larger since the surface is rough. The main assumption of Wenzel is that the liquid follows the defects of the solid surface, as it is deposited on it. The apparent contact angle is the one which minimizes the (surface) energy of the drop as shown in Figure 2-24.

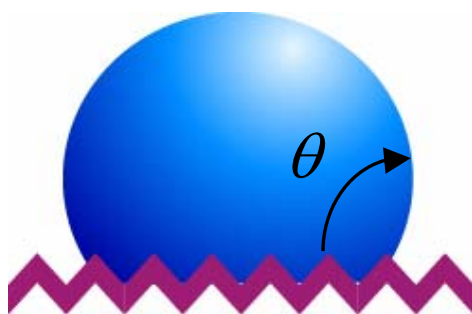


Figure 2-24. The Wenzel state: the liquid follows the solid surface.

For $r = 1$ (flat solid), we get back Young's law (equation (2.5)). For a rough surface ($r > 1$), we derive Wenzel's relation: [81, 82]

$$\cos \theta_w = r \cos \theta \quad (2.36)$$

In Eq. (2.36), θ is the intrinsic CA on a smooth surface, θ_w is that on a rough surface made of the same material, and r is the roughness factor. The Wenzel relation qualitatively agrees with the main observations: both hydrophobicity and hydrophilicity are enhanced by roughness, since we deduce from equation (2.36) that increasing surface roughness results in actual CA decrease for hydrophilic materials ($\theta < 90^\circ$) and increase for hydrophobic materials ($\theta > 90^\circ$). This looks like a simple and attractive solution for inducing superhydrophobicity: the rougher the material, the higher the contact angle. However, this is not that simple, for two reasons: firstly, contact angles generally spread in quite a large interval, contrasting with equation (2.36) which predicts a unique angle. This interval, often referred to as the contact angle hysteresis, is responsible for the sticking of drops, an effect in contradiction with water repellency. In a Wenzel state, the contact angle hysteresis will be very large: trying to remove a liquid makes it contact itself (owing to the fraction left in the textures), which yields a low "receding" contact angle—values as low as 40° were reported, making this state hydrophilic-like in the receding stage. [83]

The second reason which makes it impossible to reach high values of θ_w , as expected from equation (2.36) for r large and $\theta > 90^\circ$, can be guessed quite easily: for very rough hydrophobic materials, the energy stored for following the solid surface is much larger than the energy associated with the air pockets sketched in Fig. 2-25. [83-86]

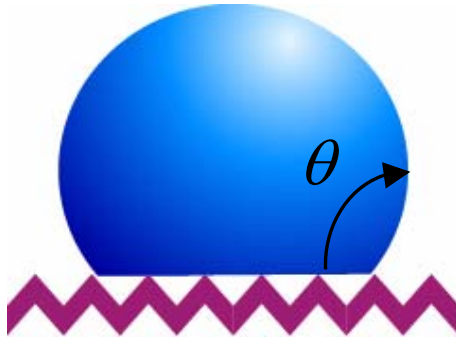


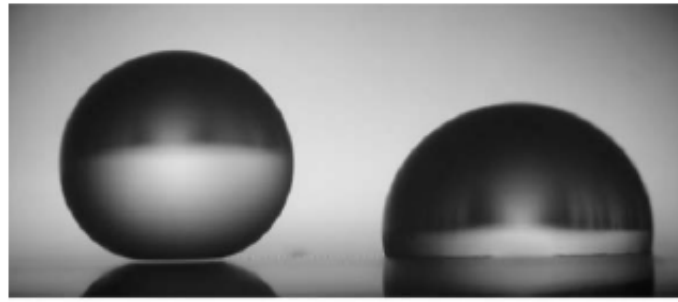
Figure 2-25. The Cassie state, the liquid only contacts the top of the asperities, leaving air below.

The Cassie and Baxter Equation

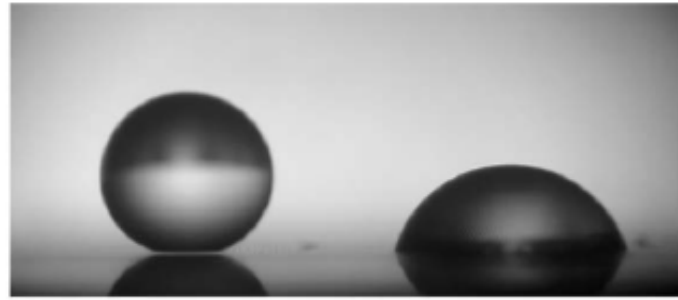
In Cassie and Baxter state (Figure 2-25), the liquid only contacts the solid through the top of the asperities, on a fraction that we denote as f_1 . [80] If only air were present between the solid and the liquid (as for a water drop on a very hot plate), the “contact angle” would be 180° : the smaller f_1 , the closer to this extreme situation, and thus the higher the hydrophobicity. More precisely, the contact angle θ_c of such a “fakir” drop (Figure 2-24) is an average between the angles on the solid (of cosine $\cos \theta$), and on the air (of cosine -1), respectively weighed by the fractions f_1 and $1 - f_1$, which yields:

$$\cos \theta_c = f_1(\cos \theta + 1) - 1 \quad (2.37)$$

For $\theta = 110^\circ$ and $f_1 = 10\%$, we find that θ_c is about 160° . In this case, 90% of the drop base contacts air! This makes it understandable that the corresponding hysteresis is observed to be very low (typically around 5 to 10°), as first reported by Johnson and Dettre: [88] the liquid has very little interactions with its substrate. Hence, this state will be the (only) repellent one, since it achieves both a large contact angle and a small hysteresis (this can be observed further, in Figure 2-26).



(a)



(b)

Figure 2-26. Millimetric water drops (of the same volume) deposited on a superhydrophobic substrate consisting of dilute pillars ($f_1 = 0.01$). (a) The right drop has been pressed, which induced a Wenzel state, characterized by a smaller angle (the roughness is very low, and equal to 1.1). The light passes below the left drop, indicating a Cassie state. (b) Ten minutes later, the drop volumes have decreased, owing to evaporation, and angles became receding ones. The difference of hysteresis between both states is clearly visible: the Wenzel drop even became hydrophilic

θ_c monotonously increases as f_1 decreases, suggesting that f_1 should be made as small as possible. But reducing f_1 also makes the roughness decrease, so that we reach the critical roughness γ_c below which the Wenzel state is favoured. The quantity r_c is easily deduced from the intersection of equation (2.36) and (2.37), and is found to be $(f_1 - 1)/\cos\theta + f_1$, which is generally close to $-1/\cos\theta$ (since we will often have: $f_1 = 1$). For $\theta = 120^\circ$ (a high value for the Young angle, obtained on fluorinated substrates), the fakir state will thus be favored for roughness factors larger than 2. Conversely, Öner and McCarthy experimentally observed that below a critical

density of defects (i.e. below a critical roughness), there is indeed a serious deterioration of the water-repellent properties. [89]



2.3 Wettability Pattern and Wettability gradient

The surface and interfacial properties of materials are directly related to their surface energies. Current approaches toward engineer tunable surfaces include light irradiation and UV thermal treatment, acidification, and applying electrical potentials, among others. Intra- and intermolecular interactions play important roles in determining the surface properties of polymers. Structured surfaces that exhibit lateral patterns of varying wettability have received extensive attention because it can apply as preparing fluid microchips and the periodical arrangements of metallic nanoparticles or nanowires and self-assembly of block copolymer or carbon nanotubes. Besides, a gradient surface displays a gradual change in the chemical and physical properties along its length. has a wide range of applications in material science. A gradient in a surface can induce the net mass transport of liquids, which affords a driving force for operation of microfluidic devices and for biological cell motility in vitro. We would further describe how wettability pattern, wettability gradient and the periodical arrangements of metallic nanoparticles, nanowires and carbon nanotubes were prepared. But we describe how the wettability of surface was affect by UV, thermal treatment, pH value and applying electrical potentials first.

2.3.1 Methods to Control the Wettability of Surface

Wettability is a very important property governed by both the chemical composition and the geometrical structure of solid surfaces. Super-hydrophobic surface (with water contact angle (CA) larger than 150°) and super-hydrophilic surfaces (CA close to 0°) have been extensively investigated due to their importance for industrial applications. Recently, smart surfaces with tunable wettability have aroused great interest because of their myriad applications as biosensors, microfluidic

devices, intelligent membranes, and so on. [90, 91] Current approaches toward engineer tunable surfaces include UV, [92, 93] thermal treatment, [94, 95] acidification, [96-98] and applying electrical potentials, [99, 100] among others. [101, 102]

Among these method, UV approach to control the wettability of surface is the most way which was used. Jiang et al. reported the wettability of aligned ZnO nanorod films could be controlled by UV illumination. [92] From Figure 2-27, reversible super-hydrophobicity to super-hydrophilicity transition on aligned ZnO nanorod films was observed and intelligently controlled by alternation of UV illumination and dark storage. Besides, Cho et al. reported a facile method for the fabrication of a wetting surface that is photoswitchable from superhydrophobicity to superhydrophilicity, which combines layer-by-layer assembly and the introduction of photoresponsive moieties onto the top surface (Figure 2-28). [103] This strategy can be extended to other stimuli-responsive surfaces with similar nanostructure and higher stability, which is certainly significant for future industrial applications.

There are a number of thermal approaches have been employed to control the wettability of surface. For example, Jiang et al. [94] reported on the use of poly(N-isopropylacrylamide) (PNIPAAm) grafted to texture surfaces formed by microlithography to generate the surfaces with reversibly transition behavior between the temperature above the lower critical solution temperature (LCST) and the temperature below the LCST. The rough surface structures enhanced thermally responsive wettability of a PNIPAAm-modified surface. Reversible switching between superhydrophilicity and superhydrophobicity can be achieved in a narrow temperature range of about 10°C (Figure 2-29), which is considered to result from the combined effect of the chemical variation of the surface, and surface roughness. Such

switchable surfaces may have wide applications in functional textiles, intelligent microfluidic switching, controllable drug release, and thermally responsive filters. Besides, Jiang et al. have also reported that wettability of surface could be control by pH value. [104] Stable superhydrophobic or superhydrophilic colloidal crystal films have been successfully fabricated under ambient conditions from an amphiphilic material of poly-(St-MMA-AA) in the presence of hydrogen bonding or not (Figure 2-30).The consistent hydrogen-bonding network in the films contributes to the stable superhydrophobicity, while the absence of the hydrogen bonding leads to superhydrophilicity.

Choi et al. have reported that the design of surfaces that exhibit dynamic changes in interfacial properties, such as wettability, in response to an electrical potential (Figure 2-31). The change in wetting behavior was caused by surface-confined, single-layered molecules undergoing conformational transitions between a hydrophilic and a moderately hydrophobic state. [99]

Except UV, thermal treatment, pH value and electrical potential, solvent treatment is another approach to control the wettability of surface. Minko et al. have reported a route to fabricate two-level structured self-adaptive surfaces (SAS) of polymer materials as shown in Figure 2-32. [105] The first level of structure is built by a rough polymer film that consists of needlelike structures of micrometer size. The second level of structure is formed by the nanoscopic self-assembled domains of a demixed polymer brush irreversibly grafted onto the needles. By exposing the surface to solvents that are selective to one of the components of the brush, we reversibly tune the surface properties. The large scale surface structure amplifies the response and enables us to control wettability, adhesion, and chemical composition of the surface over a wide range.

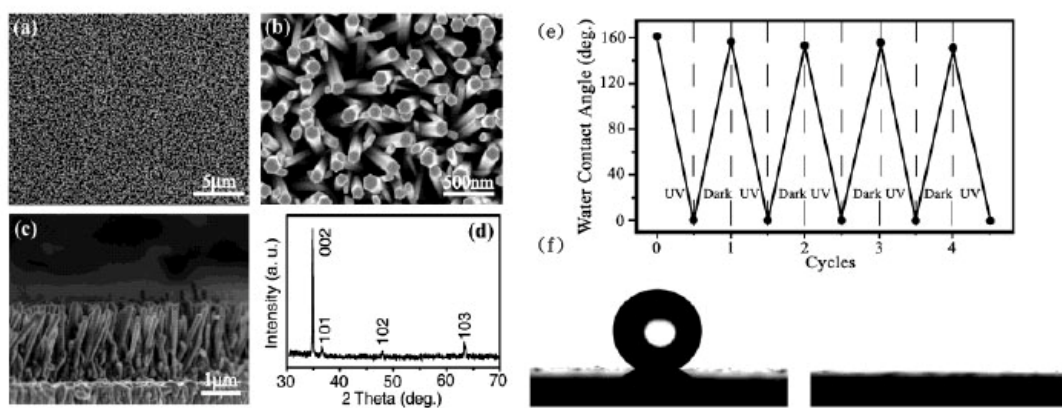


Figure 2-27. (a, b) FE-SEM top-images of the as-prepared ZnO nanorod films at low and high magnifications, respectively. (c) Cross-sectional view of the aligned ZnO nanorods. (d) XRD pattern of the as-synthesized nanorod films. (e) Reversible super-hydrophobic-super-hydrophilic transition of the as-prepared films under the alternation of UV irradiation and dark storage. (f) Photographs of water droplet shape on the aligned ZnO nanorod films before (left) and after (right) UV illumination. [92]



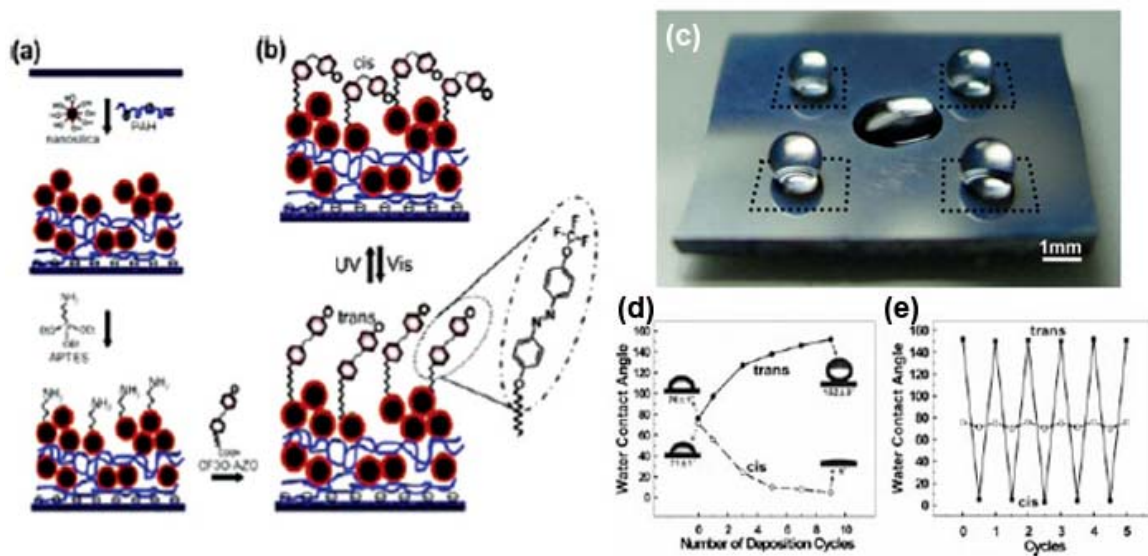


Figure 2-28. (a) Fabrication and (b) Reversible Photoisomerization of a Roughness-Enhanced Photoswitchable Surface (c) photographs of substrates with patterned extreme wetting properties; angled views of water droplet profiles on the patterned substrate as a result of selective UV irradiation. (d) The relationships between the number of deposition cycles and the water contact angles: water droplet profiles on the smooth substrate (dotted arrows) and on the (PAH/SiO₂) 9 multilayer film (solid arrows) after UV/visible irradiation. (e) Reversible wettability transitions of a smooth substrate (□) and a (PAH/SiO₂) 9 multilayer film (■).

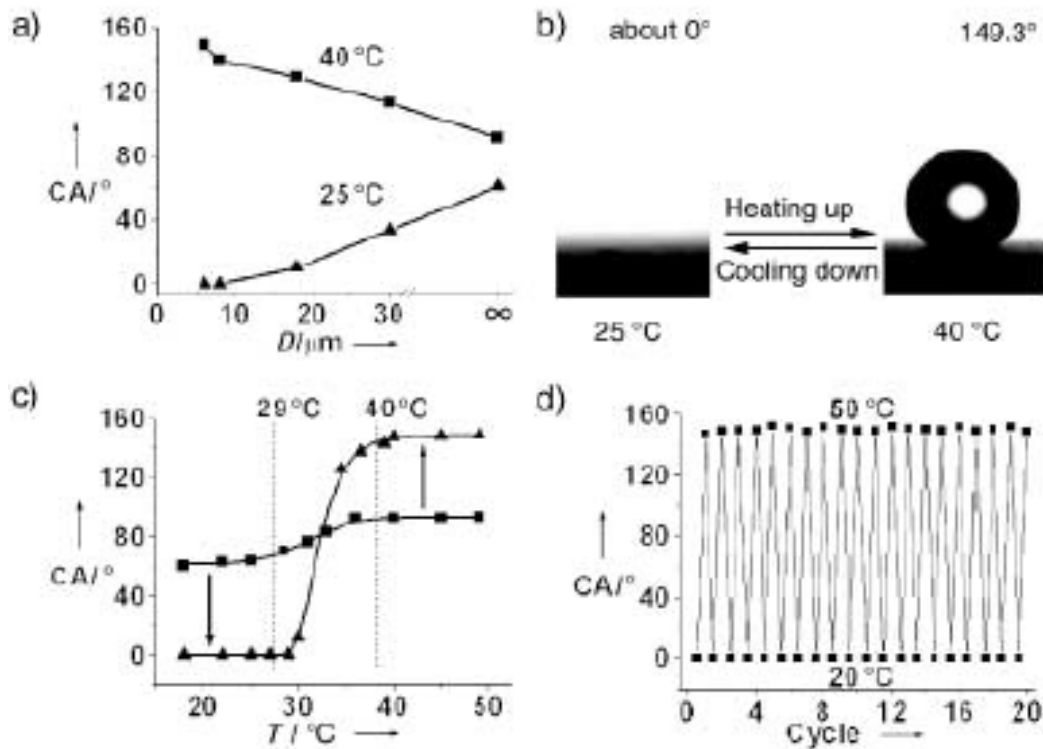


Figure 2-29. Surface-roughness-enhanced wettability of a PNIPAAm-modified surface. (a) The relationships between groove spacing (D) of rough surfaces and the water CAs at low temperature (triangles, 25°C) and at high temperature (squares, 40°C). The groove spacing of ∞ represents flat substrate. (b) Water drop profile for thermally responsive switching between superhydrophilicity and superhydrophobicity of a PNIPAAm-modified rough surface with groove spacing of about $6\mu\text{m}$, at 25°C and 40°C . The water CAs are about 0° and $149.3 \pm 2.5^\circ$, respectively. (c) Temperature (T) dependences of water CAs for PNIPAAm thin films on a rough substrate with groove spacing of about $6\mu\text{m}$ (triangles) and on flat substrate (squares). (d) Water CA in at two different temperatures for a PNIPAAm-modified rough substrate with groove spacing of $6\mu\text{m}$. [94]

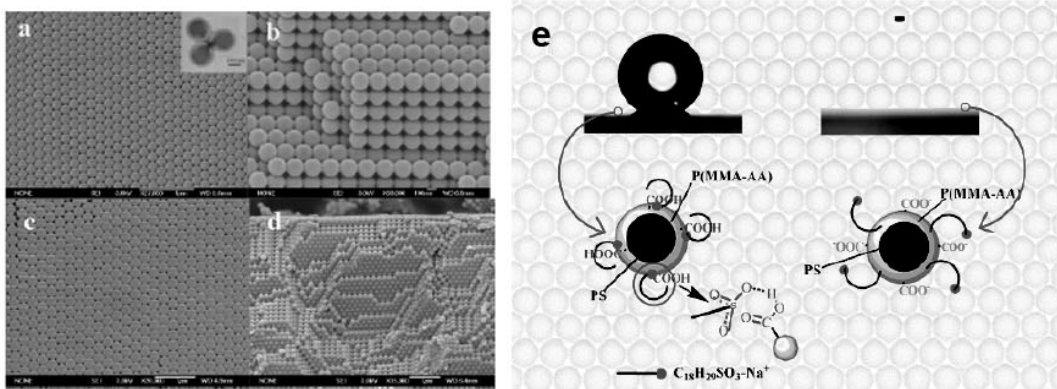
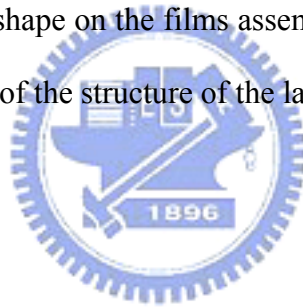


Figure 2-30. Typical comparison of SEM images of the colloidal crystal film assembly at different pH values. (a, b) Top view and side view of the films assembled at pH = 6.0. (c, d) Top view and side view of the film assembled at pH = 12.0. (Inset: typical TEM image of core-shell spheres of poly-(St-MMA-AA); the bar is 100 nm. (e) Photographs of water droplet shape on the films assembled from suspensions with pH of 6.0 and 12 and illustrations of the structure of the latex sphere in the films. [104]



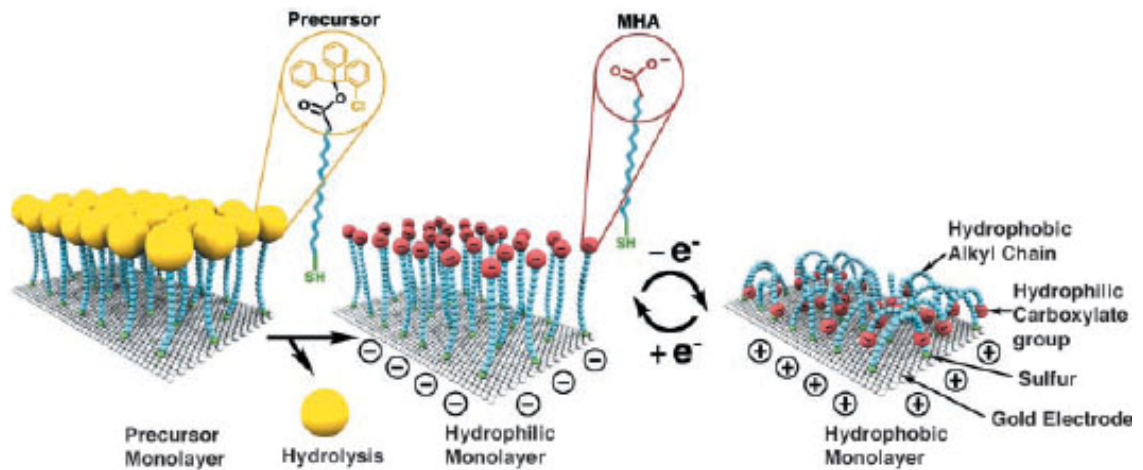


Figure 2-31. Idealized representation of the transition between straight (hydrophilic) and bent (hydrophobic) molecular conformations (ions and solvent molecules are not shown). The precursor molecule MHAE, characterized by a bulky end group and a thiol head group, was synthesized from MHA by introducing the (2-chlorophenyl)diphenylmethyl ester group. [99]



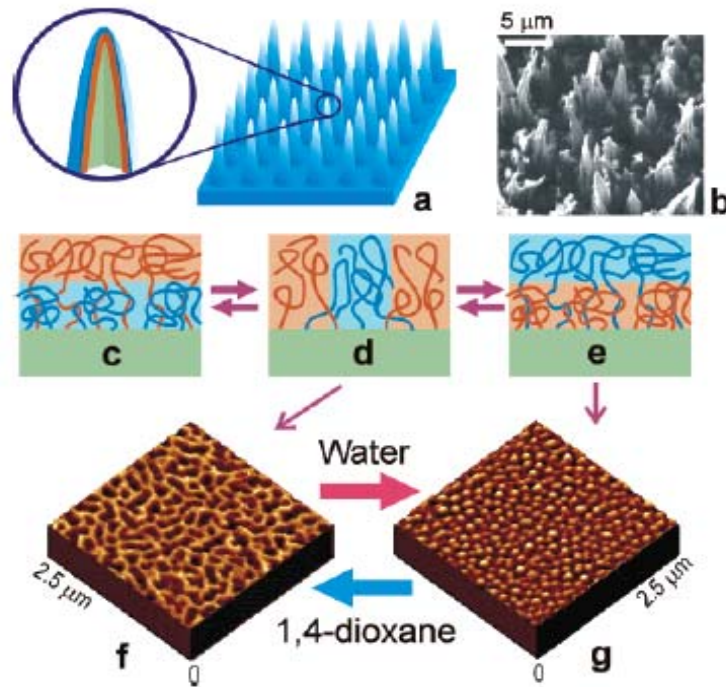


Figure 2-32. Two-level structure of self-adaptive surfaces (SAS): Schematic representation of needlelike surface morphology of the PTFE surface (first level) (a) and SEM image of the PTFE film after 600 s of plasma etching (b). Each needle is covered by a covalently grafted mixed brush that consists of hydrophobic and hydrophilic polymers (second level) depicted schematically in panels c-e. Its morphology results from interplay between lateral and vertical phase segregation of the polymers, which switches the morphology and surface properties upon exposure to different solvents. In selective solvents the preferred polymers preferentially occupies the top of the surface (c and e), while in nonselective solvents, both polymers are present in the top layer (d). The lower panels (f and g) show AFM images (model smooth substrate) of the different morphologies after exposure to different solvents. [105]

2.3.2 Fabrication of wettability pattern and periodic array of colloidal nanocrystals

The development of highly parallelizable means of creating ordered assemblies of colloidal particles of micrometer to nanometer length scales is a recent focus of research. Electrostatically guided deposition of particles on patterned substrates is one means of creating ordered structures. In this technique, patterned surfaces containing charged and uncharged regions are created by soft lithography to pattern alkanethiols on gold, [106] by photolithography to pattern siloxane layers on glass, [107, 108] by layer by layer adsorption of polyelectrolytes, [109] or by creating holes in an insulating substrate formed using a focused ion beam. [110] Colloidal particles bearing charge of the opposite sign of the patterned patches are then exposed to those regions. The particles adsorb to the charged regions via columbic interactions and pack to form arrays of single particles or multiple particles, depending upon the relative size of the particles to the charged regions. In the case of multiple particles adsorbing on a site, the particles, which in general are well-wet by the suspending fluids, are pulled into ordered structures in the late stages of fluid evaporation by the contraction of capillary bridges connecting them. Evaporation also provides a means of collecting particles near three-phase contact lines and so has been exploited as a means of particle self-assembly. Stebe et al. reported that ordered arrays of particles were created spontaneously by evaporative deposition of colloidal suspensions on surfaces of patterned wetting from parent drops with diameters large compared to the length scale of the underlying pattern (Figure 2-33). [111] Jonas et al. also reported 2D structured colloidal crystals can be obtained on chemically patterned surfaces by evaporative deposition of colloidal suspensions (Figure 2-34). [112] Furthermore, Zhang et al. demonstrated the fabrication of metallic photonic crystals, in the form of

a periodic array of gold nanowires on a waveguide, by spin coating a colloidal gold suspension onto a photoresist mask and subsequent annealing (Figure 2-35). This alternative method for fabricating metallic photonic crystals possessed advantages of simplicity, high speed, and low cost. [113] From recent report, the selective placement and alignment of individual SWCNTs could be also achieved on UV patterning surface (Figure 2-36). [114]

Surfaces with extreme wetting properties such as superhydrophilic patterns on a superhydrophobic surface offer new possibilities in the fabrication of novel devices such as planar microcanals (open-air microfluidic channels). [115] Open-air microfluidic channels offer advantages such as the facile handling of small amount of liquids, the possibility of massive parallel processing, direct accessibility, and ease of cleaning. [115-117] The availability of patterned surfaces with superhydrophobic and superhydrophilic regions can greatly enhance the utility and function of such devices and move us beyond nature's impressive accomplishment with the Namib beetle. Lee et al. introduced a direct ultraviolet (UV)-assisted replica molding method for creating a biomimetic hierarchical structure and its use for selectively transforming the superhydrophobic surface to a superhydrophilically patterned surface on large area, regardless of the type of substrate (Figure 2-37). [118]

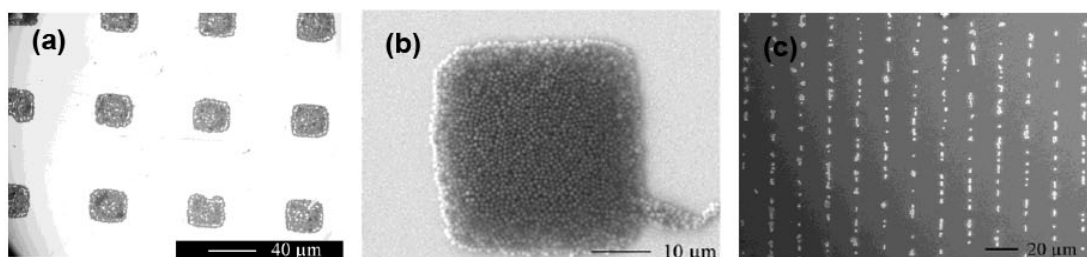


Figure 2-33. Colloidal particles assembled on 50 μm carboxylic acid terminated square patterned surfaces on a continuous methylterminated surface at $\text{pH}=2$, 24.5°C , 21% humidity. (a) An optical micrograph of 0.8 μm amidine functionalized microspheres deposited at 0.1% volume fraction. (b) SEM image. (c) An SEM image of 0.8 μm microspheres assembled on a surface patterned with alternating 5 μm carboxylic acid terminated stripes and 5 μm methyl terminated stripes at $\text{pH}=2$, 24.5°C , 21% humidity, and 0.01% volume fraction. [111]



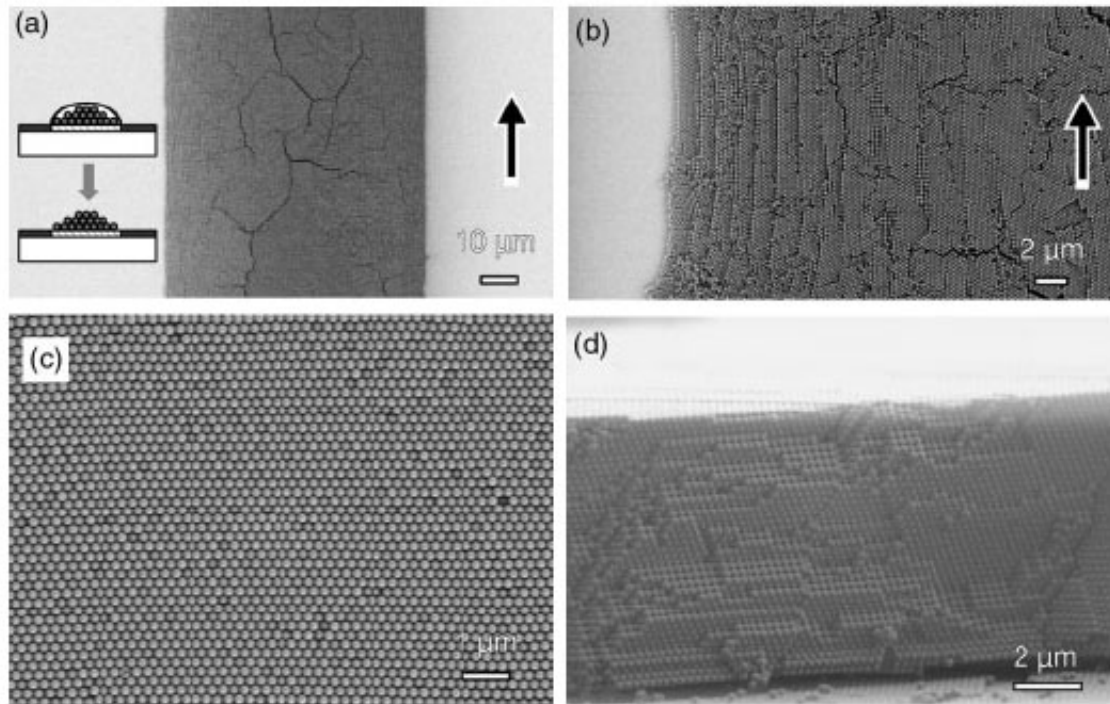


Figure 2-34. (a), (b) LVSEM image at higher magnification showing the stepwise increase of the thickness from the edge to the center of the stripe. (c) LVSEM image of the topmost layer showing the excellent crystal quality. (d) LVSEM image of the cross-section through a colloidal crystal stripe. [112]

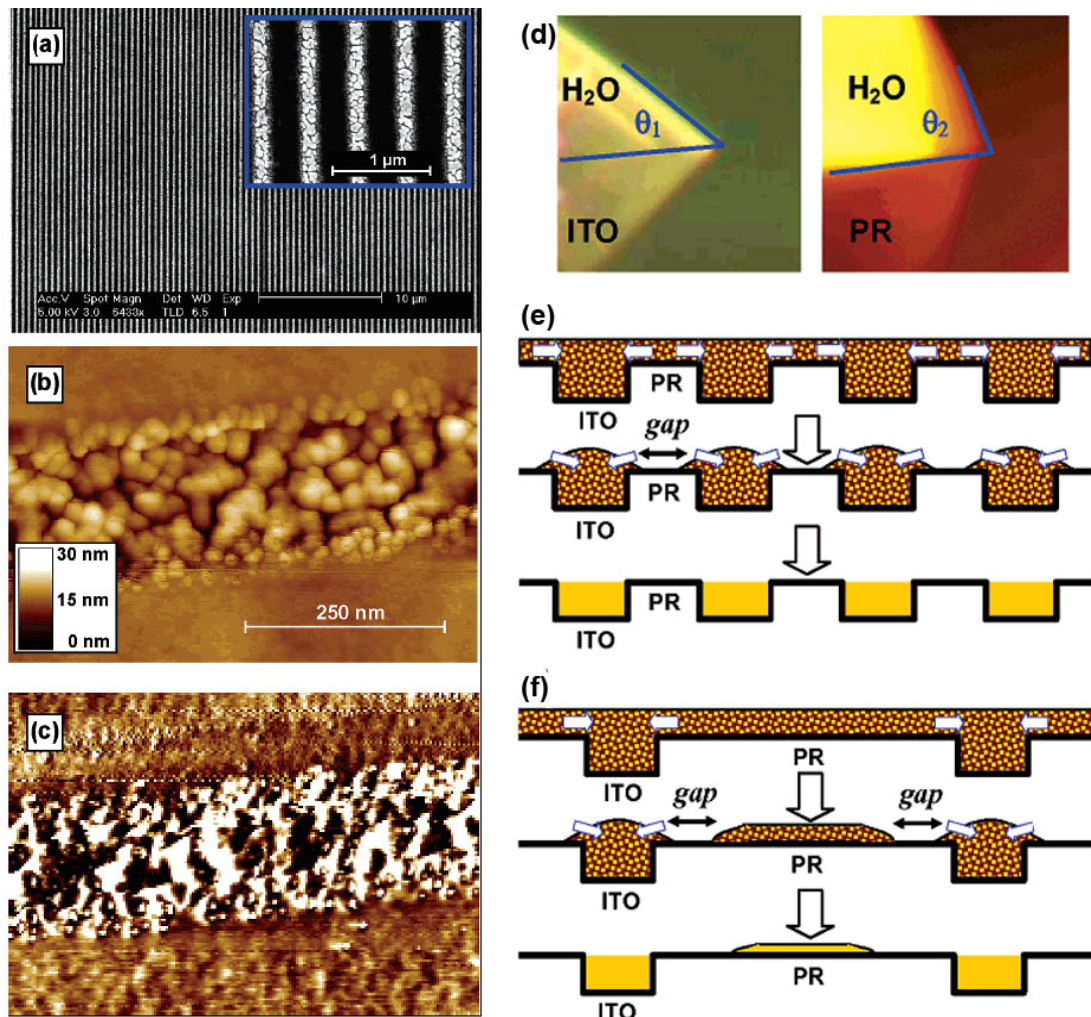


Figure 2-35. (a) SEM Images of the gold photonic crystal structures, (b) AFM height image of the gold photonic crystal structures, (c) AFM phase image of the gold photonic crystal structures, (d) Measurements of contact angles of water on the ITO and on the PR surfaces: $\theta_1 = 44-45^\circ$, $\theta_2 = 73-75^\circ$. (e) Mechanisms for the confinement of the gold nanoparticles into the grating grooves when the PR channel is small enough. (f) Two gaps will form for structures with large PR channel. [113]

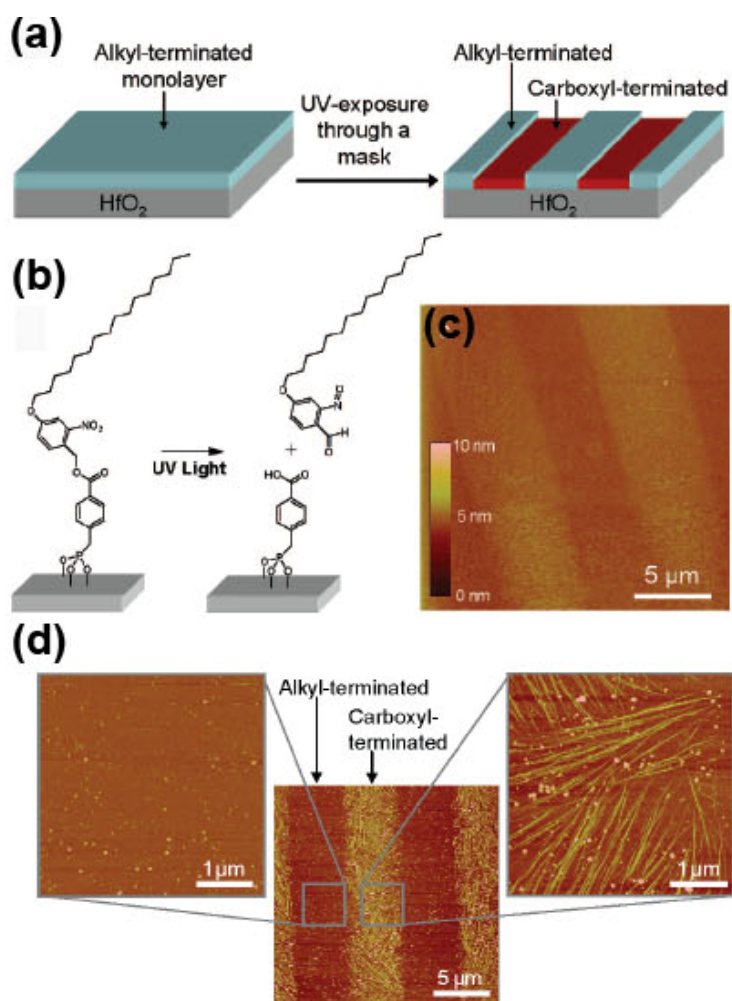


Figure 2-36. (a) Illustration of creating the photopatterned monolayer, (b) illustration of the UV-induced reaction of SAM 6 and (c) AFM image of the photopatterned monolayer surface. (d) AFM image of the UV-patterned HD-UV-PA-modified surface after drop-casting SWCNTs from a H₂O/methanol solution (3:1 volume). The higher resolution images on the left and right illustrate the high selectivity of the deposition. [114]

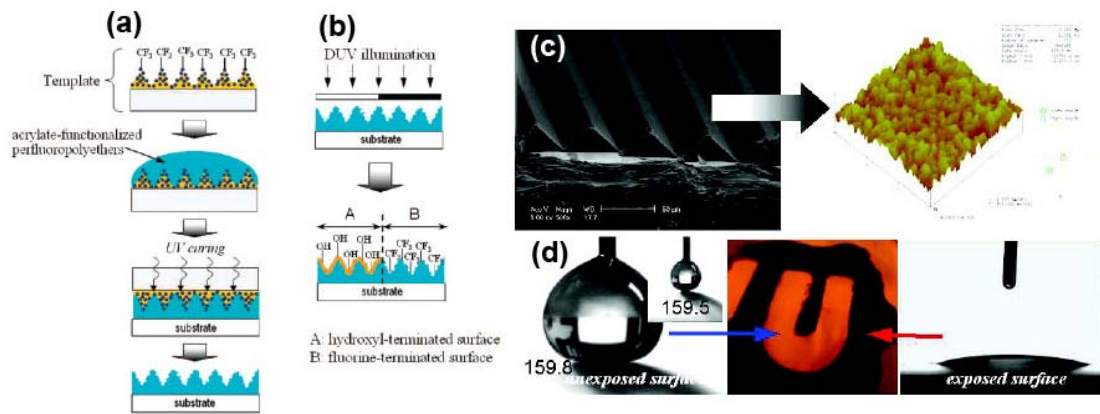


Figure 2-37. (a) Fabrication of a Biomimetic Dual-Scale Hierarchical Structure by Direct UV-Replica Molding with the Template and (b) Fabrication of Selectively Wetting Surface (c) SEM and AFM image of the template with dual-scale roughness (d) Selective wetting of water on the DUV-modified surface obtained with a SUS mask. [118]



References

- [1] Dupré, A. *Theorié mécanique de la chleur*, Paris, **1869**, p.368.
- [2] Young, T. *Phil Trans. R. Soci. Lond.* **1805**, 95, 65.
- [3] Michaelis, A. S.; Dean, Jr. S. W. *J. Phys. Chem.* **1962**, 66, 34.
- [4] Baily, G. L. J. *Proc. 2nd Int. Congr. Surf. Act.* **1957**, 3, 189.
- [5] Poynting, J. H.; Thompson, J. J. *A Textbook of Physics: Properties of Matter*, 8th ed., Charles Griffin, London, **1920**.
- [6] Girifalco, L. A.; Good, R. J. *J. Phys. Chem.* **1957**, 61, 904.
- [7] Good, R. J.; Girifalco, L. A.; Kraus, G. *J Phys. Chem.* **1957**, 62, 1418.
- [8] Good, R. J.; Girifalco, L. A. *J. Phys. Chem.* **1960**, 64, 561.
- [9] Fowkes, F. W. *Contact Angle, Wettability and Adhesion, Advances in Chemistry Series 43*, R. F. Gould, Ed., American Chemical Society, Washington, DC, **1964**, p. 99.
- [10] Fowkes, F. W. in *Adhesion and Adsorption of Polymers, Polymer Science and Technology*, vol. 12A, L. H. Lee, Ed., Plenum Press, New York, **1980**, p. 43.
- [11] Owens, D. K.; Wendt, R. C. *J. Appl. Polym. Sci.* **1969**, 13, 1741.
- [12] Kaelble, D. H. *J. Adhesion* **1970**, 2, 50.
- [13] Wu, S. *J. Polym. Sci., C* **1971**, 34, 19.
- [14] Wu, S. *Adhesion and Adsorption of Polymers, Polymer Science and Technology*, vol. 12A, L. H. Lee, Ed., Plenum Press, New York, **1980**, p. 53.
- [15] Fowkes, F. M.; Mostafa, M. A. *Int. Eng. Chem. Prod. Res. Dev.* **1978**, 17, 3.
- [16] Fowkes, F. M.; McCarthy, D. C.; Mostafa, M. A. *J. Colloid Interface Sci.* **1980**, 78, 200.
- [17] van Oss, C. J.; Chaudhury, M. K.; Good, R. J. *Chem. Rev.* **1988**, 88, 927.
- [18] van Oss, C. J.; Ju, L.; Chaudhury, M. K.; Good, R. J. *J. Colloid Interface Sci.*

1989, 128, 313.

- [19] van Oss, C. J.; Good, R. J. *J. Macromol. Sci. Chem.* **1989**, A26, 1183.
- [20] van Oss, C. J. *J. Dispers. Sci. Technol.* **1990**, 11, 491.
- [21] van Oss, C. J.; Arnold, K.; Good, R. J.; Gawrisch, K.; Ohki, S. *J. Macromol. Sci. Chem.* **1990**, A27, 563.
- [22] van Oss, C. J.; Good, R. J.; Busscher, H. J. *J. Dispers. Sci. Technol.* **1990**, 11, 75.
- [23] van Oss, C. J.; Giese, Jr., R. F.; Good, R. J. *Langmuir* **1990**, 6, 1711.
- [24] Good, R. J.; van Oss, C. J. in *Modern Approaches to Wettability*, M. E. Schrader and G. I. Loeb, Eds., Plenum Press, New York, **1992**, p. 1.
- [25] Good, R. J. in *Contact Angle, Wetting, and Adhesion*, K. L. Mittal, Ed., VSP, xxx, **1993**, p. 3.
- [26] Fox, H. W.; Zisman, W. A. *J. Colloid Sci.* **1950**, 5, 514.
- [27] Fox, H. W.; Zisman, W. A. *J. Colloid Sci.* **1952**, 7, 109.
- [28] H. W. Fox, W. A. Zisman, *J. Colloid Sci.* **1952**, 7, 428.
- [29] Weisenhorn, A. L.; Maivald, P.; Butt, H.-J.; Hansma, P. K. *Phys. Rev. B* **1992**, 45, 11226.
- [30] Israelachvili, J. N. *Intermolecular and Surface Forces*, 2nd ed.; Academic Press: London, 1992.
- [31] Johnson, K. L.; Kendall, K.; Roberts, A. D. *Proc. R. Soc. London, Ser. A* **1971**, 324, 301.
- [32] Noy, A.; Vezenov, D. V.; Lieber, C. M. *Annu. Rev. Mater. Sci.* **1997**, 27, 381.
- [33] Kawai, A.; Nagata, H.; Takata, M. *Jpn. J. Appl. Phys.* **1992**, 31, L977.
- [34] Kawai, A.; Nagata, H.; Morimoto, H.; Takata, M. In *Surface Modification Technologies VII*; Proc. 7th Int.
- [35] Sudarshan, T. S., Ishizaki, K., Takata, M., Kamata, K., Eds.; Sanjo, Niigata,

Japan, 31 Oct-2 Nov **1993**.

- [36] Tan, S.; Sherman Jr. R. L.; Ford, W. T. *Langmuir* **2004**, *20*, 7015
- [36] LeGrand, D. G.; Gaines, Jr., G. L. *J. Colloid Interface Sci.* **1969**, *31*, 162.
- [37] LeGrand, D. G.; Gaines, Jr., G. L. *J. Colloid Interface Sci.* **1973**, *42*, 181.
- [38] Wu, S. *J. Colloid Interface Sci.* **1969**, *31*, 153.
- [39] Wu, S. *J. Macromol. Sci.* **1974**, *C10*, 1.
- [40] Schonhorn, H.; Ryan, F. W. *J. Phys. Chem.* **1966**, *70*, 3811.
- [41] Rastogi, A. K.; Pierre, L. E. *St. J. Colloid Interface Sci.* **1969**, *31*, 168.
- [42] Wang, R.; Hashimoto, K.; Fujishima, A.; Chikuni, M.; Kojima, E.; Kitamura, A.; Shimohigoshi, M.; Watanabe, T. *Nature* **1997**, *388*, 431.
- [43] Chen, W.; Fadeev, A. Y.; Hsieh, M. C.; Öner, D.; Youngblood, J.; McCarthy, T. J. *Langmuir* **1999**, *15*, 3395.
- [44] Feng, L.; Li, S.; Li, Y.; Li, H.; Zhang, L.; Zhai, J.; Song, Y.; Liu, B.; Jiang, L.; Zhu, D. *Adv. Mater.* **2002**, *14*, 1857.
- [45] Blossey, R. *Nat. Mater.* **2003**, *2*, 301.
- [46] Lafuma, A.; Quéré, D. *Nat. Mater.* **2003**, *2*, 457.
- [47] Nakajima, A.; Fujishima, A.; Hashimoto, K.; Watanabe, T. *Adv. Mater.* **1999**, *11*, 1365.
- [48] Woodward, J. T.; Gwin, H.; Schwartz, D. K. *Langmuir* **2000**, *16*, 2957.
- [49] Sun, T.; Song, W.; Jiang, L. *Chem. Commun.* **2005**, 1723.
- [50] Nishino, T.; Meguro, M.; Nakamae, K.; Matsushita, M.; Ueda, Y. *Langmuir* **1999**, *15*, 4321.
- [51] Onda, T.; Shibuichi, S.; Satoh, N.; Tsujii, K. *Langmuir* **1996**, *12*, 2125.
- [52] Wu, Y.; Sugimura, H.; Inoue, Y.; Takai, O. *Chem. Vap. Deposition* **2002**, *8*, 47.
- [53] Tsujii, K.; Yamamoto, T.; Onda, T.; Shibuchi, S. *Angew. Chem. Int. Ed. Engl.*

1997, 36, 1011.

- [54] Tadanaga, K.; Katata, N.; Minami, T. *J. Am. Ceram. Soc.* **1997**, 80, 3213.
- [55] Nakajima, A.; Fujishima, A.; Hashimoto, K.; Watanabe, T. *Adv. Mater.* **1999**, 11, 1365.
- [56] Nakajima, A.; Abe, K.; Hashimoto, K.; Watanabe, T. *Thin Solid Films* **2000**, 376, 140.
- [57] Bico, J.; Marzolin, C.; Quéré, D. *Europhys. Lett.* **1999**, 47, 220.
- [58] Miwa, M.; Nakajima, A.; Fujishima, A.; Hashimoto, K.; Watanabe, T. *Langmuir* **2000**, 16, 5754.
- [59] Marangoni, C. *Ann. Phys. Chem.* **1871**, 143, 337.
- [60] Gennes, P. G. De. *Rev. Mod. Phys.* **1985**, 57, 827.
- [61] Shafrin, E. G.; Zisman, W. A. *Contact Angle, Wettability and Adhesion (Advances in Chemistry Series vol 43)* (Washington, DC: American Chemical Society) 1964 pp 145
- [62] Neinhuis, C.; Barthlott, W. *Ann. Bot.* **1997**, 79, 667.
- [63] Neinhuis, C.; Barthlott, W. *Planta* **1997**, 202, 1.
- [64] Otten, A.; Herminghaus, S. *Langmuir* **2004**, 20, 2405.
- [65] Wagner, P.; Fürstner, R.; Barthlott, W.; Neinhuis, C. *J. Exp. Bot.* **2003**, 54, 1.
- [66] Wagner, T.; Neinhuis, C.; Barthlott, W. *Acta Zool.* **1996**, 3, 213.
- [67] . Lee, W; Jin, M. K.; Yoo, W. C.; Lee, J. K. *Langmuir* **2004**, 20, 7665.
- [68] Gao, X.; Jiang, L. *Nature* **2004**, 432 36.
- [69] Parker, A. R.; Lawrence, C. R. *Nature* **2001**, 414, 33
- [70] Blossey, R. *Nat. Mater.* **2003**, 2, 301.
- [71] Morra, M.; Occhiello, E.; Garbassi, F. *Langmuir* **1989**, 5, 872.
- [72] Woodward, I.; Schofield, W. C. E.; Roucoules, V.; Badyal, J. P. S. *Langmuir*

2003, 19, 3432.

- [73] Erbil, H. Y.; Demirel, A. L.; Avci, Y.; Mert, O. *Science* **2003**, 299, 1377.
- [74] Xie, Q.; Fan, G.; Zhao, N.; Guo, X.; Xu, J.; J Dong,.; Zhang, L.; Zhang, Y.; Han, C. C. *Adv. Mater.* **2004**, 16, 302.
- [75] Lau, K. K. S.; Bico, J.; Teo, K. B. K.; Chhowalla, M.; Amaratunga, G. A. J.; Milne, W. I.; McKinley, G. H.; Gleason, K. K. *Nano. Lett.* **2003**, 3, 1701.
- [76] Feng, L.; Li, S.; Li, Y.; Li, H.; Zhang, L.; Zhai, J.; Song, Y.; Liu, B.; Jiang, L.; Zhu, D. *Adv. Mater.* **2002**, 14, 1857.
- [77] Li, H.; Wang, X.; Song, Y.; Liu, Y.; Li, Q.; Jiang, L.; Zhu, D. *Angew. Chem. Int. Ed.* **2001**, 40, 1743.
- [78] Feng, L.; Li, S.; Li, H.; Zhai, J.; Song, Y.; Jiang, L.; Zhu, D. *Angew. Chem. Int. Ed.* **2002**, 41, 1221.
- [79] Neinhuis, C.; Barthlott, W. *New Phytologist* **1998**, 138, 91.
- [80] Herminghaus, S. *Europhys. Lett.* **2000**, 52, 165.
- [81] Wenzel, R. N. *Ind. Eng. Chem.* **1936**, 28, 988.
- [82] Wenzel, R. N. *J. Phys. Chem.* **1949**, 53, 1466.
- [83] Lafuma, A.; Quéré, D. *Nat. Mater.* **2003**, 2, 457.
- [84] Bico, J.; Thiele, U.; Quéré, D. *Colloids Surf. A* **2002**, 206, 41.
- [85] Patankar, N. *Langmuir* **2003**, 19, 1249.
- [86] Marmur, A. *Langmuir* **2003**, 19, 8343.
- [87] Cassie, A. B. D.; Baxter, S. *Trans. Faraday Soc.* **1944**, 40, 546.
- [88] Johnson, R. E.; Dettre, R. H. in *Contact angle, Wettability and Adhesion, Advances in Chemistry Series, American Chemical Society, Washington DC, 1964*, vol. 43, pp. 112–135.
- [89] Öner, D.; McCarthy, T. J. *Langmuir* **2000**, 16, 7777.

- [90] Russell, T. P. *Science* **2002**, 279, 964.
- [91] Sun, T.; Feng, L.; Gao, X.; Jiang, L. *Acc. Chem. Res.* **2005**, 38, 644
- [92] Feng, X.; Feng, L.; Jin, M.; Zhai, J.; Jiang, L.; Zhu, D. B. *J. Am. Chem. Soc.* **2004**, 126, 62-63.
- [93] Lahann, J.; Mitragotri, S.; Tran, T.; Kaido, H.; Sundaram, J.; Choi, I. S.; Hoffer, S.; Somorjai, G. A.; Langer, R. *Science* **2003**, 299, 371-374.
- [94] Sun, T.; Wang, G.; Feng, L.; Liu, B.; Ma, Y.; Jiang, L.; Zhu, D. *Angew. Chem. Int. Ed.* **2004**, 43, 357-360.
- [95] Fu, Q.; Rama Rao, G. V.; Basame, S. B.; Keller, D. J.; Artyushkova, K.; Fulghum, J. E.; López, G. P. *J. Am. Chem. Soc.* **2004**, 126, 8904-8905.
- [96] Ionov, L.; Houbenov, N.; Sidorenko, A.; Stamm, M.; Luzinov, I.; Minko, S. *Langmuir* **2004**, 20, 9916-9919.
- [97] Yu, X.; Wang, Z.; Jiang, Y.; Shi, F.; Zhang, X. *Adv. Mater.* **2005**, 17, 1289-1293
- [98] Choi, Se-Jin; Suh, K. Y.; Lee, H. H. *J. Am. Chem. Soc.* **2008**, 130, 6312-6313.
- [99] Lahann, J.; Mitragotri, S.; Tran, T. N.; Kaido, H.; Sundaram, J.; Choi, I. S.; Hoffer, S.; Somorjai, G. A.; Langer, R. *Science* **2003**, 299, 3710.
- [100] Krupenkin, T. N.; Taylor, J. A.; Schneider, T. M.; Yang, S. *Langmuir* **2004**, 20, 3824-3827.
- [101] Ryu, D. Y.; Shin, K.; Drockenmuller, E.; Hawker, Craig J.; Russell, T. P. *Science* **2005**, 308, 236-239.
- [102] Minko, S.; Müller, M.; Motornov, M.; Nitschke, M.; Grundke, K.; Stamm, M. *J. Am. Chem. Soc.* **2003**, 125, 3896.
- [103] Lim, H. S.; Han, J. T.; Kwak, D.; Jin, M.; Cho, K. *J. Am. Chem. Soc.* **2006**, 128, 14458
- [104] Wang, J.; Hu, J.; Wen, Y.; Song, Y.; Jiang, L. *Chem. Mater.* **2006**, 18, 4984

- [105] Minko, S.; Müller, M.; Motornov, M.; Nitschke, M.; Grundke, K.; Stamm, M.
J. Am. Chem. Soc. **2003**, 125, 3896
- [106] Aizenberg, J.; Braun, P. V.; Wilzius, P. *Phys. Rev. Lett.* **2000**, 84, 2997.
- [107] Kruger, C.; Jonas, U. *J. Colloid Interface Sci.* **2002**, 252, 331.
- [108] Jonas, U.; Campo, A.; Kruger, C.; Glasser, G.; Boos, D. *Proc. Natl. Acad. Sci.*
2002, 99, 8.
- [109] Lee, I. L.; Zheng, H.; Rubner, M.; Hammond, P. *Adv. Mater.* **2002**, 14, 572.
- [110] Fudouzi, H.; Kbayashi, M.; Shinya, N. *Adv. Mater.* **2002**, 14, 1649.
- [111] Fan, F.; Stebe, K. J. *Langmuir* **2004**, 20, 3062
- [112] Fustin, C. A.; Classer, G.; Spiess, H. W.; Jonas, U. *Adv. Mater.* **2003**, 15, 1025
- [113] Zhang, X.; Sun, B.; Friend, R. H.; Guo, H.; Nau, D.; Giessen, H. *Nano Lett.*
2006, 6, 651
- [114] Bardecker, J. A.; Afzali, A.; Tulevski, G. S.; Graham, T.; Hannon, J. B.; Jen, A.
K. Y. *J. Am. Chem. Soc.* **2008**, 130, 7226-7227.
- [115] Gau, H.; Herminghaus, S.; Lenz, P.; Lipowsky, R. *Science* **1999**, 283, 46.
- [116] Hsu, C. H.; Chen, C.; Folch, A. *Lab Chip* **2004**, 4, 420.
- [117] Seemann, R.; Brinkmann, M.; Kramer, E. J.; Lange, F. F.; Lipowsky, R. *PNAS*
2005, 102, 1848.
- [118] Choi, S. J.; Suh, K. Y.; Lee, H. H. *J. Am. Chem. Soc.* **2008**, 130, 6312.

Chapter 3

Modification of Polymer Substrates with Low Surface Free Energy Material by Low-Temperature Curing

Polybenzoxazine

Abstract

The B-ala/AIBN PBZ system has a higher extent of the ring-opening of oxazine because phenol-containing oligomers are formed at the early stage of the curing process. As a result, the B-ala/AIBN PBZ system possesses a relatively stronger intramolecular hydrogen bonding and lower surface energy than the pure B-ala system at low temperature curing. In this context, Poly(4-vinyl pyridine), Poly(4-vinyl phenol) thin film and polycarbonate substrates which lack liquid resistance possess low surface free energy after modification with B-ala/AIBN = 5/1 PBZ.

3.1 Introduction

Low surface energy polymeric materials with good film-forming characteristics have attracted great interest because of their practical applications. [1] Consequently great attention has been placed on precise strategies modifying these solid surfaces. [2] Most of the low surface energy polymeric materials that have been developed were based on fluorine- or silicon-containing polymers. Polybenzoxazine (PBZ), a new class of low surface energy material, has recently been developed displaying a strong intramolecular hydrogen bonding but extremely low surface free energy, even lower than pure Teflon. [3] However, the requirement of high-temperature curing (ca. 180 ~ 210°C) by PBZ limits its broader applications, especially for most polymer substrates. A method of lower temperature curing for benzoxazine is thus urgently needed to broaden PBZ applications in temperature-sensitive substrates such as most polymeric materials. In this context, we discovered that Bis(3-allyl-3,4-dihydro-2*H*-1,3-benzoxazinyl)-isopropane (B-ala) can be cured at a relatively lower temperature (120 °C) with the aid of 2,2'-azobisisobutyronitrile (AIBN), resulting in even lower surface energy than that from the conventional method. Many polymer substrates such as polycarbonate, poly(4-vinyl pyridine), poly(4-vinyl phenol) and the like others can be coated by the modified polybenzoxazine in order to possess low surface energy.

3.2 Experiment Section

3.2.1 Materials

All the chemicals were used as received. Bisphenol A, paraformaldehyde (95%) and AIBN were supplied by the Showa Chemical Company of Japan. 2,2'-Bis(3-methyl-3,4-dihydro-2H-1,3-benzoxazinyl)propane (BA-m) was supplied by Shikoku Corporation. Finally, poly(4-vinylpyridine) ($M_w = 60,000$) was obtained from Aldrich of USA. The synthesis of B-ala was based on the reaction of bisphenol A with allylamine and paraformaldehyde according to the previously reported procedure. [4] Likewise poly(4-vinyl phenol) ($M_w = 10,000$; PDI = 1.4) was synthesized according to the previously reported method. [5]

3.2.2 Contact Angle Measurement

The surface free energy of the polymer sample was determined by contact angle goniometry at 25 °C using a Krüss GH-100 goniometer interfaced with image-capture software by injecting a 5 μL liquid drop. Deionized water, ethylene glycol ($\geq 99\%$; Aldrich), and diiodomethane (99%; Aldrich) were used as standards for measuring the surface free energies.

3.2.3 Thin-Film Formation and Polymerization

One-half grams of the B-ala monomer was pre-mixed with a certain mole ratio of AIBN in 10 mL tetrahydrofuran (THF) at room temperature. The solution was then filtered through a 0.2 μm syringe filter before spin coating onto a glass slide ($100 \times 100 \times 1 \text{ mm}^3$).

3.2.4 Polymer Thin Film Formation

Polymer solution was prepared by dissolving the polymer in ethanol at a concentration of 10 wt%. One mL of the appropriate polymer solution was spin-coated onto a glass slide using a photoresistant spinner operating at 1500 rpm for 45 s. The sample was then left to dry at 60 °C for 1 h to remove residual solvent. The 0.5 g B-ala monomer was pre-mixed with AIBN to produce a mole ratio of 5 in toluene(10ml) B-ala/AIBN at room temperature. Finally, the mixed solution was filtered through a 0.2 μm syringe filter before spin-coating onto the polymer thin film surface.



3.3 Results and Discussion

The ^1H NMR spectrum of B-ala as shown in Figure 3-1 established that the structure of B-ala was recorded in deuterated chloroform (CDCl_3) solution at 25°C by using a Varian UNITY INOVA-400 NMR spectrometer. The two multiplets at 5.25 and 5.95 ppm were typical for the protons of $=\text{CH}_2$ and $=\text{CH}-$ in the allyl group, respectively. The protons of $-\text{CH}_2-$ of the allyl group showed a doublet at 3.36 ppm. The characteristic protons of oxazine ring appeared at 3.92 and 4.82 ppm as assigned to $-\text{Ar}-\text{CH}_2-\text{N}-$ and $-\text{OCH}_2-\text{N}-$, respectively, while the aromatic protons appeared as a multiplet at 6.77-7.0 ppm. Besides, ^{13}C NMR spectrum and Mass spectrum of B-ala are shown in Figure 3-2 and 3-3 to provide evidences for the synthesis of B-ala monomer is successful.

The B-ala monomer contained the *N*-allyl group that can polymerize through free radical polymerization with the aid of a free radical initiator. The AIBN is known as an effective free radical initiator for addition polymerization of the *N*-allyl group [4, 6]. Figure 3-4 shows the DSC thermograms of the bifunctional allyl-containing benzoxazine monomer B-ala, with and without AIBN as an initiator. Two exothermic peaks were observed for B-ala, which correspond to the crosslinking of the *N*-allyl group (260°C) and the ring-opening polymerization (210°C) of the benzoxazine (Figure 3-5). [4] Another exothermic peak appeared at 120°C when AIBN was added, which can be attributed to the breaking of its azo group. As shown in Figures 3-6 (a) and 3-6 (b), the characteristic absorption band assigned to the allyl group appeared at 1644 cm^{-1} (stretching of $\text{C}=\text{C}$). The intensity of this allyl peak (1644 cm^{-1}) decreased in the presence of AIBN and with the increase of curing time (Figure 3-6 (b)), implying that the polymerization of *N*-allyl groups took place by the free radical mechanism. However, the tetrasubstituted benzene mode at 1484 cm^{-1} , corresponding

to benzoxazine polymerization via ring opening, was somewhat unexpected to have increased when the AIBN was added (Figure 3-6 (c)). Ishida et al. [7] studied the curing behavior of benzoxazine monomer and found that the benzoxazine precursor undergoes an autocatalytic type of curing mechanism as catalyzed by the phenol group formed by the ring opening of the oxazine ring. Based on a previous report, [8] the decomposition heat from the breaking of the azo group as observed for AIBN at 363° K was around 123 J/g. Furthermore, certain phenolic-containing oligomers were formed due to the heat release from the breaking of the azo group of the AIBN. The phenol group of these oligomers provided catalytic effect for the ring opening of the oxazine ring in the subsequent curing. More oligomers formed during the earlier stages of the curing process resulting in the higher rate of ring-opening crosslinking of the oxazine ring. More AIBN was added to form more oligomers, thereby releasing more heat from the breaking of more azo groups and resulting in a higher rate of ring-opening crosslinking of the oxazine ring (Figure 3-6 (d)). As a result, the radical initiator AIBN, not only initiated the free radical polymerization for the allyl group but also catalyzed the ring-opening reaction of benzoxazine.

Table 3-1 lists the surface roughness and the advancing contact angles of the three test liquids and the respective surface free energies (γ_s) of B-ala and B-ala/AIBN PBZs with various curing times. The lowest surface free energy obtained was 15.3 mJ/m² from the B-ala/AIBN=5:1 PBZ system after 24 h of curing at 120 °C. In both B-ala and B-ala/AIBN PBZ systems at the curing temperature of 120 °C, the advancing contact angles of all the three test liquids (water, ethyleneglycol and diiodomethane) increased as curing time was increased. At the same curing time, all the advancing contact angles from B-ala/AIBN PBZ films were relatively higher than those from B-ala PBZ films, especially in the diiodomethane liquid system. The

surface free energy, γ_s , was calculated by using van Oss and Good's three-liquid method [9] and two-liquid geometric method. [10] The extremely low surface free energy ($\gamma_s = 15.3 \text{ mJ/m}^2$) from the B-ala/AIBN=5:1 after 24 h of curing was even lower than that of pure Teflon ($\gamma_s = 16.43 \text{ mJ/m}^2$). [3] This phenomenon can be explained in terms of the more intramolecular hydrogen bonding formed. To determine the extent of hydrogen bonding within B-ala and B-ala/AIBN PBZs, FTIR curve-resolving on all hydrogen bondings were performed. Figure 3-7 displays the FTIR spectra of the B-ala/AIBN PBZ thin films as a function of curing time (2, 4, 8, and 24 h) at 120 °C. The FTIR spectrum of the pure B-ala system is similar to the B-ala/AIBN system. The fraction of the peak at 3207 cm^{-1} , corresponding to the OH \cdots N intramolecular hydrogen bond, increased when the curing time increased, while the OH \cdots O intermolecular hydrogen bond at 3417 cm^{-1} slightly decreased when the curing time increased. When AIBN was added, the rate of the ring-opening reaction and the fraction of the intramolecular hydrogen bonding both increased (Table 3-2). The surface free energies versus the curing times at 120 °C of various molar ratios for B-ala monomer to AIBN are shown in Figure 3-8. The lowest surface free energy for the B-ala/AIBN=5:1 PBZ system was 15.3 mJ/m^2 which was even lower than the BA-m PBZ system cured in 1h at 210° C (16.4 mJ/m^2). [3]

The thermal curing process of this B-ala/AIBN PBZ system is at 120 °C, therefore, it can be used to modify many polymer substrates. Figure 3-9 shows the advancing contact angles of water, ethylene glycol, and diiodomethane on the poly(4-vinyl pyridine) thin film before and after modification with B-ala/AIBN = 5/1 PBZ, those advancing contact angles of three test liquids all increase substantially. Poly(4-vinyl phenol) film and polycarbonate substrates give the same trend as shown in Table 3-3.

3.4 Conclusions

The free radical initiator AIBN, induced polymerization of the *N*-allyl group and produced phenol-containing oligomers. These oligomers were able to catalyze the ring opening of the oxazine ring at a relatively lower curing temperature (120 °C) to produce polybenzoxazine with stronger intramolecular hydrogen bonding but lower surface energy. B-ala and B-ala/AIBN PBZ thin films both possessed low surface free energy because the strong intramolecular hydrogen bonds were formed during the curing process. B-ala/AIBN PBZ system had a relatively lower surface free energy than the pure B-ala system because of the higher extent of the ring-opening of oxazine. Moreover, it can modify many polymer substrates that are thermally stable at or above 120 °C.



References

- [1] (a) Li, H.; Wang, X.; Song, Y.; Liu, Y.; Li, Q.; Jiang, L.; Zhu, D. *Angew. Chem.* **2001**, 113, 1793. (b) Sun, T.; Wang, G.; Liu, H.; Feng, L.; Jiang, L.; Zhu, D. *J. Am. Chem. Soc.* **2003**, 125, 14996 (c) Russell, T. P. *Science* **2002**, 297,964 (d) Aussillous, P.; Qumrm, D. *Nature* **2001**, 411, 924.
- [2] (a) Ryu, D. Y.; Shin, K.; Drockenmuller, E.; Hawker, C. J.; Russell, T. P. *Science* **2005**, 308, 236 (b) Mansky, P.; Liu, Y.; Huang, E.; Russell, T. P.; Hawker, C. *Science* **1997**, 275 ,1458
- [3] (a) Wang, C. F.; Su, Y. C.; Kuo, S. W.; Huang, C. F.; Sheen, Y. C.; Chang, F. C. *Angew. Chem. Int. Ed.* **2006**, 45, 2248 (b) Wang, C. F.; Wang, Y. T.; Tung, P. H.; Kuo, S. W.; Lin, C. H.; Sheen, Y. C.; Chang, F. C. *Langmuir* **2006**, 22, 8289 (c) Wang, C. F.; Chiou, S. F.; Ko, F. H.; Chou, C. T.; Lin, H. C.; Huang, C. F.; Chang, F. C. *Macromol. Rapid Commun.* **2006**, 27, 333.
- [4] Agag, T.; Takeichi, T. *Macromolecules*, **2003**, 36, 6010.
- [5] Tung, P. H.; Kuo, S. W.; Jeong, K. U.; Cheng, S. Z. D.; Huang, C. F.; Chang, F. C. *Macromol. Rapid Commun.* **2007**, 28, 271.
- [6] Ishida, H.; Ohba, S. *Polymer*, 46, **2005**, 5588.
- [7] (a) Ishida, H.; Rodriguez, Y. *Polymer* **1995**, 36, 3151. (b) Dunkers, J.; Ishida, H. *J. Polymer Science: Part A: Polymer Chemistry* **1999**, 37, 1913.
- [8] Severini, F.; Gallo, R. *J. Thermal Analysis*, **1984**, 29, 561.
- [9] (a) van Oss, C. J.; Ju, L.; Chaudhury, M. K.; Good, R. J. *J. Colloid Interface Sci.* **1989**, 128, 313. (b) van Oss, C. J.; Chaudhury, M. K.; Good, R. J. *Chem. Rev.* **1988**, 88, 927.
- [10] Fowkes, F. W. "Dispersion Force Contributions to Surface and Interfacial Tensions" Gould, R. F., Ed.; American Chemical Society: Washington, DC, **1964**.

Table 3-1. Advancing contact angles for water, ethylene glycol (EG), and diiodomethane (DIM) and their corresponding surface free energy of B-ala and B-ala/AIBN polybenzoxazine films.

	Curing time (h)	Roughness (nm)	Contact angle(°)			Surface free energy (mJ/m ²)		
			Water	DIM	E.G.	γ_s (HD)	γ_s (ED)	γ_s
B-ala								
	0.5	1.3	83.7	18.4	66.5	48.3	49.3	48.2
	1	1.2	85.3	19.2	69.6	48.2	48.5	48.0
	2	0.8	91.5	21.1	73.5	48.6	47.5	47.5
	4	1.4	105.0	51.4	79.5	35.4	34.4	33.5
	8	1.3	107.5	58.1	86.5	31.3	30.0	29.7
	24	1.2	111.9	63.3	88.9	28.7	27.1	26.7
B-ala/AIBN = 5/1								
	0.5	1.4	93.1	20.7	70.5	49.2	48.0	47.6
	1	1.0	95.0	21.0	72.0	49.6	47.7	47.5
	2	1.0	103.0	24.7	75.4	51.1	46.3	46.3
	4	0.8	107.2	63.2	80.4	27.7	29.4	26.8
	8	0.8	109.0	83.0	87.0	16.0	21.2	16.6
	24	1	112.0	85.3	89.0	14.9	19.8	15.3

* Curing temperature = 120 °C

* Molar ratio of B-ala monomer/AIBN = 5/1

* γ_s (HD) : Test liquids are deionized water and diiodomethane

* γ_s (ED) : Test liquids are ethyleneglycol and diiodomethane

Table 3-2. Fraction of hydrogen bonding of B-ala/AIBN=5:1 PBZ film cured at 120 °C for 2, 4, 8, and 24 h.

	O ⁻ ---H ⁺ N Intramolecular hydrogen bonding (%)	OH---N Intramolecular hydrogen bonding (%)	OH---O Intermolecular hydrogen bonding (%)
B-ala-AIBN-5-1-2h	63.64	31.66	4.69
B-ala-AIBN-5-1-4h	59.84	36.06	4.10
B-ala-AIBN-5-1-8h	56.86	39.52	3.62
B-ala-AIBN-5-1-24h	56.65	40.65	2.70



Table 3-3. The advancing contact angle for water, ethylene glycol, and diiodomethane of poly(4-vinyl phenol), poly(4-vinyl pyridine) and polycarbonate substrates before and after modification with B-ala/AIBN=5/1 PBZ thin film cured 8 h at 120 °C.

Polymer substrates	Contact angle(°)			Surface energy γ_s (mJ/m ²)
	Water	DIM	E.G.	
<i>Before modification</i>				
Poly(4-vinyl phenol)	72.1	44.4	45.6	40.5
Poly(4-vinyl pyridine)	62.2	0	48.0	57.4
Polycarbonate	89.5	35.0	56.0	42.3
<i>After modification</i>				
Poly(4-vinyl phenol)	107.0	80.6	87.3	17.6
Poly(4-vinyl pyridine)	108.7	83.2	86.3	16.6
Polycarbonate	107.3	80.3	86.2	17.9



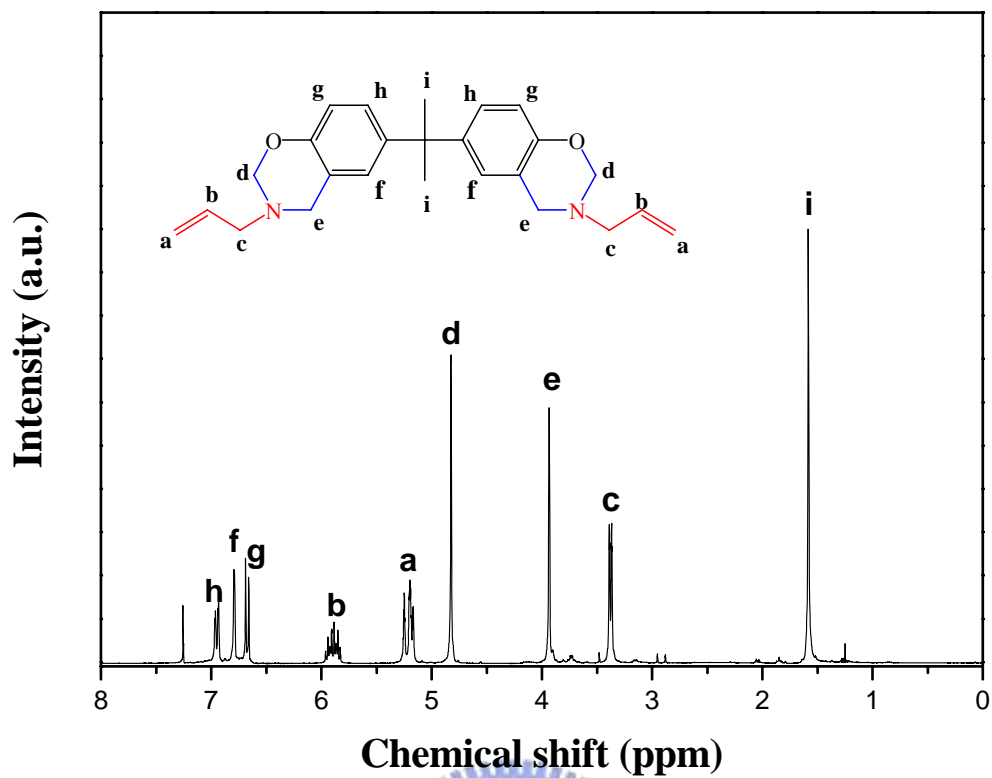


Figure 3-1. The ^1H NMR spectrum of B-ala monomer.



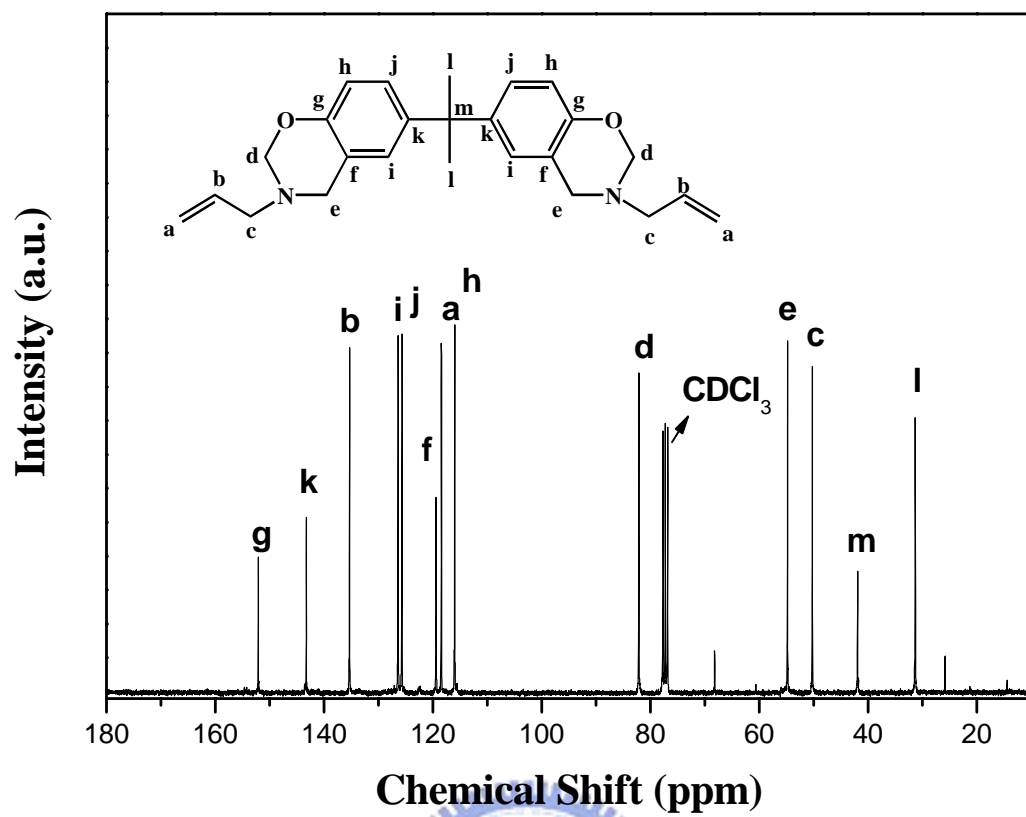


Figure 3-2. The ^{13}C NMR spectrum of B-ala monomer.



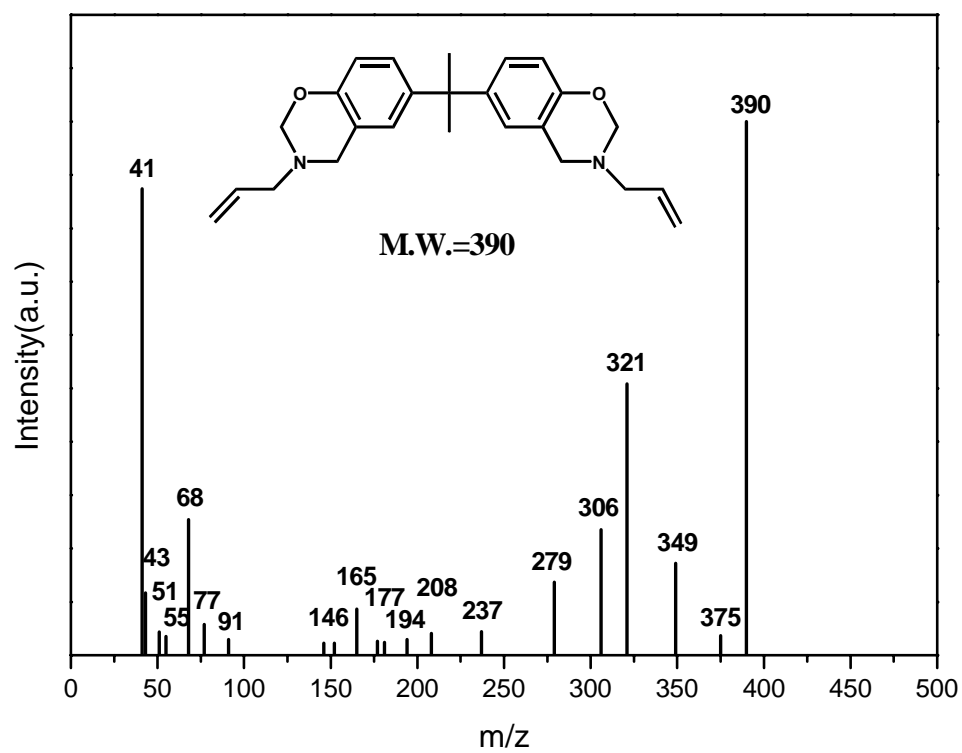


Figure 3-3. The Mass spectrum of B-ala monomer.



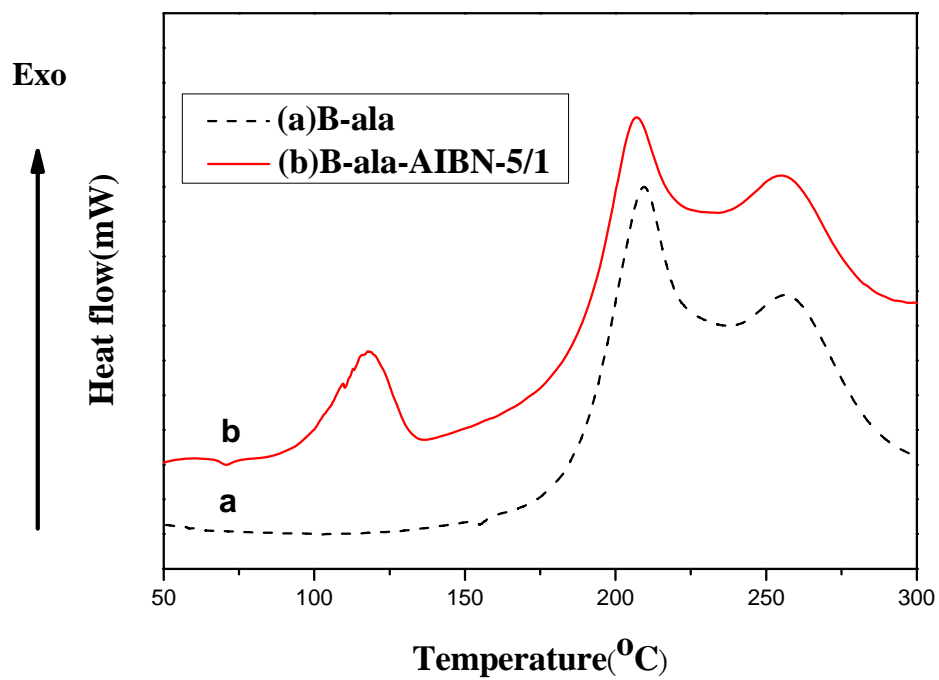


Figure 3-4. DSC diagram of B-ala and B-ala/AIBN molar ratio = 5:1.



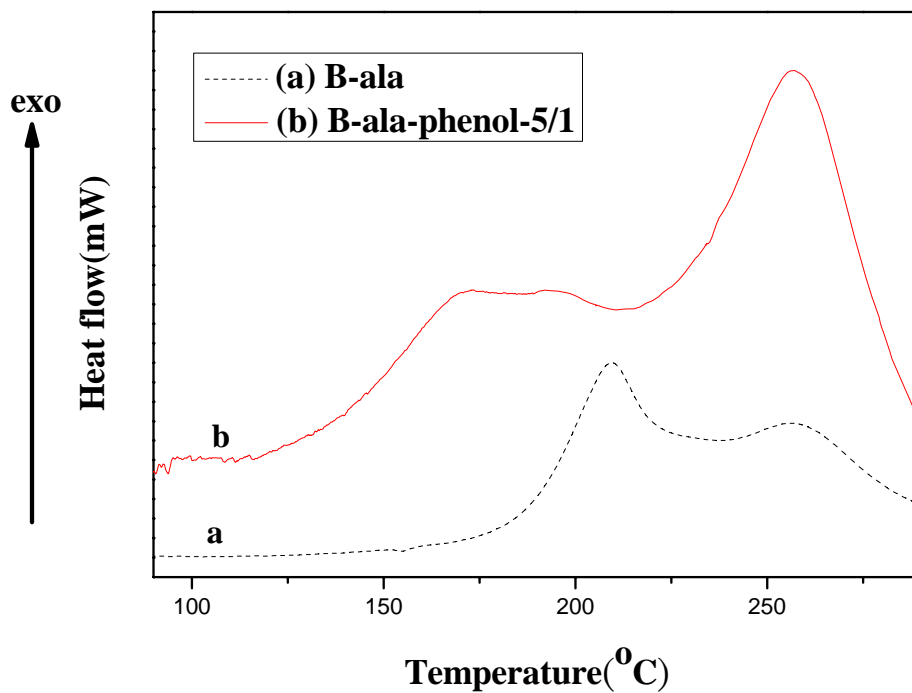


Figure 3-5. DSC diagram of B-ala and B-ala/phenol molar ratio = 5:1.



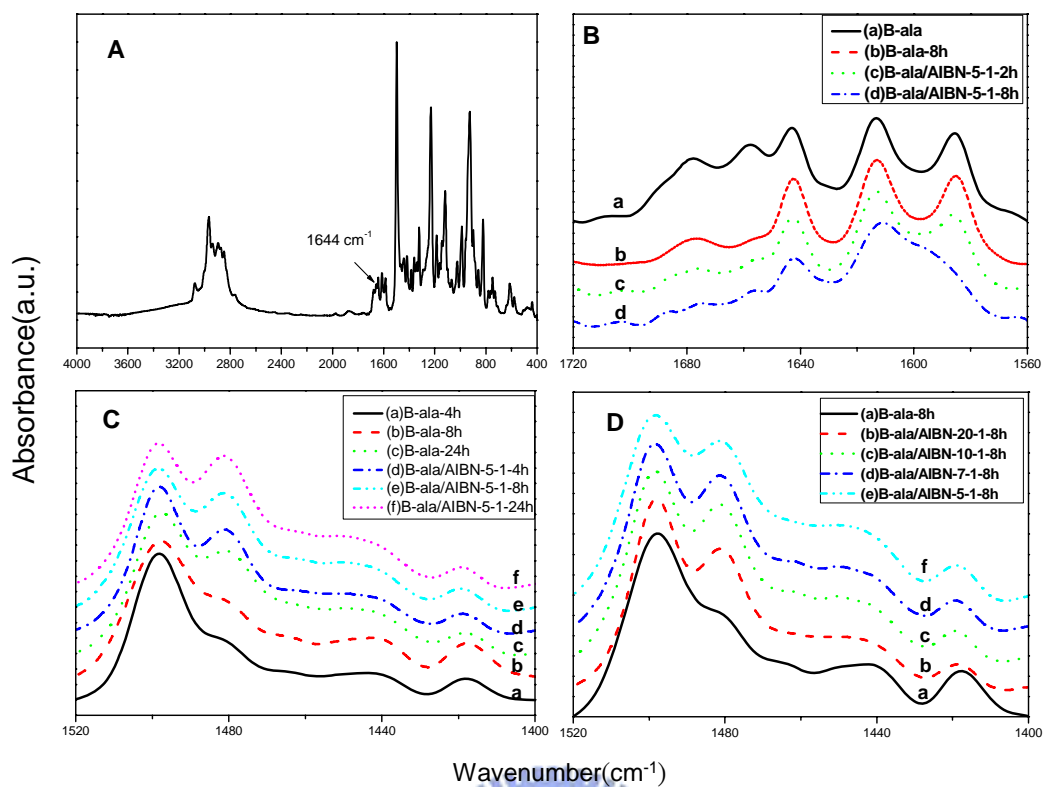


Figure 3-6. FTIR spectra of B-ala and B-ala/AIBN PBZ film. (a) B-ala, (b) B-ala and B-ala/AIBN = 5:1 cured at 120 °C, (c) B-ala and B-ala/AIBN = 5:1 cured at 120 °C, and (d) B-ala and different molar ratio of B-ala/AIBN cured for 8h at 120 °C.

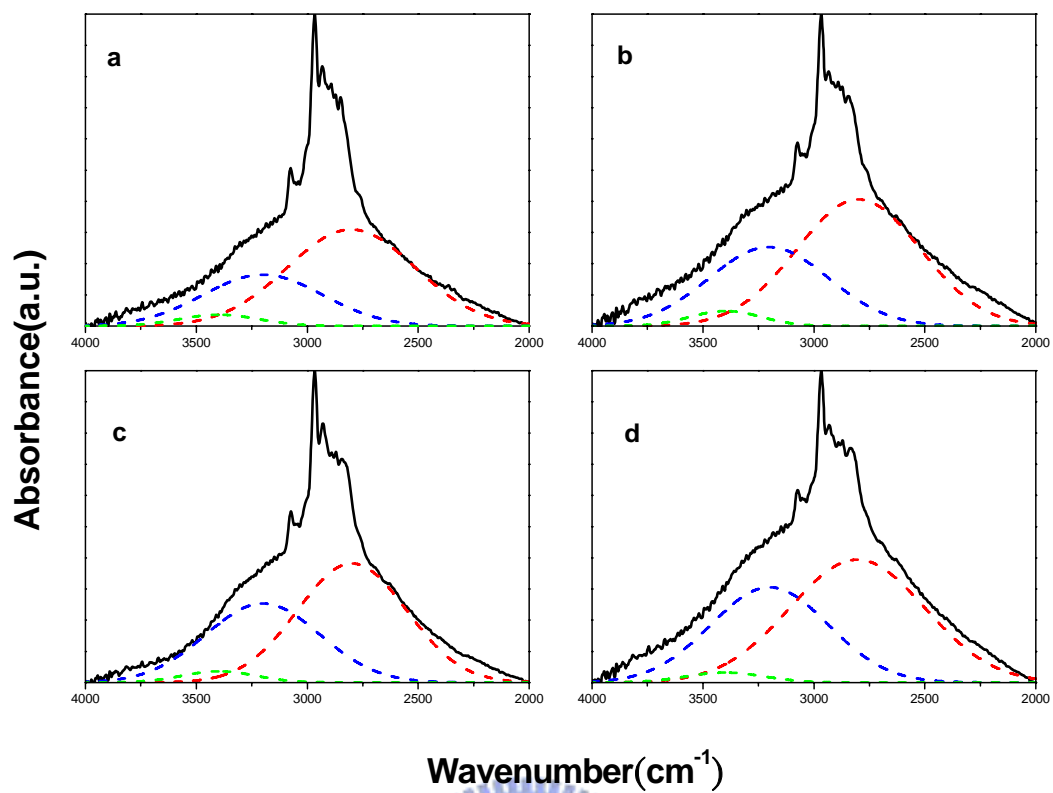


Figure 3-7. Curve fitting for the FTIR spectra of B-ala/AIBN=5:1 PBZ film cured at 120 °C for (a) 2, (b) 4, (c) 8, and (d) 24 h.

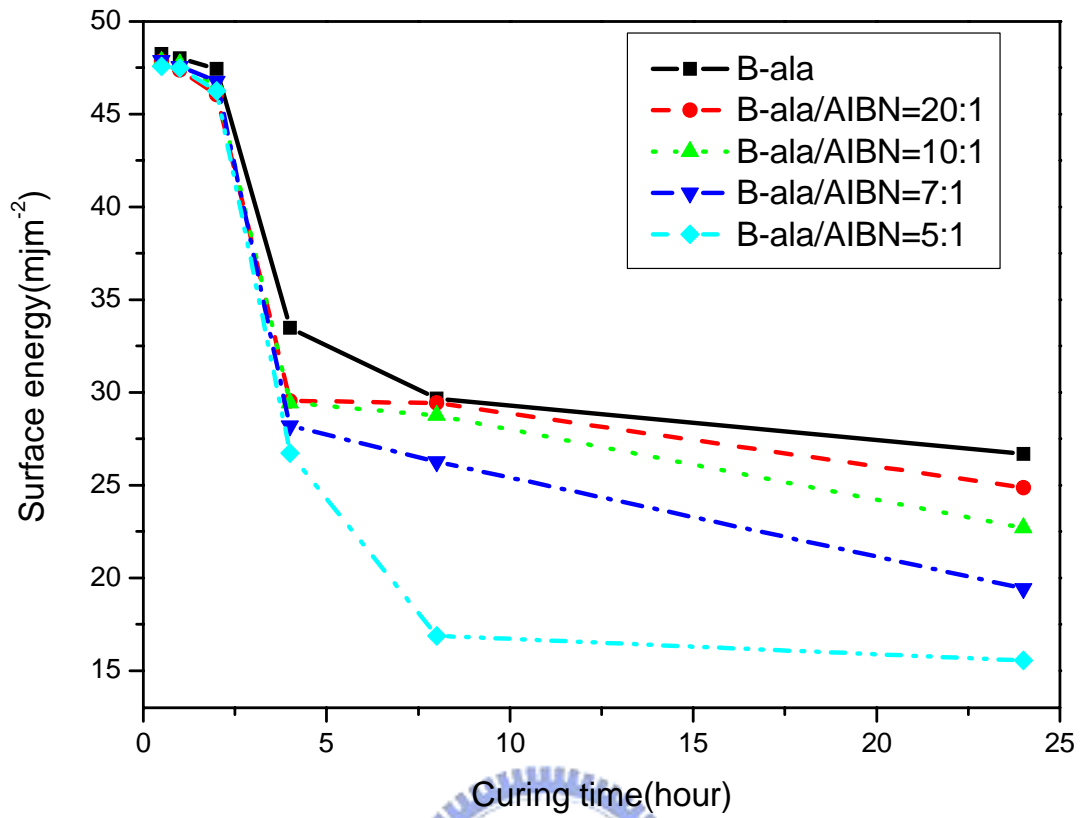


Figure 3-8. Surface free energy of B-ala and B-ala with different molar ratio of AIBN cured at 120 °C.



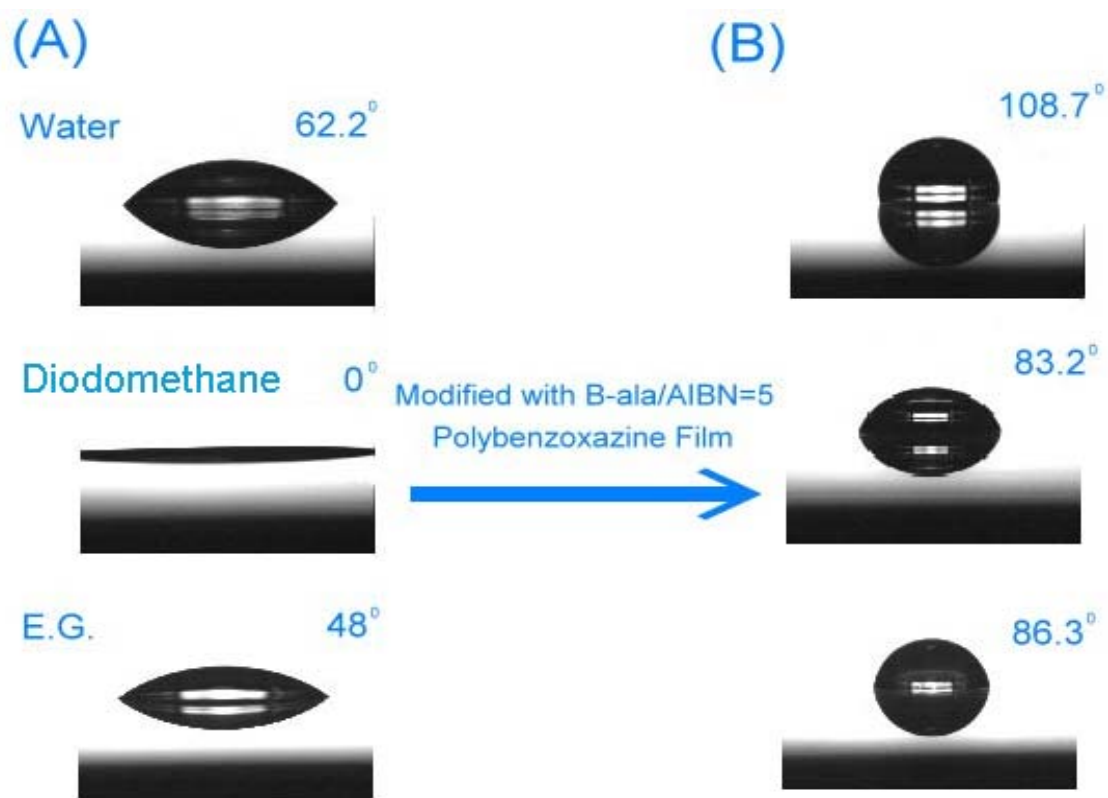


Figure 3-9. The advancing contact angle for water, ethylene glycol, and diiodomethane of (a)poly(4-vinyl pyridine) thin film (b)modified with B-ala/AIBN=5 PBZ thin film.

Chapter 4

Tuning the Surface Free Energy of Polybenzoxazine Thin Films

Abstract

A novel approach to manipulate the surface free energy and wettability on polybenzoxazine thin films can be achieved simply by varying time of thermal treatment or UV exposure. Fraction of the intramolecular hydrogen bonding of the as cured sample will convert into intermolecular hydrogen bonding upon thermal treatment or UV exposure and thus results in increase of hydrophilicity and wettability. This UV approach provides a simple method to generate wettability patterns or wettability gradients on the surface of polybenzoxazine film. In addition, we have applied this technique to the preparation of a large-area periodic array of CdTe colloidal nanocrystals on polybenzoxazine thin films.

4.1 Introduction

The surface and interfacial properties of materials are directly related to their surface energies. Current approaches toward engineer tunable surfaces include light irradiation [1,2] and UV [3] thermal treatment, [4, 5] acidification, [6-8] and applying electrical potentials, [9,10] among others. [11] Intra- and intermolecular interactions play important roles in determining the surface properties of polymers. For example, Jiang et al. [4] found that at temperatures above its lower critical solution temperature (LCST), the compact, collapsed conformation of poly(N-isopropylacrylamide) (PNIPAAm), induced by intramolecular hydrogen bonding between the C=O and N-H groups of the main chains results in a low surface free energy and a high contact angle for water. When the temperature is below the LCST, however, intermolecular hydrogen bonding between the PNIPAAm main chains and water molecules predominates leading to a higher surface free energy and a lower water contact angle. Similarly, Chung et al. [12] reported that the presence of amide groups in a fluorinated-main-chain liquid-crystalline polymer system induces strong intermolecular hydrogen bonding resulting in higher surface free energies and higher degrees of hydrophilicity.

Structured surfaces that exhibit lateral patterns of varying wettability have received extensive attention because it can apply as preparing fluid microchips [13] and the periodical arrangements of metallic nanoparticles [14,15] or nanowires [16] and self-assembly of block copolymer [17] or carbon nanotubes [18]. Besides, a gradient surface displays a gradual change in the chemical and physical properties along its length. has a wide range of applications in material science. [19-22] A gradient in a surface can induce the net mass transport of liquids, which affords a driving force for operation of microfluidic devices and for biological cell motility in

vitro. Therefore, a simple method to create wettability pattern or wettability gradient on a polymer thin film was needed to be developed.

Polybenzoxazines (PBZs), feature strong intramolecular hydrogen bonds that result in extremely low surface free energies, even lower than that of pure Teflon. [23] In PBZ systems, strong intramolecular hydrogen bonding between the hydroxyl groups and the amino groups in the Mannich bridges tends to decrease the surface free energy, whereas intermolecular hydrogen bonding between hydroxyl groups results in higher surface free energies. We are unaware, however, of any previously available methods that allow precise control over the surface free energies of PBZ films. In this paper, we present a simple strategy for obtaining wettability patterns and wettability gradients on PBZ thin films by using UV irradiation to modify the extent of intra- and intermolecular hydrogen bonding. We have applied this technique to the preparation of a large-area periodic array of CdTe colloidal nanocrystals on PBZ thin films.



4.2 Experiment Section

4.2.1 Materials

All chemicals were used as received. Bisphenol A and paraformaldehyde (95%) were supplied by the Showa Chemical Company (Japan). The synthesis of bis(3-allyl-3,4-dihydro-2*H*-1,3- benzoxazinyl)isopropane (B-ala) was based on the reaction of bisphenol A, allylamine, and paraformaldehyde (Scheme 4-1). Column chromatography (eluent: ethyl acetate/hexane, 2:1) was used to separate the impurities, which were identified as unreacted phenols, amines, and benzoxazine oligomers.

4.2.2 Contact Angle Measurement

The surface free energy of the polymer sample was determined through contact angle goniometry of a liquid drop (5 μL) at 25 °C using a Krüss GH-100 goniometer interfaced with image-capture software. Deionized water, ethylene glycol ($\geq 99\%$; Aldrich), and diiodomethane (99%; Aldrich) were used as standards for measuring the surface free energies.

4.2.3 Fourier Transform Infrared (FTIR) Spectroscopy

All infrared spectra were recorded using a Nicolet Avatar 320 FTIR spectrophotometer; 32 scans were collected at a spectral resolution of 1 cm^{-1} . FTIR spectra of the polymer films were determined using the conventional potassium bromide (KBr) plate method. Each sample was prepared by casting a THF solution directly onto a KBr plate and then curing under conditions similar to those used for the bulk preparation. All films were sufficiently thin to exist within the absorbance range in which the Beer–Lambert law is obeyed.

4.2.4 Ultraviolet Irradiation Exposure

Five 6W, low-pressure mercury lamps ($\lambda = 265$ nm) were used as the UV irradiation source. Samples were placed at a distance of 25 cm from the source to receive 30 W/m^2 of radiation.

4.2.5 Electron Spectroscopy for Chemical Analysis (ESCA)

The chemical composition of the substrate surface was analyzed using a Thermo VG Scientific ESCALAB 250 spectrometer equipped with a monochromatic Al $K\alpha$ X-ray source (1486.6 eV photons); the vacuum within the analysis chamber was maintained at or below ca. 10^{-8} mbar.

4.2.6 Thin-Film Formation and Polymerization

A solution of the B-ala monomer (0.5 g) in THF (10 mL) was filtered through a $0.2\text{-}\mu\text{m}$ syringe filter before spin-coating onto a glass slide ($100 \times 100 \times 1 \text{ mm}^3$) and the sample was then cured in an oven at 210°C .

4.2.7 Periodic Arrangement of Arrays of CdTe Colloidal Nanocrystals

Aqueous colloidal CdTe solutions were prepared by adding a freshly prepared NaHTe solution to 1.25×10^{-3} N N_2 -saturated CdCl_2 solutions at pH 9.0 in the presence of mercaptocarboxylic acid (stabilizing agent). The molar ratio of Cd^{2+} , stabilizer, and HTe^- was fixed at 1:2.4:0.5. The resulting mixture was then heated under reflux to control the growth of the CdTe nanocrystals. The B-ala polybenzoxazine (PBZ) thin films were exposed through a mask to 265-nm UV radiation at a distance of 1 cm for ca. 20 min to produce a hydrophilic pattern. The periodic arrays of CdTe colloidal nanocrystals were prepared through direct

evaporation of a drop of an aqueous colloidal CdTe solution on PBZ thin films exhibiting patterned lyophobicity. Fluorescent images were acquired with a Leica DMI 6000B CS laser scanning confocal microscope equipped with diode, argon blue, green DPSS, and helium-neon lasers for excitation.



4.3 Results and discussion

After optimizing its thermal curing conditions, B-ala PBZ contains predominantly intramolecular hydrogen bonds and, therefore, possesses an extremely low surface free energy. Figure 4-1 displays the advancing contact angles and surface free energies (γ_s) of three test liquids on B-ala PBZ films after various curing times at 210 °C. From Table 4-1, the lowest surface free energy we obtained for a B-ala film was 14.4 mJ m⁻², calculated using van Oss and Good's three-liquid method, [24] which is substantially lower than that of pure Teflon (21 mJ m⁻²). The surface free energy in this B-ala PBZ system decreased initially and then increased steadily upon increasing the curing time. This phenomenon can be explained in terms of changes in the ratio of intra- and intermolecular hydrogen bonds (Figure 4-2). [23] Therefore, the surface free energy of this PBZ is tunable—from 14.4 to 46.3 mJ m⁻²—merely by controlling the length of time that it is subjected to thermal curing. Nevertheless, this technique would be very difficult to use to fabricate a gradient in the surface free energy or provide a wettability pattern on PBZ.

Ishida et al. [25, 26] determined that C=O-containing species are formed when a bisphenol-A-based PBZ resin is exposed to UV radiation under ambient conditions. The isopropylidene linkages of PBZ are the reactive sites where oxidation and cleavage occur upon UV exposure, forming 2, 6-disubstituted benzoquinone units. The presence of these benzoquinone moieties decreases the extent of intramolecular hydrogen bonding while increasing the extent of intermolecular hydrogen bonding. Because radical formation and oxidation reactions induced by UV radiation are usually concentrated at polymer surfaces, we suspected that the surface properties of PBZ thin films would be greatly affected by their length of UV exposure and the corresponding photo-oxidation mechanism is shown in Scheme 4-2.

Figure 4-1 reveals that the advancing contact angles of the three test liquids decreased upon increasing the UV exposure time of B-ala PBZ films (cured 2 h at 210 °C). This behavior is consistent with a partial destruction of intramolecular hydrogen bonding and a corresponding increase in the extent of intermolecular hydrogen bonding after UV exposure, resulting in higher surface free energies and higher degrees of hydrophilicity. From Table 4-2, we find that the advancing contact angles of the polar test liquids (water, ethylene glycol) decrease substantially after UV exposure; the decrease in the advancing contact angle of the nonpolar liquid (diiodomethane) is less pronounced. To determine the interactions occurring between these liquids and the PBZ thin film, we used the two-liquid geometric method [27] to determine the corresponding values of γ_s , γ^d , and γ^p (Table 4-3). The values of γ^d and γ^p can be calculated from the measured contact angles; the superscript “d” refers to the London dispersion forces, whereas the superscript “p” refers to polar forces, including all of the interactions established between the solid and liquid, such as Keesom dipole–dipole, Debye dipole-induced dipole, and hydrogen bonding interactions. The value of γ^p increased rapidly upon increasing the UV exposure time, but the change in γ^d was relatively insignificant; these phenomena imply that the polar forces between the PBZ thin film and the testing liquids increased substantially after UV exposure. The presence of new polar quinone C=O functional groups on the irradiated surface led to stronger polar forces between the PBZ film and the testing liquid, resulting in lower advancing contact angles for both water and ethylene glycol. The ESCA results in Table 4-3 reveal that the atomic fraction of oxygen, an indication of the degree of photo-oxidation of the surface, increased dramatically after UV exposure.

The relationship between the surface free energy of B-ala PBZ thin films and the UV exposure time suggested that we could manipulate the surface free energy at selected regions merely by varying the UV exposure time to create wettability patterns or wettability gradients. Scheme 4-3 provides an illustration of the procedures used to control the surface free energy of PBZ thin films. In the procedure, we controlled the surface free energy of the B-ala PBZ thin films through thermal curing and then created hydrophilic regions on them through UV exposure. Figures 4-3 (a) and 4-3 (b) present photographic images of a wettability pattern and a wettability gradient formed upon two PBZ films after UV exposure. Furthermore, we also deposited CdTe colloidal nanocrystals through direct evaporation of a nanocrystal solution [28] in periodic arrangements on PBZ thin films exhibiting patterned lyophobicity (Figure 4-4).



4.4 Conclusion

In conclusion, the surface free energy and hydrophilicity of PBZ films can be controlled through a combination of thermal treatment and UV exposure to change the ratios of intra- to intermolecular hydrogen bonds. This simple method allows wettability patterns and wettability gradients to be produced on the surfaces of PBZ films; in addition, we used this technique to pattern periodic arrangements of CdTe colloidal nanocrystals on PBZ thin films.



References

- [1] Rosario, R.; Gust, D.; Hayes, M.; Jahnke, F.; Springer, J.; Garcia, A. A. *Langmuir* 2002, 18, 8062-8069
- [2] Feng, X.; Feng, L.; Jin, M.; Zhai, J.; Jiang, L.; Zhu, D. B. *J. Am. Chem. Soc.* 2004, 126, 62-63.
- [3] Lahann, J.; Mitragotri, S.; Tran, T.; Kaido, H.; Sundaram, J.; Choi, I. S.; Hoffer, S.; Somorjai, G. A.; Langer, R. *Science* 2003, 299, 371-374.
- [4] Sun, T.; Wang, G.; Feng, L.; Liu, B.; Ma, Y.; Jiang, L.; Zhu, D. *Angew. Chem. Int. Ed.* 2004, 43, 357-360.
- [5] Fu, Q.; Rama Rao, G. V.; Basame, S. B.; Keller, D. J.; Artyushkova, K.; Fulghum, J. E.; López, G. P. *J. Am. Chem. Soc.* 2004, 126, 8904-8905.
- [6] Ionov, L.; Houbenov, N.; Sidorenko, A.; Stamm, M.; Luzinov, I.; Minko, S. *Langmuir* 2004, 20, 9916-9919.
- [7] Yu, X.; Wang, Z.; Jiang, Y.; Shi, F.; Zhang, X. *Adv. Mater.* 2005, 17, 1289-1293
- [8] Choi, Se-Jin; Suh, K. Y.; Lee, H. H. *J. Am. Chem. Soc.* 2008, 130, 6312-6313.
- [9] Minko, S.; Müller, M.; Motornov, M.; Nitschke, M.; Grundke, K.; Stamm, M. *J. Am. Chem. Soc.* 2003, 125, 3896-3900.
- [10] Krupenkin, T. N.; Taylor, J. A.; Schneider, T. M.; Yang, S. *Langmuir* 2004, 20, 3824-3827.
- [11] Ryu, D. Y.; Shin, K.; Drockenmuller, E.; Hawker, Craig J.; Russell, T. P. *Science* 2005, 308, 236-239.
- [12] Ma, K. X.; Chung, T. S. *J. Phys. Chem. B* 2001, 105, 4145-4150
- [13] Gau, H.; Herminghaus, S.; Lenz, P.; Lipowsky, R. *Science* 1999, 283, 46-49.
- [14] (a) Linden, S.; Kuhl, J.; Giessen, H. *Phys. Rev. Lett.* 2001, 86, 4688. (b) Linden, S.; Christ, A.; Kuhl, J.; Giessen, H. *Appl. Phys. B* 2001, 73, 311.

- [15] (a)Zhang, X.; Sun, B.; Friend, R. H.; Guo, H.; Nau, D.; Giessen, H. *Nano Lett.* 2006, 6, 651 (b) Fustin, C. A.; Glasser, G.; Spiess, H.W.; Jonas, U. *Adv. Mater.* 2003, 15, 1025 (c) Fan, F.; Stebe, K. J. *Langmuir* 2004, 20, 3062
- [16] Christ, A.; Tikhodeev, S. G.; Gippius, N. A.; Kuhl, J.; Giessen, H. *Phys. Rev. Lett.* 2003, 91, 183901
- [17] (a)Peters, R. D.; Yang, X. M.; Nealey, P. F. *Macromolecules* 2002, 35, 1822 (b) Tsori, Y.; Andelman, D. J. *Chem. Phys.* 2001, 115, 1970 (c) Chandekar, A.; Sengupta, S. K.; Barry, C. M. F.; Mead, J. L.; Whitten, J. E. *Langmuir* 2006, 22, 8071
- [18] Bardecker, J. A.; Afzali, A.; Tulevski, G. S.; Graham, T.; Hannon, J. B.; Jen, A. K.-Y. *J. Am. Chem. Soc.* 2008, 130, 7226-7227.
- [19] Ito, Y.; Heydari, M.; Hashimoto, A.; Konno, T.; Hirasawa, A.; Hori, S.; Kurita, K.; Nakajima, A. *Langmuir* 2007, 23, 1845-1850.
- [20] Ichimura, K.; Oh, S.-K.; Nakagawa, M. *Science* 2000, 288, 1624.
- [21] Rosario, R.; Gust, D.; Garcia, A. A.; Hayes, M.; Taraci, J. L.; Clement, T.; Dailey, J. W.; Picraux, S. T. *J. Phys. Chem. B* 2004, 108, 12640.
- [22] (a)Daniel, S.; Chaudhury, M. J. *Langmuir* 2002, 18, 3404-3407. (b) Daniel, S.; Chaudhury, M. J.; Chen, J. C. *Science* 2003, 291, 633.
- [23] Wang, C. F.; Su, Y. C.; Kuo, S. W.; Huang, C. F.; Sheen, Y. C.; Chang, F. C. *Angew. Chem. Int. Ed.* 2006, 45, 2248.
- [24] Van Oss, C. J.; Chaudhury, M. K.; Good, R. J. *Chem. Rev.* 1988, 88, 927.
- [25] Macko, J. A.; Ishida, H.; *J. Polym. Sci. Part B: Polym. Phys.* 2000, 38, 2687.
- [26] Macko, J. A.; Ishida, H. *Polymer* 2001, 42, 6371.
- [27] Fowkes, F. W. *Dispersion Force Contributions to Surface and Interfacial Tensions*; Gould, R. F., Ed.; American Chemical Society: Washington, DC,

1964.

[28] Fan, F.; Stebe, K. J. Langmuir 2005, 21, 1149-1152



Table 4-1. Advancing contact angles for water, ethylene glycol (EG), and diiodomethane (DIM) and corresponding surface free energies of B-ala PBZ films after thermal curing

	curing time (h)	roughness (nm)	contact angle(°)			surface free energy (mJ/m ²)		
			water	DIM	E.G.	$\gamma_s(\text{HD})$	$\gamma_s(\text{ED})$	γ_s
B-ala-210°C								
	0.5	1.3	98.2	69.4	75.4	23.3	30.2	24.1
	1	1.2	112.0	83.2	84.4	15.9	22.7	16.1
	2	1.8	112.9	87.2	88.2	14.0	20.1	14.4
	4	1.4	104.6	76.7	76.8	19.2	28.4	20.1
	8	1.3	91.0	68.6	52.6	24.7	49.0	26.8
	24	1.2	19.8	48.9	10.2	68.6	75.0	46.3

* Curing temperature = 210 °C



Table 4-2. Advancing contact angles for water, ethylene glycol (EG), and diiodomethane (DIM) and corresponding surface free Energies of B-ala PBZ films cured for 2 h at 210 °C and then Subjected to UV exposure.

UV exposure time (min)	Roughness (nm)	Contact angle(°)			Surface free energy (mJ/m ²) γ_s
		Water	DIM	E.G.	
B-ala-210°C-2h					
0	1.8	112.9	87.2	88.2	14.4
10	1.6	106.0	85	81.5	16.4
20	1.4	84.6	79.6	75.9	19.9
40	1.9	65.6	74.8	60.8	26.5
60	1.4	53.4	69.1	37.8	38.4
80	1.7	34.7	64.9	25.3	43.4
100	1.7	21.3	60.8	18.3	44.8
120	1.6	6.2	54.6	3.8	46.6

* UV wavelength = 265nm

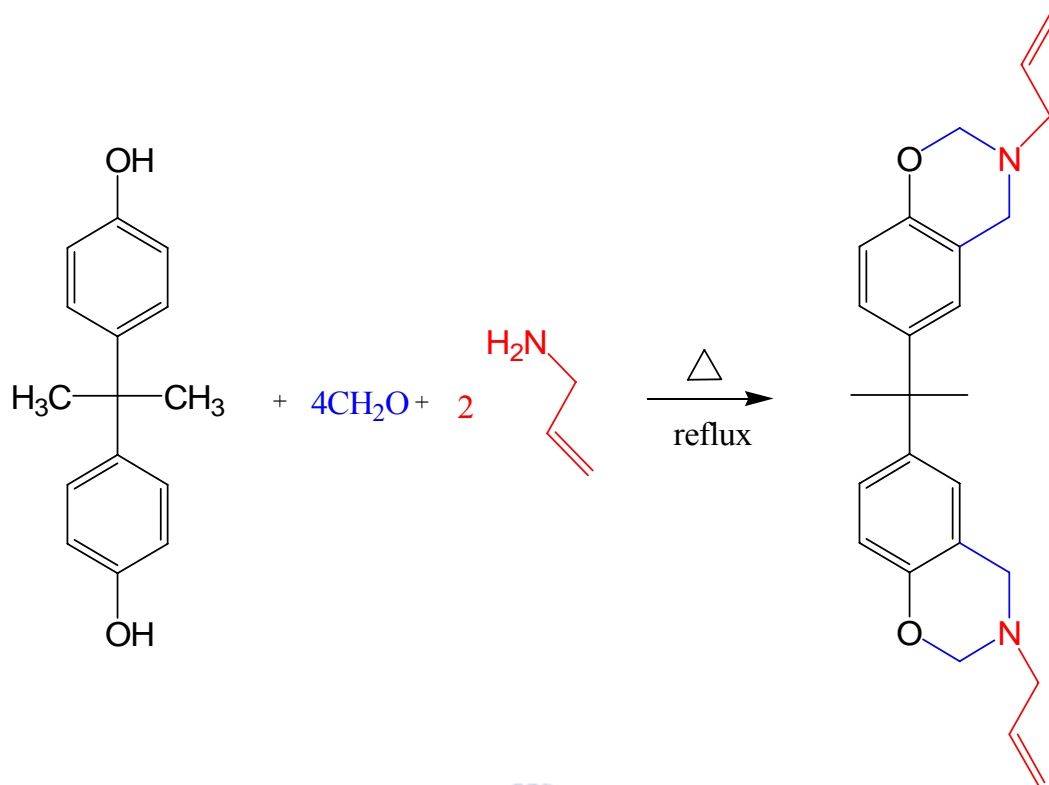
* distance between UV source and sample: 25cm



Table 4-3. Surface free energy and ESCA analysis of B-ala PBZ films cured for 2 h at 210 °C and then subjected to UV exposure

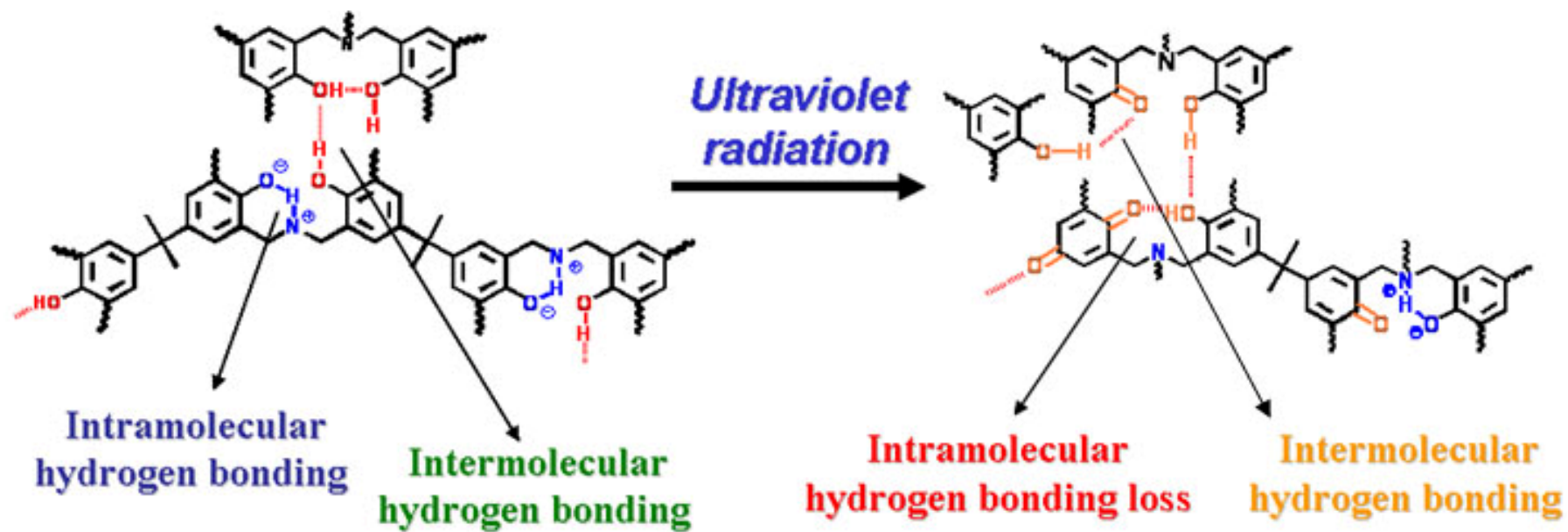
UV exposure time (min)	Surface free energy (mJ/m ²)(HD)			Surface free energy (mJ/m ²)(ED)			ESCA oxygen content (mol%)
	γ^d	γ^p	γ_s	γ^d	γ^p	γ_s	
B-ala-210°C-2h							
0	13.5	0.5	14.0	9.8	10.2	20.0	25.2
10	13.5	1.6	15.1	9.8	14.9	24.7	25.4
20	13.0	10.4	23.4	11.6	17.3	28.9	25.6
40	12.5	23.9	36.4	11.6	30.4	42.0	26.0
60	13.7	32.7	46.4	11.4	52.0	63.4	28.3
80	13.7	47.2	60.9	12.3	59.9	72.2	29.2
100	14.6	53.9	68.5	13.9	61.1	75.0	31.9
120	17.1	55.7	72.8	16.5	61.1	77.6	32.4



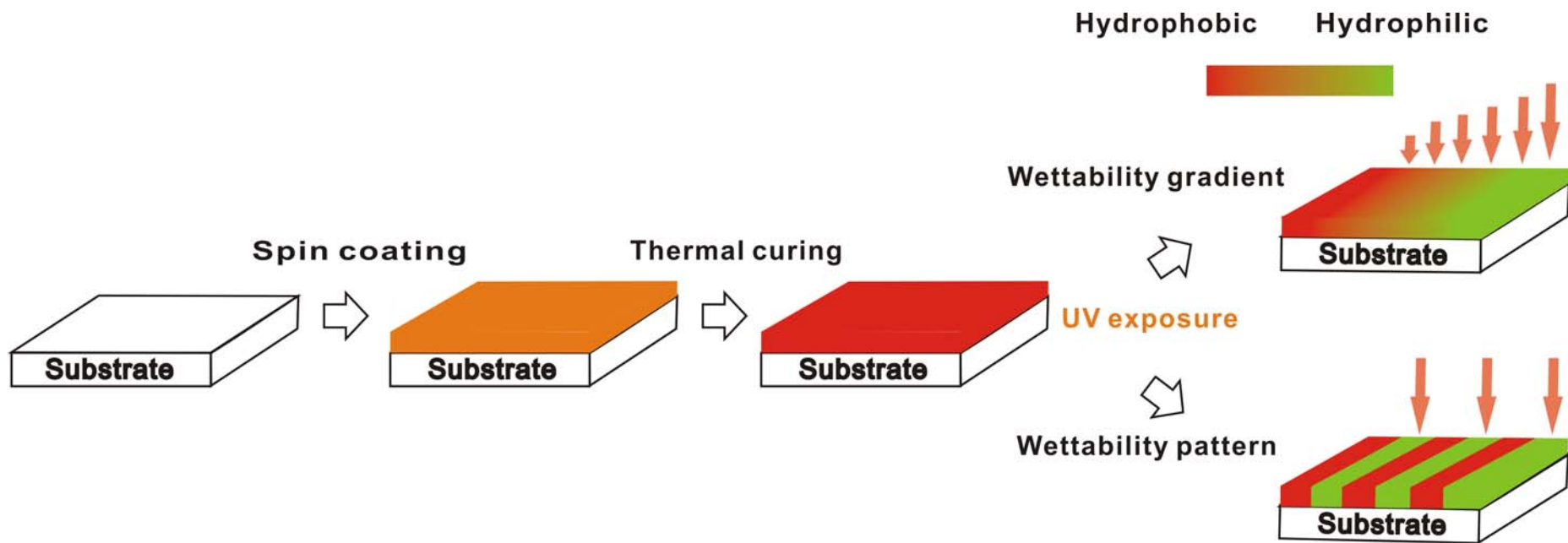


Scheme 4-1. Preparation of the allylamine-based benzoxazine monomer





Scheme 4-2. Mechanism of the B-ala photo-oxidation



Scheme 4-3. Fabrication of wettability gradients and wettability patterns on B-ala PBZ films

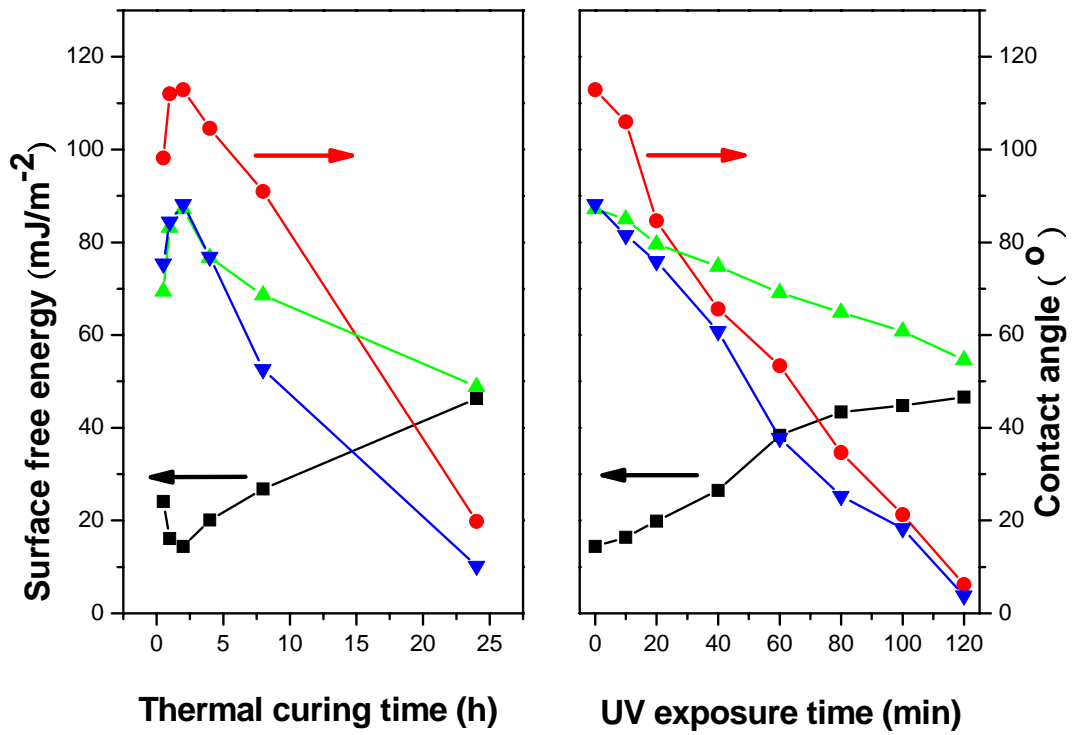


Figure 4-1. Advancing contact angles of (●)water, (▲)diiodomethane, and (▼)ethylene glycol and the respective surface free energies (γ_s) (■) of B-ala PBZ films



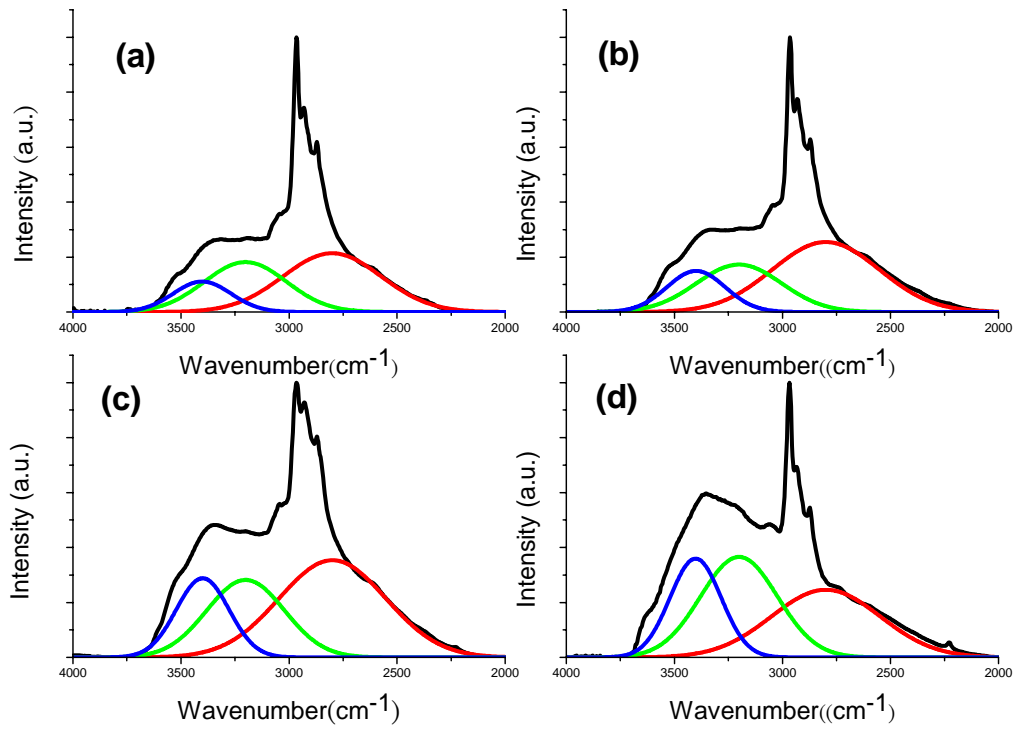


Figure 4-2. Curve fitting of the FTIR spectra of B-ala PBZ films cured at 210 °C for (a) 1, (b) 2, (c) 4, and (d) 8 h



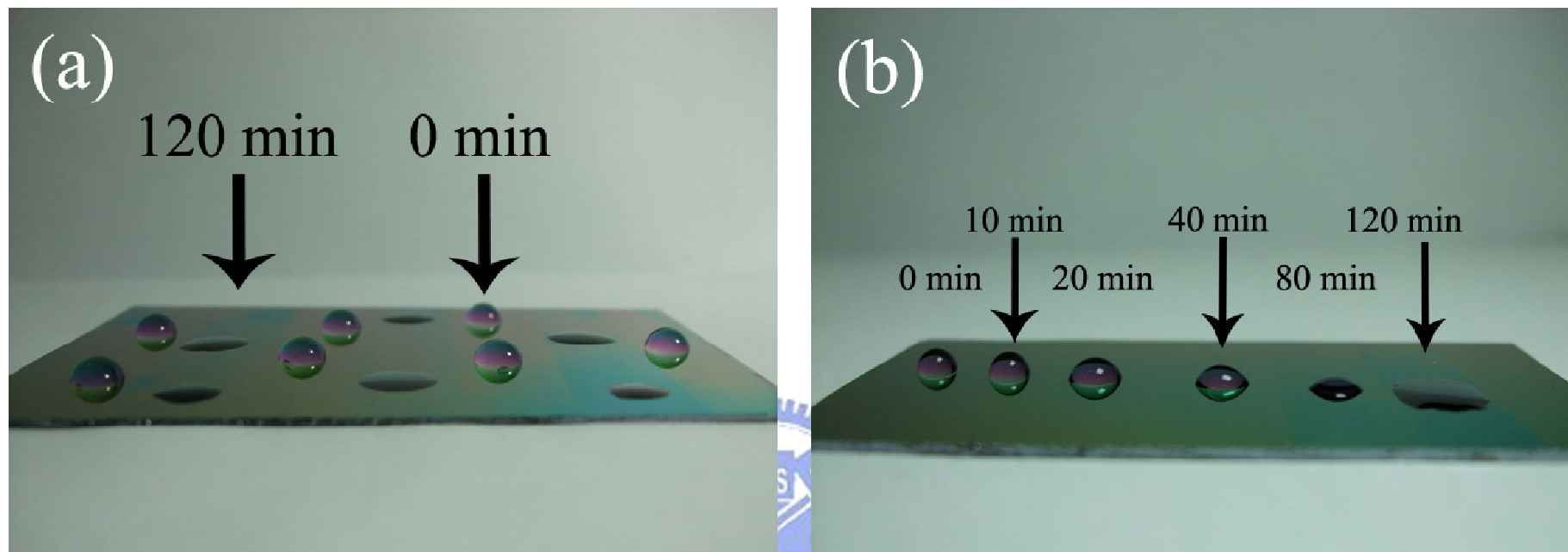


Figure 4-3. Water drops on (a) wettability pattern, (b) wettability gradient B-ala PBZ films.

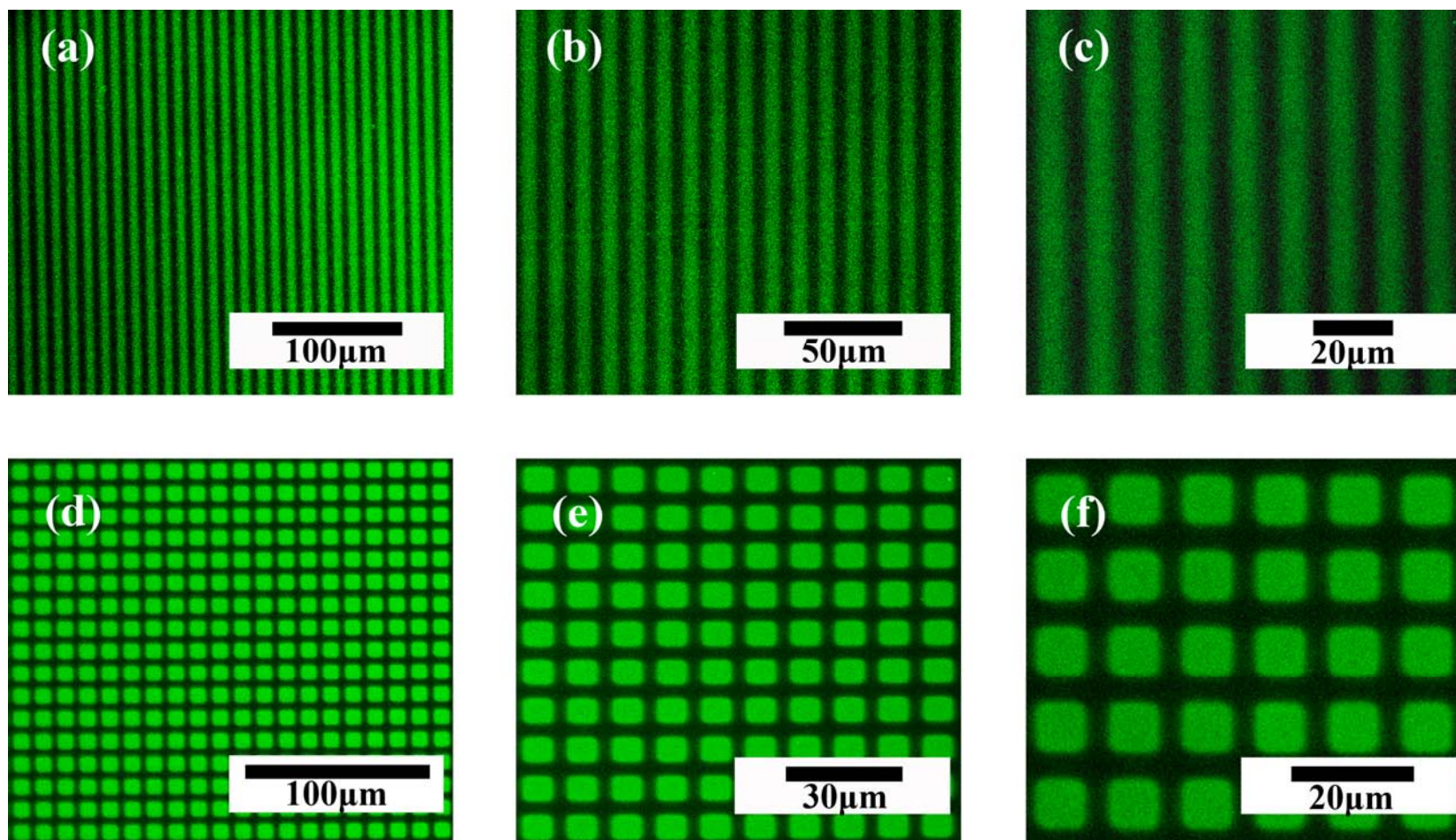


Figure 4-4. Fluorescence microscope images of periodic arrangement of arrays of CdTe colloidal nanocrystals on line patterned PBZ thin film in a magnification of (a)200 (b)400 (c)600 and square patterned PBZ thin film in a magnification of (a)200 (b)400 (c)600

Chapter 5

Fabrication of patterned superhydrophobic

Polybenzoxazine-hybrid surfaces

Abstract

The hydrophilicity of B-ala PBZ film and superhydrophobic polybenzoxazine-hybrid surface can be controlled through UV exposure to change ratio of intra- to intermolecular hydrogen bonds. Fraction of the intramolecular hydrogen bonding of the as cured sample will convert into intermolecular hydrogen bonding upon UV exposure and thus results in increase of hydrophilicity. This simple method allows for manipulating the hydrophilicity at selected regions on superhydrophobic polybenzoxazine-hybrid surface to create patterned surface with superhydrophobic and superhydrophilic regions. Besides, we have found that the superhydrophobic polybenzoxazine-silica hybrid surface exhibits good adhesion of water droplets after UV exposure which can be served as a “mechanical hand” to transfer water droplets from a superhydrophobic surface to a hydrophilic one.

5.1 Introduction

A solid surface's water repellency is one of the most important characteristics in both theoretical research and industrial applications. The wettability of solid surfaces can be controlled by surface topography and/or surface chemistry. With this controllability, many useful methods [1] have been developed to produce numerous superhydrophobic surfaces. Among these, an approach for artificial superhydrophobic surfaces [2, 3] such as mimic lotus leaves has drawn great interest where the surface is covered by branch-like nanostructure on top of micropapillae. The multiscale hierarchical structure observed in nature could be effective in manipulating important surface properties such as wettability, friction, and adhesion for electronic, optical, and biological applications. [4] The wettability of the multiscale hierarchical structure can also be alternated between superhydrophobicity and superhydrophilicity by a change in surface chemistry. [5] Wettability-switching surfaces have also been realized by applying an external stimulus, such as light irradiation, [6] electrical potential, [7] temperature, [8] and solvent. [9] While the reversibility is desirable in certain applications, however, this approach cannot be used for selective transformation of the wettability. [7-9]

Patterned surfaces with dissimilar wetting properties have been achieved using techniques such as microcontact printing, [10, 11] chemical vapor deposition, [12] and photolithography. [13-15] However, these approaches often involve complicated procedures to introduce functional groups to the patterned areas. Therefore, a simple and more effective route to generate arrays of patterns with different wetting properties and chemical functionalities is highly desirable. Furthermore, surfaces with extreme wetting properties such as superhydrophilic patterns on a superhydrophobic surface offer new possibilities in the fabrication of novel devices such as planar

microcanals (open-air microfluidic channels). [16] Open-air microfluidic channels offer advantages such as the facile handling of small amount of liquids, the possibility of massive parallel processing, direct accessibility, and ease of cleaning. [16-18] The availability of patterned surfaces with superhydrophobic and superhydrophilic regions can greatly enhance the utility and function of such devices and move us beyond nature's impressive accomplishment with the Namib beetle.

In our previous study, we have discovered that polybenzoxazine (PBZ) is a new class of nonfluorine, non-silicon low surface free energy polymeric material and the superhydrophobic polybenzoxazine hybrid surface with excellent environmental stability can be carried out by an easy two-step coating process. [19] We are unaware of any previously available methods that superhydrophilic regions can be created on the superhydrophobic polybenzoxazine hybrid surface. In this communication, we introduce a direct ultraviolet (UV)-assisted replica molding method to create superhydrophilic regions on the superhydrophobic polybenzoxazine hybrid surface. This method allows for selective wetting on polybenzoxazine thin films or superhydrophobic polybenzoxazine-hybrid surfaces by exposing to ultraviolet through an optical mask or shadow mask.

5.2 Experiment Section

5.2.1 Materials

All the chemicals were used as received. Bisphenol A and paraformaldehyde (95%) were supplied by the Showa Chemical Company of Japan. The synthesis of bis(3-allyl-3,4-dihydro-2*H*-1,3-benzoxazinyl)isopropane(B-ala) was based on the reaction of bisphenol A with allylamine and paraformaldehyde according to the previously reported procedure. [20] Column chromatography eluting with ethylacetate–hexane (2:1) was used to separate the impurities, which were identified as unreacted phenols, amines, and benzoxazine oligomers. Silica nanoparticles, Tokusil 233G, were kindly provided by the Oriental Silicas Corporation. The nanoparticle is a 22 nm precipitated hydrated silica.

5.2.2 Contact Angle Measurement

Water contact angles were determined by contact angle goniometry at 25 °C using a Krüss GH-100 goniometer interfaced with image-capture software. Water droplets (5 μ l) were dropped carefully onto the polybenzoxazine thin film or the polybenzoxazine-silica hybrid films. Each reported contact angles is the average of six measurements.

5.2.3 Fourier Transform Infrared Spectroscopy (FTIR)

All infrared spectra were recorded using a Nicolet Avatar 320 FTIR Spectrophotometer, 32 scans were collected with a spectral resolution of 1 cm⁻¹. Infrared spectrum of the polymer film was determined with the conventional potassium bromide (KBr) plate method. The sample was prepared by casting the THF solution directly onto a KBr plate and cured under conditions similar to those used in

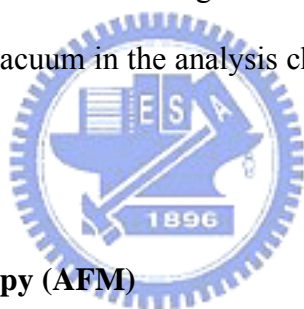
the bulk preparation. All films were thin enough to be within the absorbance range where the Beer–Lambert law is obeyed.

5.2.4 Ultraviolet Irradiation Exposure

Five 6W, low-pressure mercury lamps ($\lambda = 265$ nm) were used as an ultraviolet irradiation source. Samples were placed at 2cm from the source to receive 30 W/m^2 of radiation.

5.2.5 Electron Spectroscopy for Chemical Analysis (ESCA)

Chemical composition in the substrate surface was analyzed using a Thermo VG Scientific ESCALAB 250 Spectrometer using a monochromatic Al K α x-ray source (1486.6 eV photons) and the vacuum in the analysis chamber was maintained at about 10^{-8} mbar or lower.



5.2.6 Atomic Force Microscopy (AFM)

AFM results were acquired using a Digital Instruments multimode scanning probe microscope. Damage to both the tip and the sample surface was minimized by employing the AFM in the tapping mode. AFM images were acquired using ultrasharp silicon cantilevers having a force constant of 15 N/m. The values of root-mean-square (rms) roughness were calculated over scan areas of $5 \mu\text{m} \times 5 \mu\text{m}$. The adhesion measurements were made using silicon cantilevers having a force constant of 0.1 N/m.

5.2.7 Preparation of polybenzoxazine thin film and superhydrophobic polybenzoxazine-silica hybrid surface

One-half gram of the B-ala monomer was dissolved in 10 mL tetrahydrofuran (THF) at room temperature. The solution was then filtered through a 0.2 μm syringe filter before spin coating onto a glass slide ($50\times 50\times 1\text{ mm}^3$). 1 mL of the appropriate monomer solution was spin-coated onto a glass slide using a photoresist spinner operating at 1500 rpm for 45 s, then the sample was cured in an oven at 210°C. Superhydrophobic coating on a glass slide based on polybenzoxazine and silica nanoparticles was performed through a two-step process. First, B-ala benzoxazine (0.5 g) was mixed with nanoparticles (0.75 g) in tetrahydrofuran (THF) (10 mL). After keeping the solutions in an ultrasound bath for 2 h, the mixture was spin-coated onto a glass slide ($50\times 50\times 1\text{ mm}^3$) at 1500 rpm for 45 s and then cured in an oven at 210 °C for 1 h. Subsequently, the polybenzoxazine-silica hybrid surface was modified with 0.1% (w/v) B-ala polybenzoxazine film. The B-ala benzoxazine solution was spin coated onto a rough surface for 45 s at 1500 rpm and then cured at 210 °C for 1h.

5.3 Results and Discussion

The resulting water contact angle (CA) was about 111.3° for B-ala polybenzoxazine thin film and the contact angle for superhydrophobic polybenzoxazine-silica hybrid surface was 161.1° and the sliding angle was smaller than 3° .

PBZs feature strong intramolecular hydrogen bonds that result in extremely low surface free energies, even lower than that of pure Teflon. [19] In PBZ systems, strong intramolecular hydrogen bonding between the hydroxyl groups and the amino groups in the Mannich bridges tends to decrease the surface free energy, whereas intermolecular hydrogen bonding between hydroxyl groups results in higher surface free energies. The destruction portion of intramolecular hydrogen bonding by switching into intermolecular hydrogen bonding in PBZ system tends to increase its surface free energy and higher hydrophilicity.

Ishida et al. [21, 22] determined that C=O-containing species are formed when a bisphenol-A-based PBZ resin is exposed to UV radiation under ambient conditions. The isopropylidene linkages of PBZ are the reactive sites where oxidation and cleavage occur upon UV exposure, forming 2, 6-disubstituted benzoquinone units. The presence of these benzoquinone moieties decreases the extent of intramolecular hydrogen bonding while increasing the extent of intermolecular hydrogen bonding. Figure 5-1 shows FTIR spectra and structures of (a) B-ala monomer (b) the unirradiated B-ala polybenzoxazine (c) the B-ala polybenzoxazine irradiated for 60min and (d) the difference spectrum of (b) and (c). There are two important changes evident in the differential spectrum (Figure 5-1 (d)), the growth of the band at 1655 cm^{-1} assigned to the 2,6-disubstituted benzoquinone and a slight increase in intermolecular hydrogen bonding in the range $3550\text{--}3100\text{ cm}^{-1}$. The reason for this

difference is the reduction in intramolecular hydrogen bond by converting the hydroxyl group to carbonyl group. Table 5-1 reveals that the atomic fraction of oxygen, an indication of the degree of photo-oxidation of the surface increases after UV exposure. From Figures 5-3 (a), 5-3 (b) and 5-3 (c), we can find the growth of the peak at 294.3eV attributed to the hydrogen bonding between benzoquinone and hydroxyl group. We can also find similar result by comparing Figures 5-3 (d) and 5-3 (d). Thus, we deduce that hydrogen bondings between benzoquinone and hydroxyl group increase upon increasing the UV exposure time of B-ala PBZ films (cured 1 h at 210 °C). Besides, the O(1s) ESCA spectra of 1, 4-benzoquinone, 1, 4-benzoquinone mix with phenol at molar ratio of 2:1, B-ala polybenzoxazine thin film(cured at 210°C for 1h) and B-ala polybenzoxazine thin film(cured at 210°C for 1h) after 60min UV exposure are carried out in Figure 5-4. According to these results, the photo-oxidation reaction in B-ala PBZ system can be illustrated in Scheme 3-2.

Since the radical formation and oxidation reactions induced by UV radiation are usually concentrated at polymer surfaces, we anticipated that the surface properties of PBZ thin films would be greatly affected by their length of UV exposure. Figure 5-5 reveals that the contact angles of water decrease upon increasing the UV exposure time of B-ala PBZ films and superhydrophobic polybenzoxazine-silica hybrid surfaces. In the B-ala PBZ thin film (cured 1h at 210 °C) system, the contact angle of water decreases with increasing UV exposure time, from 111.3° to 18.6° after 60 min UV exposure. The contact angle of water for the superhydrophobic polybenzoxazine-silica hybrid surface decreases rapidly upon increasing the UV exposure time, from 161.1° to 0° after 60 min UV exposure. This behavior is consistent with a partial destruction of intramolecular hydrogen bonding and the increase in the extent of intermolecular hydrogen bonding after UV exposure and

result of higher surface free energies and higher hydrophilicity.

However, the contact angle of water is affected by surface properties, the energy of materials and surface morphology. Figure 5-6 shows SEM image and their corresponding contact angle of the polybenzoxazine-silica hybrid surface with different treatments. In addition, Figure 5-7 shows AFM image of the polybenzoxazine-silica hybrid surface with different treatments. From SEM and AFM images, the surface topography of polybenzoxazine-silica hybrid surface with different treatments remains unchanged, but the changes in the contact angles of water are dramatic. The surface topography of B-ala PBZ thin films unchange after UV irradiation exposure (Figure 5-8). The reason for the contact angle decrease upon increasing the UV exposure time of B-ala PBZ film and superhydrophobic polybenzoxazine-silica hybrid surface is due to the change of chemical composition on the surface. Therefore, we can manipulate the wettability at selected regions merely by varying the UV exposure time to create patterned surfaces containing superhydrophobic and superhydrophilic regions. Figure 5-9 (a) and 5-9 (b) present photographic images of superhydrophilic patterns upon a superhydrophobic polybenzoxazine-silica hybrid surface. In addition, good adhesion of the water droplet placed on the superhydrophobic polybenzoxazine-silica hybrid surface after 5min UV exposure was observed. For example, even when we tilted the surfaces vertically or flip them upside down, as shown in Figure 5-9 (d) and 5-9 (c), the water droplet did not slide from the surface.

The adhesion force of surface was found depending strongly on its chemical composition [23] and topography [24]. For superhydrophobic polybenzoxazine-silica hybrid surface, the change of chemical composition of surface is the major factor to increase the adhesion force because its surface topography remains unchange after

UV exposure. Furthermore, we have reported²⁵ that the presence of new polar quinone C=O functional groups on the irradiated surface led to stronger polar forces between the B-ala PBZ film and polar liquids. We have measured the adhesion force of B-ala PBZ thin films with silicon cantilevers before and after UV irradiation. The mean adhesion force for B-ala PBZ thin films before and after 5min UV irradiation were 2.66 nN and 8.12 nN. It is expected that a surface with a sufficiently high adhesive force to a liquid will have many potential application, such as in liquid transportation without loss and in the analysis of very small volumes of liquid samples. The superhydrophobic polybenzoxazine-silica hybrid surface after 5min UV exposure can be used as a “mechanical hand” to transfer small water droplets from a superhydrophobic surface to a hydrophilic one. As seen in Figure 5-10 (a), a water droplet on an ordinary superhydrophobic surface with a water contact angle as high as 161.1°. Then, we used the superhydrophobic polybenzoxazine-silica hybrid surface which have been UV irradiated 5 min to touch and adhere this water droplet 5-10 (b) until it was transferred from the ordinary superhydrophobic surface. Finally, this water droplet was released on a hydrophilic surface (poly (4-vinylphenol) thin film). We have found the droplet could be completely transferred from the ordinary superhydrophobic surface to superhydrophobic polybenzoxazine-silica hybrid surface which have been UV irradiated 5 min but a little volume was lost when the water droplet was released on a hydrophilic surface. We believe the water droplet could be completely released on a hydrophilic surface without any lost by optimizing the process condition or applying external force such as magnetic force. [26]

5.4 Conclusions

The superhydrophobic polybenzoxazine-silica hybrid surface can be prepared by an easy two-step coating process and the hydrophilicity of superhydrophobic polybenzoxazine-silica hybrid surface can be controlled through UV exposure to change the ratio of intra- to intermolecular hydrogen bonds.

This simple method allows superhydrophilic regions to be produced on superhydrophobic polybenzoxazine hybrid surface. Besides, good adhesion of the water droplet on the superhydrophobic polybenzoxazine-silica hybrid surface can be obtained after 5min UV exposure and we apply this surface as a “mechanical hand” to transfer small water droplets from a superhydrophobic surface to a hydrophilic one.



References

- [1] Feng, X.; Jiang, L. *Adv. Mater.* **2006**, *18*, 3063.
- [2] (a) Lau, K. K. S.; Bico, J.; Teo, K. B. K.; Chhowalla, M.; Amaratunga, G. A. J.; Milne, W. I.; McKinley, G. H.; Gleason, K. K. *Nano. Lett.* **2003**, *3*, 1701. (b) Jiang, L.; Zhao, Y.; Zhai, J. *Angew. Chem. Int. Ed.* **2004**, *43*, 4338.
- [3] (a) Ji, J.; Fu, J.; Shen, J. *Adv. Mater.* **2006**, *18*, 1441. (b) Gao, L.; McCarthy, T. J. *Langmuir* **2006**, *22*, 5998.
- [4] Nosonovsky, M.; Bhushan, B. *Mater. Sci. Eng. Rep.* **2007**, *58*, 162; *Langmuir* **2008**, *24*, 1525.
- [5] Bico, J.; Thiele, U.; Quere, D. *Colloids Surf. A* **2002**, *206*, 41.
- [6] (a) Lim, H. S.; Han, J. T.; Kwak, D.; Jin, M.; Cho, K. *J. Am. Chem. Soc.* **2006**, *128*, 14458. (b) Zhang, X.; Kono, H.; Liu, Z.; Nishimoto, S.; Tryk, D. A.; Murakami, T.; Sakai, H.; Abe, M.; Fujishima, A. *Chem. Commun.* **2007**, 4949. (c) Lahann, J.; Mitragotri, S.; Tran, T.; Kaido, H.; Sundaram, J.; Choi, I. S.; Hoffer, S.; Somorjai, G. A.; Langer, R. *Science* **2003**, *299*, 371. (d) Caprioli, L.; Mele, E.; Angilè, F. E.; Girardo, S.; Athanassiou, A.; Camposeo, A.; Cingolani, R. and D. Pisignano *Appl. Phys. Lett.* **2007**, *91*, 113. (e) Hozumi, A.; Kojima, S.; Nagano, S.; Seki, T.; Shirahata, N.; and Kameyama T. *Langmuir* **2007**, *23*, 3265.
- [7] (a) Lahann, J.; Mitragotri, S.; Tran, T.; Kaido, H.; Sundaram, J.; Choi, I. S.; Hoffer, S.; Somorjai, G. A.; Langer, R. *Science* **2003**, *299*, 371. (b) Prins, M. W. J.; Welters, W. J. J.; Weekamp, J. W. *Science* **2001**, *291*, 277.
- [8] (a) Crevoisier, G. B.; Fabre, P.; Corpart, J. M.; Leibler, L. *Science* **1999**, *285*, 1246. (b) Fu, Q.; Rao, G. V. R.; Basame, S. B.; Keller, D. J.; Artyushkova, K.; Fulghum, J. E.; Lopez, G. P. *J. Am. Chem. Soc.* **2004**, *126*, 8904.
- [9] Minko, S.; Muller, M.; Motornov, M.; Nitschke, M.; Grundke, K.; Stamm, M. J.

- Am. Chem. Soc.* **2003**, *125*, 3896.
- [10] Lopez, G. P.; Biebuyck, H. A.; Frisbie, C. D.; Whitesides, G. M. *Science* **1993**, *260*, 647.
- [11] Drelich, J.; Miller, J. D.; Kumar, A.; Whitesides, G. M. *Colloids Surf. A* **1994**, *93*, 1.
- [12] Sun, T.; Wang, G.; Liu, H.; Feng, L.; Jiang, L.; Zhu, D. *J. Am. Chem. Soc.* **2003**, *125*, 14996.
- [13] Tadanaga, K.; Morinaga, J.; Matsuda, A.; Minami, T. *Chem. Mater.* **2000**, *12*, 590.
- [14] Kim, H.; Kreller, C. R.; Tran, K. A.; Sisodiya, V.; Angelos, S.; Wallraff, G.; Swason, S.; Miller, R. D. *Chem. Mater.* **2004**, *16*, 4267.
- [15] Kim, H.-C.; Wallraff, G.; Kreller, C. R.; Angelos, S.; Lee, V. Y.; Volksen, W.; Miller, R. D. *Nano Lett.* **2004**, *4*, 1169.
- [16] Gau, H.; Herminghaus, S.; Lenz, P.; Lipowsky, R. *Science* **1999**, *283*, 46.
- [17] Hsu, C.-H.; Chen, C.; Folch, A. *Lab Chip* **2004**, *4*, 420.
- [18] Seemann, R.; Brinkmann, M.; Kramer, E. J.; Lange, F. F.; Lipowsky, R. *PNAS* **2005**, *102*, 1848.
- [19] (a) Wang, C. F.; Su, Y. C.; Kuo, S. W.; Huang, C. F.; Sheen, Y. C.; Chang, F. C. *Angew. Chem., Int. Ed.* **2006**, *45*, 2248. (b) Wang, C. F.; Wang, Y. T.; Tung, P. H.; Kuo, S. W.; Lin, C. H.; Sheen, Y. C.; Chang, F. C. *Langmuir* **2006**, *22*, 8289.
- [20] Liao, C. S.; Wu, J. S.; Wang, C. F.; Chang, F. C. *Macromol. Rapid Commun.* **2008**, *29*, 52.
- [21] Macko, J. A.; Ishida, H.; *J. Polym. Sci. Part B: Polym. Phys.* **2000**, *38*, 2687.
- [22] Macko, J. A.; Ishida, H. *Polymer* **2001**, *42*, 6371-6383
- [23] (a) Feldman, K.; Tervoort, T.; Smith, P.; Spencer, N. D. *Langmuir* **1998**, *14*, 372.

- (b) Tsibouklis, J.; Graham, P.; Eaton, P. J.; Smith, J. R.; Nevell, T. G.; Smart, J. D.; Ewen, R. J. *Macromolecules* **2000**, 33, 8460. (c) Eaton, P.; Smith, J. R.; Graham, P.; Smart, J. D.; Nevell, T. G.; Tsibouklis, J. *Langmuir* **2002**, 18, 3387.
- [24] (a) Jin, M; Feng, X.; Feng, L.; Sun, T.; Zhai, J.; Li, T.; Jiang, L. *Adv. Mater.* **2005**, 17, 1977. (b) Feng, L.; Zhang, Y.; Xi, J.; Zhu, Y.; Wang, N.; Xia, F.; Jiang, L. *Langmuir* **2008**, 24, 4114. (c) Boduroglu, S.; Cetinkaya, M.; Dressick, W. J.; Singh, A.; Demirel, M. C. *Langmuir* **2007**, 23, 11391.
- [25] Liao, C. S.; Wang C. F.; Lin H. C.; Chou, H. Y.; Chang, F. C. *J. Phys. Chem. C* **2008**, 112, 16189
- [26] Hong, X.; Gao, X.; Jiang L. *J. Am. Chem. Soc.* **2007**, 129, 1478 – 1479.



Table 5-1. Contact angle and ESCA oxygen content of B-ala PBZ thin film and superhydrophobic polybenzoxazine-silica hybrid surface with different UV exposure time.

UV exposure time (min)	Contact angle (°)		ESCA oxygen content (mol%)
	B-ala PBZ thin film	Superhydrophobic polybenzoxazine-silica hybrid surface	
0	111.3	161.1	21.77
5	91.3	154.1	23.80
10	89.1	139.5	24.88
20	83.4	116.8	26.70
30	71.6	95.5	26.71
40	46.6	68.9	29.29
50	33.7	9.0	30.10
60	18.6	0	30.14



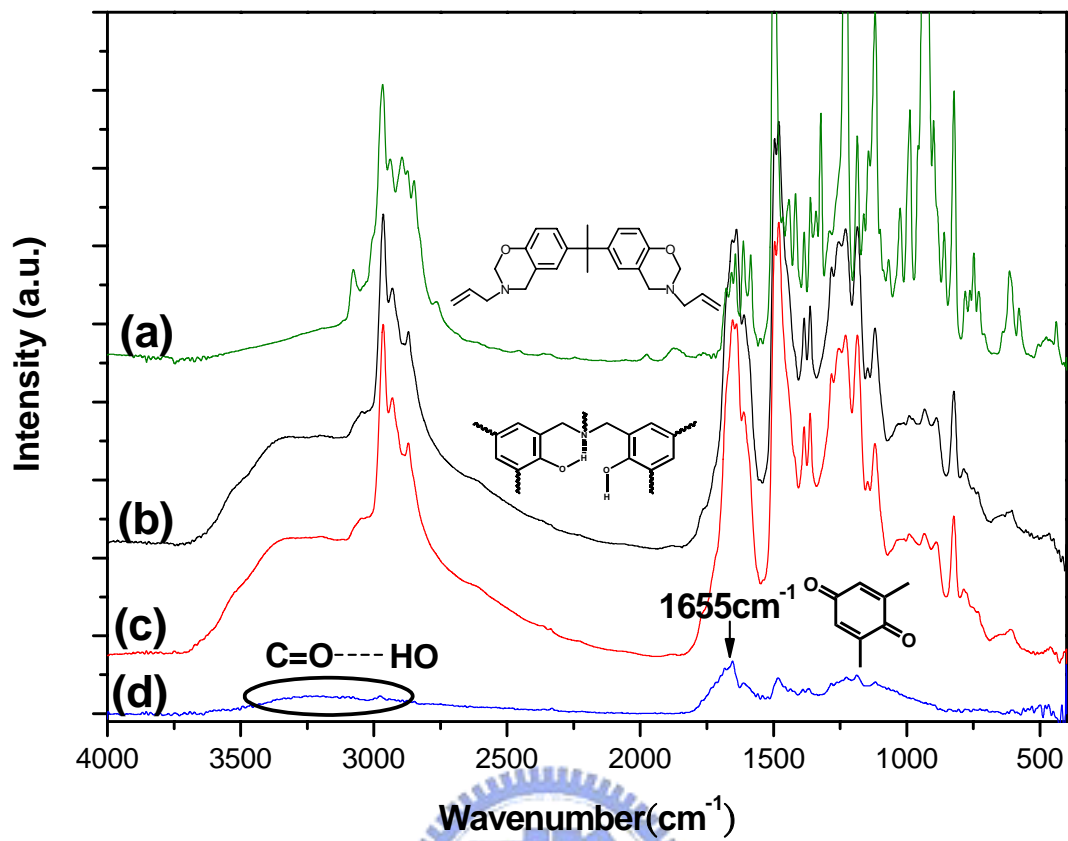


Figure 5-1. FTIR spectrum and structure of (a) B-ala monomer (b) the unirradiated B-ala polybenzoxazine (c) the B-ala polybenzoxazine irradiated for 60min and (d) the difference spectrum of (b) and (c)

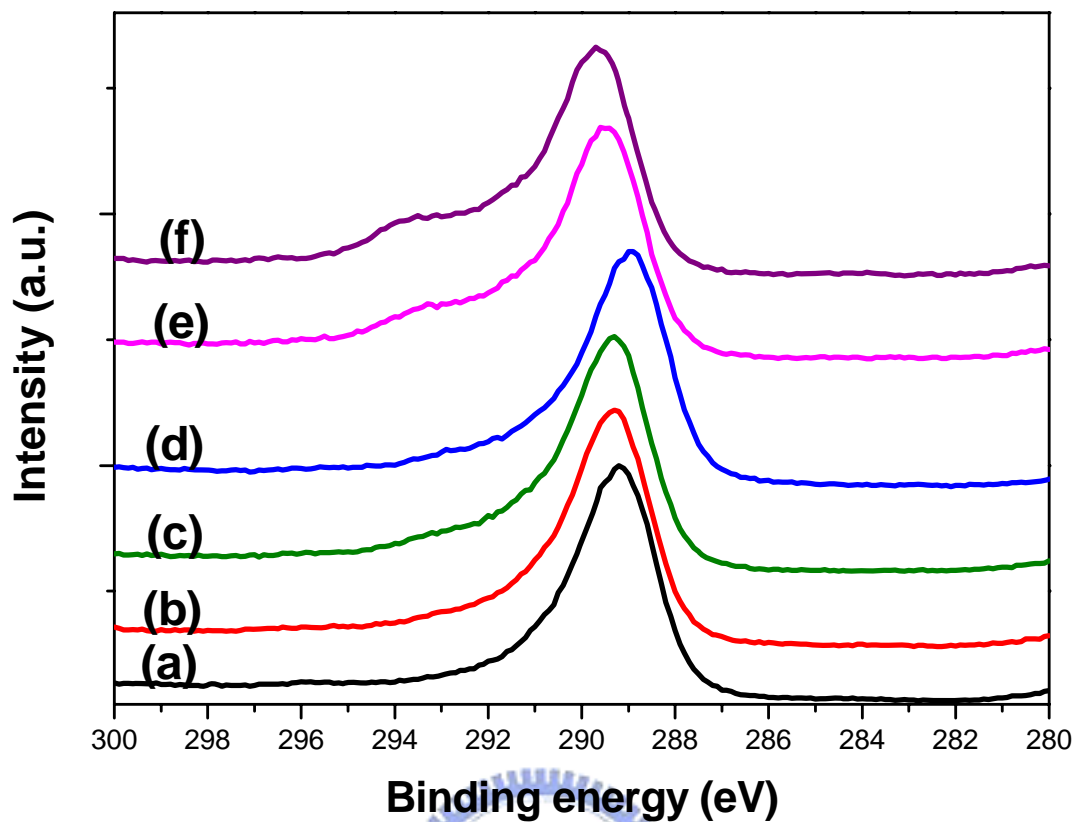


Figure 5-2. C(1s) ESCA spectrum of B-ala polybenzoxazine thin film cured 1h at 210°C with different UV exposure time (a) 0min (b) 5min (c) 10min (d) 20min (e) 40min (f) 60min

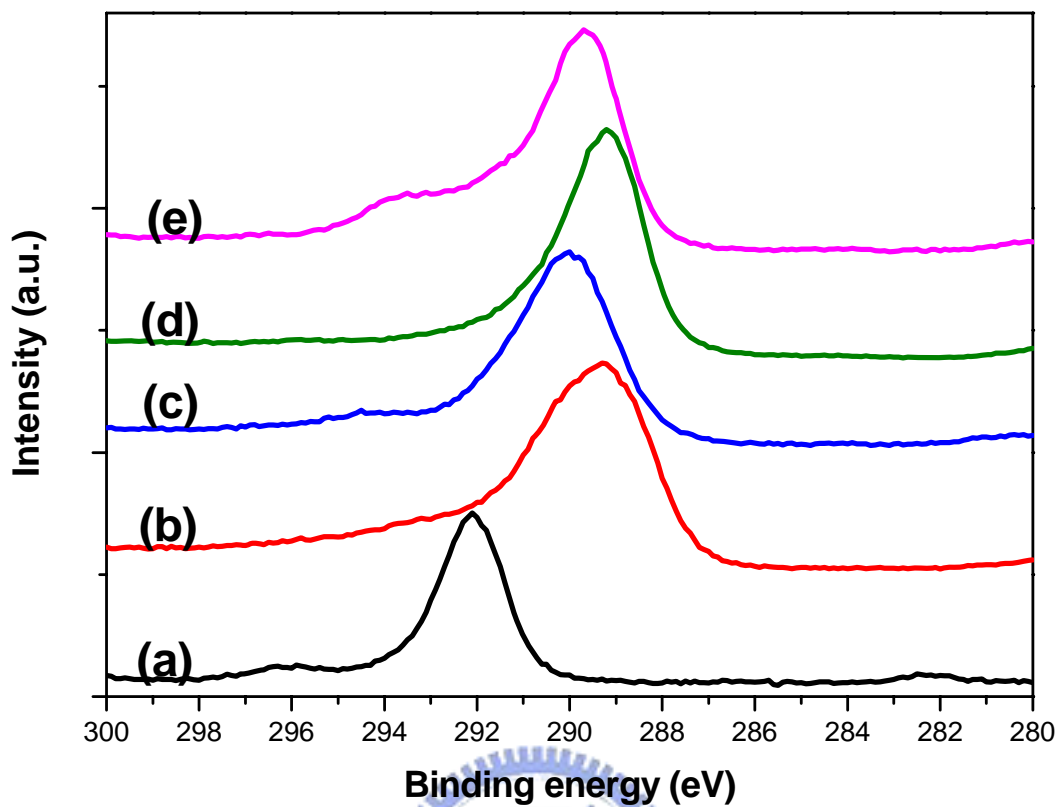


Figure 5-3. C(1s) ESCA spectrum of (a) phenol (b) 1, 4-benzoquinone (c) 1, 4-benzoquinone mix with phenol at molar ratio of 2:1 (d) B-ala polybenzoxazine thin cured at 210°C for 1h (e) d after 60min UV exposure

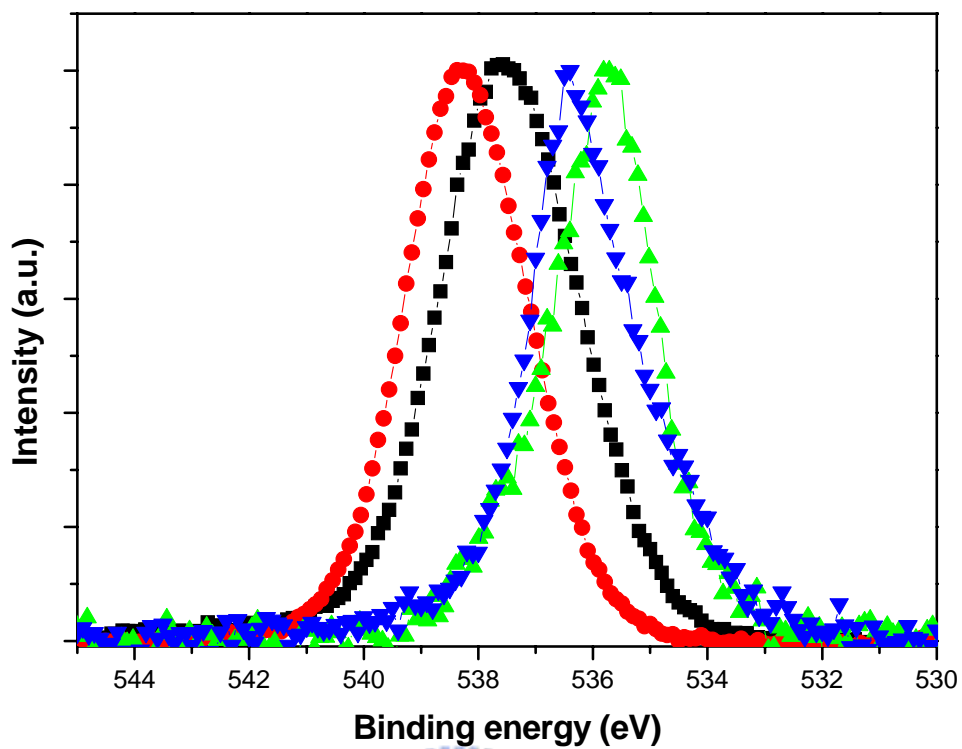


Figure 5-4. O(1s) ESCA spectrum of (■) 1, 4-benzoquinone (◆) 1, 4-benzoquinone mix with phenol at molar ratio of 2:1 (▲) B-ala polybenzoxazine thin film(cured at 210°C for 1h (▼) B-ala polybenzoxazine thin film (cured at 210°C for 1h) after 60min UV exposure

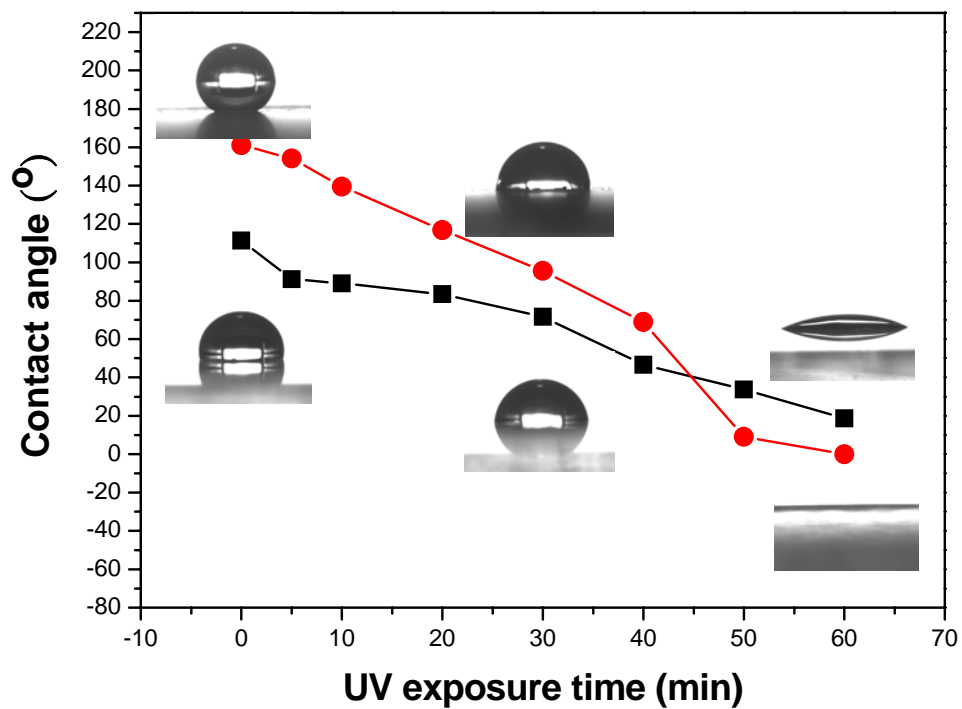


Figure 5-5. Water contact angles for (■) polybenzoxazine thin films and (●) superhydrophobic polybenzoxazine-silica hybrid surfaces with different UV exposure time.



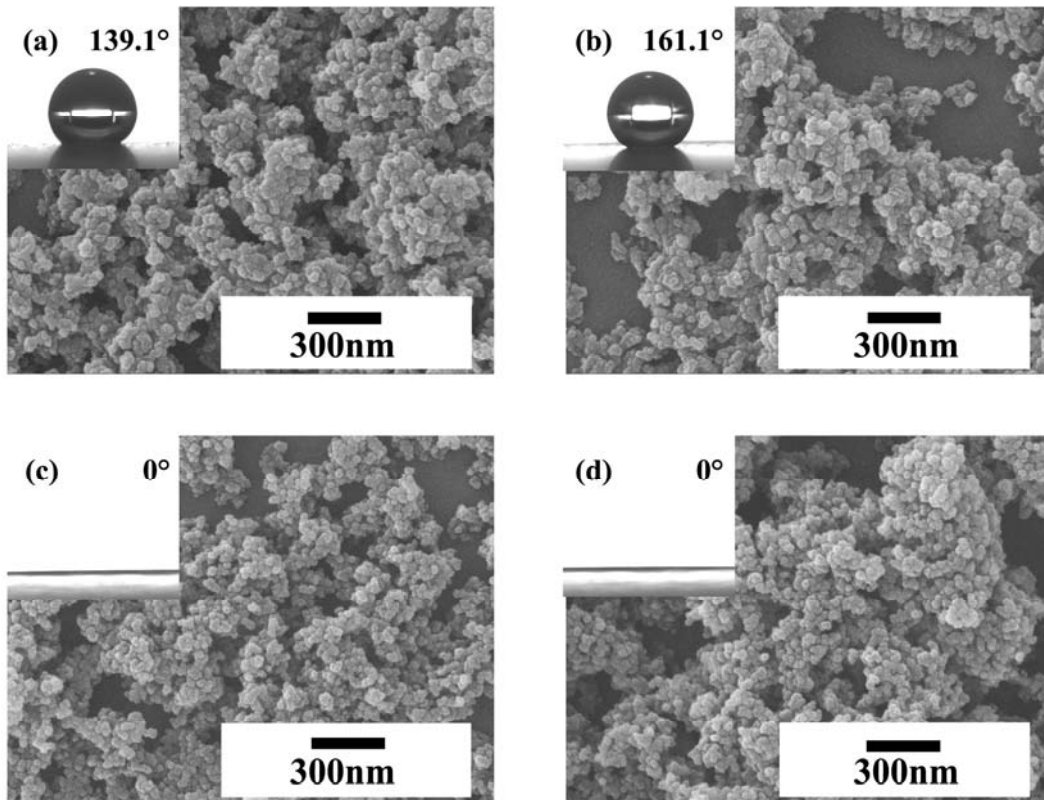


Figure 5-6. SEM image and their corresponding contact angle of (a) polybenzoxazine-silica hybrid surface (b) polybenzoxazine-silica hybrid surface modified with 0.1% pure B-ala polybenzoxazine thin film (c) b after 60min UV irradiation (d) c wash with acetone and methanol.

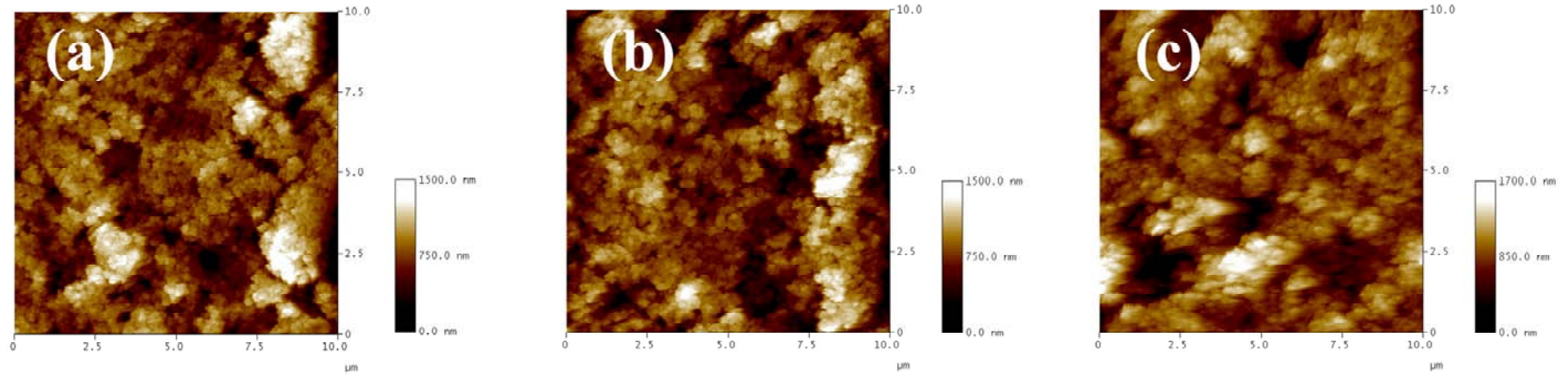
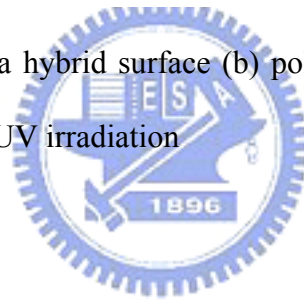


Figure 5-7. AFM images of (a) polybenzoxazine-silica hybrid surface (b) polybenzoxazine-silica hybrid surface modified with 0.1% pure B-ala polybenzoxazine thin film (c) b after 60min UV irradiation



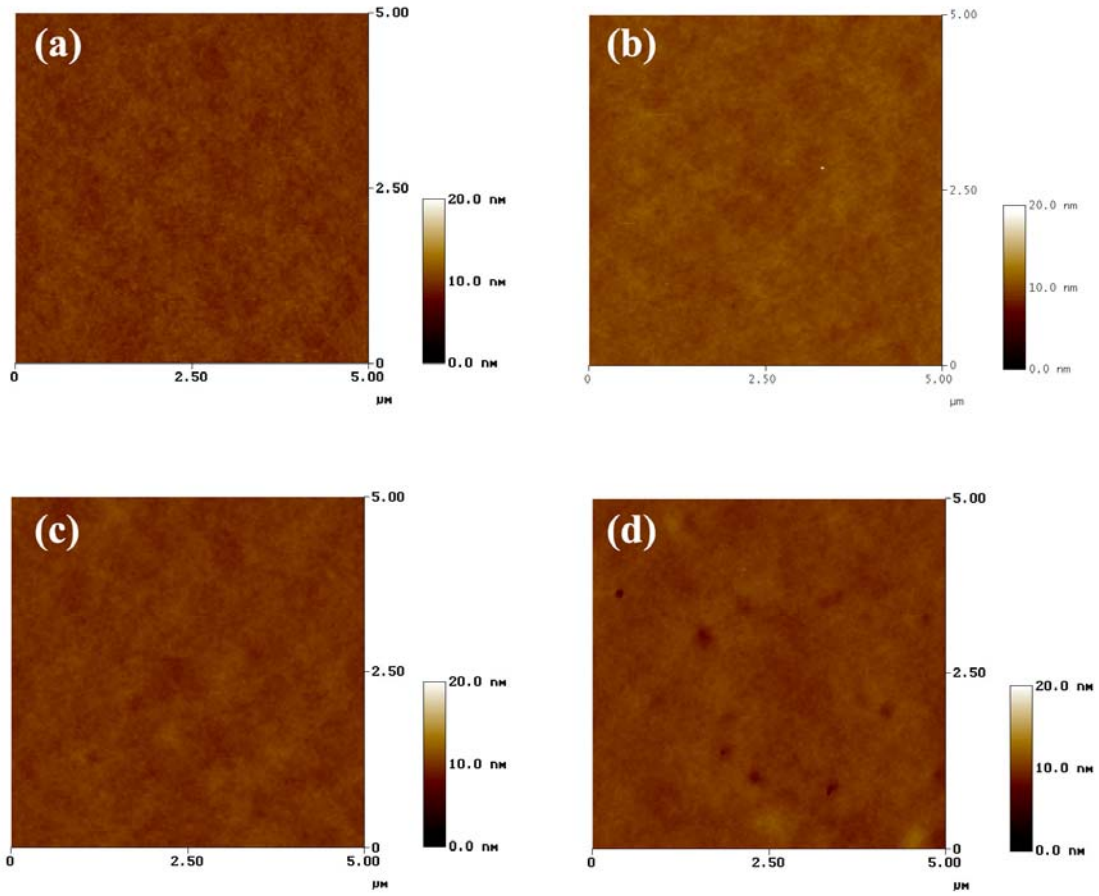


Figure 5-8. AFM images with different UV exposure time (a) 0min (b) 20min (c) 40min (d) 60min

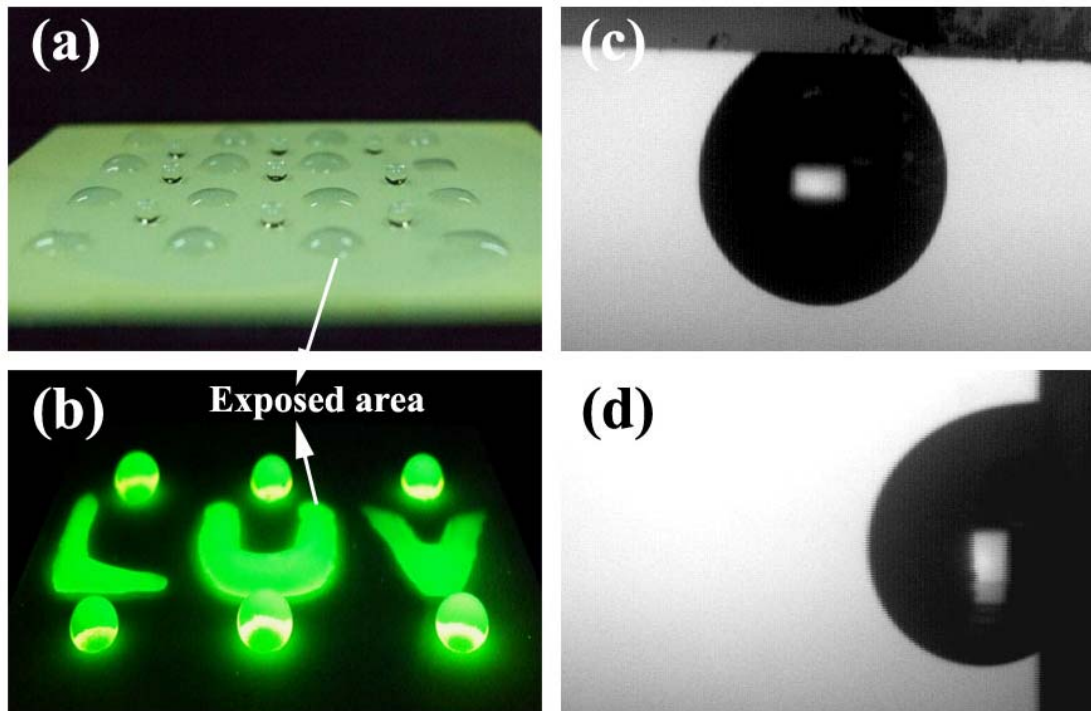


Figure 5-9. (a) Water drops on selective wetting polybenzoxazine-silica hybrid surface (b) CdTe quantum dot containing solution drops on the UV-modified polybenzoxazine-silica hybrid surface obtained with a LUV mask. Shapes of $5\mu\text{l}$ water droplets on the superhydrophobic polybenzoxazine-silica hybrid surface after 5min UV exposure with different tilt angles (c) 180° (d) 90°

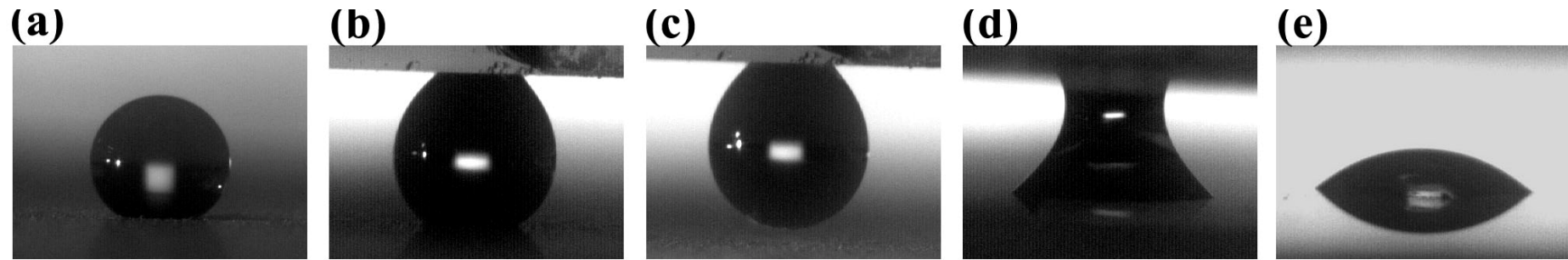


Figure 5-10. Transfer Process of a water droplet from a superhydrophobic surface to a hydrophilic one.



Chapter 6

Effect of Molecule Weight and Hydrogen Bonding on Low-Surface-Energy Material of Poly(vinylphenol)

Abstract

We discovered that a series of poly(vinylphenol-*co*-methylmethacrylate) (PVPh-*co*-PMMA) block and random copolymers possess extremely low surface energy after a simple thermal treatment procedure, even lower than that of poly(tetrafluoroethylene) (22.0 mJ/m^2) calculated on the basis of the two-liquid geometric method. The decrease of the surface energy in PVPh/PMMA systems was due to the decrease of intermolecular hydrogen-bonding fraction between hydroxyl groups of PVPh tends to decrease the surface energy and the sequence distribution of the vinylphenol group in PVPh-*co*-PMMA copolymers plays an important role in dictating the final surface energy after thermal treatment. Besides, the effects of molecule weight of PVPh on surface free energy were investigated carefully in this chapter.

6.1 Introduction

The performance of polymeric materials is often dictated by surface properties, such as wettability, friction, and adhesion. In particular, hydrophobicity and oleophobicity have attracted tremendous interest due to their wide range of applications. [1-4] Both poly(dimethylsiloxane) (PDMS) and poly(tetrafluoroethylene) (PTFE) are two well-known examples possessing low surface energies. [5-8] PTFE may be regarded as the benchmark lower surface energy material, displaying water repellency [9] in combination with other desirable properties. [10] The small size of the fluorine atom with high electronegativity, low polarizability, and strong fluorine-fluorine repulsion [11] results in weak intermolecular forces of fluorinated polymer chains and thus relatively lower surface energies. However, PTFE and many fluorinated polymers have some application limitations such as high cost and poor processibility. Many efforts have been attempted to search for low-surface-free-energy polymeric materials with low cost, easy processibility, and good film-forming characteristics. [12-14]

Hydrogen bonding plays an important role in determining the surface properties of polymers. In general, the amorphous comblike polymers possessing a flexible linear backbone on the side chain with low intermolecular interaction exhibit a low surface energy. [15] We have found that the intermolecular hydrogen bonding between the hydroxyl groups increases their surface energies in the polybenzoxazine system. [12] Jiang et al. [16] found that at temperatures above its lower critical solution temperature (LCST), the compact, collapsed conformation of poly(N-isopropylacrylamide) (PNIPAAm), induced by intramolecular hydrogen bonding between the C=O and N-H groups of the main chains results in a low surface free energy and a high contact angle for

water. When the temperature is below the LCST, however, intermolecular hydrogen bonding between the PNIPAAm main chains and water molecules predominates leading to a higher surface free energy and a lower water contact angle. Similarly, Chung et al. [17] reported that the presence of amide groups in a fluorinated-main-chain liquid-crystalline polymer system induces strong intermolecular hydrogen bonding resulting in higher surface free energies and higher degrees of hydrophilicity. The nature of the pendent chain has a most profound effect in determining the surface energy of the material; therefore, a low-surface-free-energy material can be obtained by decreasing the intermolecular interaction from the comblike polymer with a flexible linear backbone. [18] In our previous study [19], we discovered that PVPh, a fluorine- and silicone-free polymer, can possess an extremely low surface energy (15.7 mJ/m^2) after a simple thermal treatment procedure which is even lower than that of PTFE (22.0 mJ/m^2) calculated on the basis of the two-liquid geometric method. Besides, the sequence distribution of the vinylphenol group in PVPh-co-PS copolymers plays an important role in dictating the final surface energy after thermal treatment. In this chapter, we found that the PVPh-co-PMMA copolymers presents quiet different surface properties from PVPh-co-PS copolymers after thermal treatment. Furthermore, we discovered that the fraction of hydrogen bonding between vinylphenol groups and carbonyl groups not only depended on the sequence distribution of the vinylphenol group in PVPh-co-PMMA copolymers but also the casting process. The effects of molecule weight on surface free energy were also investigated carefully.

6.2 Experiment Section

6.2.1 Preparation of PVPh/PMMA Random and Block Copolymers and Blends

The detailed synthesis procedures of PVPh-*r*-PMMA and PVPh-*b*-PMMA copolymers have been reported previously. [20] Table 1 lists the characterizations of PVPh, PMMA, and PVPh/PMMA random and block copolymers. Various binary PVPh/PMMA blend compositions were prepared by solution-casting. A THF solution containing 5 wt % polymers was stirred for 6-8 h and then cast onto a wafer. The solution was left to evaporate at 60°C for 1 day and dried in vacuum at room temperature for 2 days. The thermal treatment was carried out by placing the as-prepared polymer film in a vacuum oven at 180 °C for 24 h and then quenching to ambient temperature.



6.3 Characterizations

^1H NMR spectra were recorded on a Varian Unity Inova 500 FT NMR spectrometer operated at 500 MHz; deuterated chloroform was used as the solvent. Thermal analyses were performed using a DuPont DSC-9000 differential scanning calorimeter operated at a scan rate of 20 °C/min within a temperature range from 30 to 250 °C. The sample was quenched to 20 °C from the melt state for the first scan and then rescanned between 20 and 250 °C at 20 °C/min. The glass transition temperature was obtained at the inflection point of the jump heat capacity. Thermal stabilities of as prepared samples were investigated using a DuPont 2050 TGA instrument operated at a rate of 20 °C/min from 30 to 700 °C under a nitrogen flow. Infrared spectroscopic measurements were conducted on a Nicolet Avatar 320 FTIR spectrophotometer; 32 scans were collected with a spectral resolution of 1 cm^{-1} . All sample preparations were under continuous nitrogen flow to ensure minimal sample oxidation or degradation. Surface roughness profiles of film structures were acquired using a Digital Instruments DI5000 scanning probe microscope in the tapping mode. The values of root-mean-square (rms) roughness were calculated over scan areas of 5 $\mu\text{m} \times 5\mu\text{m}$. For contact angle measurements, deionized water and diiodomethane (DIM) were chosen as testing liquids because significant amounts of data are available for these liquids. The advancing contact angle measurement of a polymer sample was determined at 25 °C after injection of a liquid drop (5 μL) onto the surface, and a Krüss GH-100 goniometer interfaced to image-capture software was employed to perform the measurement. A two-liquid geometric method was employed to determine the surface energy. [21]

6.4 Results and Discussion

6.4.1 The effect of molecule weight on surface free energy in PVPh system

The surface free energy of homologous series tends to increase, while the surface entropy tends to decrease, with increasing molecular weight. At infinite molecular weight, both the surface free energy and the surface entropy are, however, finite. The surface free energy of homologous series varies linearly with $M_n^{-2/3}$, [22, 23]

$$\gamma = \gamma_\infty - \frac{k_e}{M_n^{2/3}} \quad (2.32)$$

where γ_∞ is the surface free energy at infinite molecular weight and k_e is a constant. The surface free energy variation decreases with increasing molecular weight. However, the surface free energy of poly(vinyl acetate) melts having molecular weight 11,000-120,000 and hydrogen bonding are found to be practically independent of molecular weight according to previous report. [24]

Intra- and intermolecular interactions play important roles in determining the surface properties of polymers. In our previous study, we have found that the composition of hydrogen bonding in PVPh homopolymer changed dramatically after thermal treatment, resulting in a significant decrease in surface free energy (from 41.8 to 15.7 mJ/m²). In this chapter, we find the surface free energy of PVPh homopolymers is practically independent of molecular weight before thermal treatment process. However, the surface free energy of PVPh increases with increasing molecular weight of PVPh (Figure 6-1). This phenomenon could explain for the changes of hydrogen bonding composition in PVPh system after thermal treatment. It indicated that the surface free energy of PVPh would depend on molecular weight when the intermolecular hydrogen bonding decreased and free hydrogen bonding increased.

6.4.2 The effect of hydrogen bonding and sequence distribution in PVPh/PMMA system

Formulations and thermal properties of these synthesized copolymers are summarized in Table 6-1. It is well-known that a high temperature above T_g tends to partially disrupt hydrogen bond formation, and this is why we chose 180°C as the thermal treatment temperature and 180°C are far lower than the decomposition temperature (Table 6-1), thus the thermal treatment should not damage the polymer structure. Table 6-3 lists the surface roughness, advancing contact angles, and surface free energies of all specimens, before and after thermal treatment. The surface roughnesses of all specimens are lower than 5 nm; therefore, the influence of topography on the surface free energy is negligible. The advancing contact angle is relatively less sensitive to surface roughness and heterogeneity than the receding angle; thus, the advancing contact angle data are commonly used to calculate the components of surface and interfacial tension. [25, 26] In our previous study, we have found that the surface free energy of PVPh homopolymer decreases substantially after thermal treatment, resulting in a significant decrease in surface free energy (from 41.8 to 15.7 mJ/m²) and the sequence distribution of the vinylphenol group in PVPh-*co*-PS copolymers plays an important role in dictating the final surface energy after thermal treatment. In this chapter, we change the immiscible PVPh-*co*-PS copolymer to miscible PVPh-*co*-PMMA copolymer to investigate the effect of hydrogen bonding between PVPh and PMMA on the surface free energy. Before we discussed the effect of hydrogen bonding between PVPh and PMMA on the surface free energy we studied the preparing process effect of hydrogen bonding first. From Figure 6-2, we find pure PVPh homopolymer possesses quite different FTIR spectrum after

different preparing process. Different from solvent casting process, the PVPh homopolymer prepared from spin coating process possessed higher content of the free hydroxyl group and the hydroxyl groups involved in intramolecular hydrogen bonding. According to previous studies, solvent-cast films from volatile solutions such as chloroform, toluene or tetrahydrofuran may not be thermodynamically equilibrated due to rapid solvent evaporation during the spin-casting process, and the resulting surface could primarily be the result of solvent effects. [27, 28] Thus, the hydrogen bonding of PVPh homopolymer prepared from spin coating process would not be thermodynamically equilibrated. During the rapid solvent evaporation we believe that it is more favorable to form hydrogen bonds from neighboring hydroxyl groups and free hydroxyl groups in PVPh system. Thus, the higher content of the free hydroxyl group and the hydroxyl groups involved in intramolecular hydrogen bonding than it prepared from solvent casting. In our previous report, [19] it is more favorable to re-form hydrogen bonds from neighboring hydroxyl groups or those in the vicinity (most likely from the same chain, defined as an intramolecular hydrogen bond) in PVPh system after 180°C thermal treatment. This is probably the reason for PVPh homopolymer prepared from 180°C thermal treatment possessed higher content of the free hydroxyl group and the hydroxyl groups involved in intramolecular hydrogen bonding than it prepared from spin coating process and casting process.

For PVPh-co-PMMA copolymer system, we have reported that the hydrogen-bonding strength of poly (vinylphenol-co-methyl methacrylate) copolymers depended on sequence distribution and polydispersity index due to its intramolecular screening and functional group accessibility effects. [20] The FTIR spectra shown in

Figure 6-3 (a) and 6-3 (b) are good evidences for intramolecular screening and functional group accessibility effects. However, the FTIR spectra shown in Figure 6-3 (c) and 6-3 (d) are quite different from Figure 6-3 (a) and 6-3 (b). The carbonyl stretching band for PMMA appears at 1730 cm^{-1} and the peak at 1705 cm^{-1} corresponding to the hydrogen-bonded carbonyls and they can be fitted well to the Gaussian function (Table 6-2). From Figure 6-3 (c), we can find that the hydrogen-bonded carbonyls are few in PVPh/PMMA blends and PVPh-PMMA block copolymer except in PVPh-PMMA random copolymer. Furthermore, we find the similar phenomenon in the FTIR spectra of all polymer films (Figure 6-4) which prepared by spin coating process. From mention above, the reason for this phenomenon is due to rapid solvent evaporation during the spin-casting process. [27, 28] We deduced that it is more favorable to form hydrogen bonds from neighboring hydroxyl groups and carbonyls during the spin coating process. As a result, there is more hydrogen-bonded carbonyl can be found in PVPh-PMMA random copolymer.

From Table 6-3, we find all polymer specimens possess lower surface free energy after thermal treatment. In our previous report, we deduced that the decrease of surface energy is due to the decrease of the intermolecular hydrogen-bonding interaction for PVPh system. For clarity, the spectra display the hydroxyl stretching region between 2800 and 3800 cm^{-1} and the carbonyl stretching region between 1660 and 1800 cm^{-1} are shown in Figure 6-5, 6-6 and 6-7. According to a recent study, [29] the -OH band can be fitted by three Gaussian functions: a narrower shoulder band at 3525 cm^{-1} represents the free hydroxyl group, the peak at $\nu \doteq 3280\text{ cm}^{-1}$ corresponds to the hydroxyl groups involved in intermolecular hydrogen bonding, and the peak at $\nu \doteq 3420\text{ cm}^{-1}$ corresponds

to the hydroxyl groups involved in intramolecular hydrogen bonding. Besides, the band at 3440 cm^{-1} represents the hydroxyl groups interacting with carbonyl groups. [20] We find all polymer films possess fewer fractions of the hydroxyl groups involved in intermolecular hydrogen bonding resulting in lower surface free energy after thermal treatment in Figure 6-6. Most of intermolecular hydrogen bondings of hydroxyl groups convert into free hydroxyl groups, intramolecular hydrogen bonding and hydrogen bonding between hydroxyl groups and carbonyl groups after thermal treatment.

In our previous work, [30] we have studied the effect of an inert diluent segment on the miscibility behavior of PVPh-*r*-PS copolymers and found that the incorporation of a styrene moiety into the PVPh polymer chain can dilute and decrease the strong self-association in the PVPh component. The spacing of these vinylphenol groups tends to decrease the average hydroxyl-hydroxyl distance and increase the fraction of free hydroxyl in PVPh/PS random copolymers and provides a positive effect to lower the surface energy of the polymer. However, the contact angles and resulting γ_s of PVPh/PS blends show no significant change before or after $180\text{ }^\circ\text{C}$ thermal treatment in PVPh/PS systems because of surface enrichment of PS segment. [19] We find miscible polymers, PVPh-co-PMMA, with different sequence distribution present different surface properties from immiscible PVPh-co-PS copolymers because of its hydrogen bonding between hydroxyl groups and carbonyl groups. It is interesting to note that the surface free energy of PVPh/PMMA blends increase with the increasing of PMMA content and the PVPh-*r*-PMMA and PVPh-*b*-PMMA copolymers possess the most drastic reduction in surface energy after the thermal treatment (Figure 6-8). In the PVPh/PS systems, the interference of the styrene segment tends to prevent the vinylphenol segment from

migrating to the surface, which can be regarded as a negative effect, i.e., an increase in the surface energy of the material. Thus, the PVPh-*r*-PS copolymers possess the most drastic reduction in surface energy after the thermal treatment in comparison with corresponding block copolymers and blends under comparable compositions. From the second-run DSC data of both PVPh-*co*-PMMA copolymers and PVPh/PMMA blends, revealing that essentially all PVPh/PMMA specimens possess only one glass transition temperature. Single glass transition temperature strongly suggests that these systems are fully miscible and possess a homogeneous amorphous phase. Besides, it has been reported that hydrogen bonding interaction would reduce surface enrichment. [31] As a result, there is no surface enrichment occurs in PVPh/PMMA blends and block copolymers.

To further investigate the importance of hydrogen bonding between the hydroxyls and carbonyls, we turn our attention back to the FTIR spectra of the carbonyl stretching region between 1660 and 1800 cm^{-1} of PVPh/PMMA random and block copolymers and their corresponding blends were shown in Figure 6-7. From Figure 6-7, we clearly know that the fraction of hydrogen bonded carbonyl group increases after 180°C 24 h thermal treatment. It indicates that we increase the interaction between PVPh segment and PMMA segment after thermal treatment. For PVPh/PMMA random and block copolymers we speculated that it is more favorable to re-form hydrogen bonds from neighboring hydroxyl groups or carbonyl groups in the vicinity (most likely from the same chain, defined as an intramolecular hydrogen bond) resulting in the most drastic reduction in surface energy after the thermal treatment. Unlike PVPh/PMMA random and block copolymers, the surface free energy of PVPh/PMMA blends increases with the

increasing of PMMA content (Figure 6-8). Different from PVPh (after 180°C 24 h thermal treatment), PMMA homopolymer possessed higher surface free energy. In addition, intermolecular hydrogen bonding between hydroxyl groups and carbonyls increased after 180°C 24h thermal treatment. Thus, the surface free energy of PVPh/PMMA blends increases with the increasing of PMMA content.



6.5 Conclusions

In conclusion, we found the the surface free energy of PVPh homopolymer would depend on molecular weight after 180°C 24h thermal treatment because of decreasing of intermolecular hydrogen bonding and increasing of free hydroxyl groups. In addition, we also found that the decrease of the intermolecular hydrogen-bonding fraction between hydroxyl groups of PVPh in PVPh/PMMA systems through a simple thermal treatment procedure tends to decrease the surface energy. The sequence distribution of the vinylphenol group in PVPh-*co*-PMMA copolymers would not affect the final surface energy after thermal treatment. Besides, there is no surface enrichment occurs in PVPh/PMMA systems because of its hydrogen bonding between hydroxyl groups and carbonyl groups.



References

- [1] Li, H.; Wang, X.; Song, Y.; Liu, Y.; Li, Q.; Jiang, L.; Zhu, D. *Angew. Chem. Int., Ed.* **2001**, *40*, 1743.
- [2] Aussillous, P.; Quere, D. *Nature* **2001**, *411*, 924.
- [3] Shirtcliffe, N. J.; McHale, G.; Newton, M. I.; Perry, C. C. *Langmuir* **2005**, *21*, 937.
- [4] Wang, S.; Feng, L.; Liu, H.; Sun, T.; Zhang, X.; Jiang, L.; Zhu, D. *ChemPhysChem* **2005**, *6*, 1475.
- [5] Coulson, S. R.; Woodward, I.; Badyal, J. P. S.; Brewer, S. A.; Willis, C. J. *Phys. Chem. B* **2000**, *104*, 8836.
- [6] Jin, M.; Feng, X.; Xi, J.; Zhai, J.; Cho, K.; Feng, L.; Jiang, L. *Macromol. Rapid Commun.* **2005**, *26*, 1805.
- [7] Feng, L.; Zhang, Z.; Mai, Z.; Ma, Y.; Liu, B.; Jiang, L.; Zhu, D. *Angew. Chem., Int. Ed.* **2004**, *43*, 2012.
- [8] Hillborg, H.; Tomczak, N.; Olah, A.; Schonherr, H.; Vancso, G. J. *Langmuir* **2004**, *20*, 785.
- [9] Wu, S. *Polymer Interface and Adhesion*; Marcel Dekker: New York, 1982.
- [10] Feiring, A. E.; Imbalzano, J. F.; Kerbow, D. L. *Adv. Fluoroplast. Plast. Eng.* **1994**, 27.
- [11] Carlson, D. P.; Schmiegel, W. *Ullmann's Encyclopedia of Industrial Chemistry*; VCH Verlagsgesellschaft: Weinheim, Germany, 1988; p 393.
- [12] Wang, C. F.; Su, Y. C.; Kuo, S. W.; Huang, C. F.; Sheen, Y. C.; Chang, F. C. *Angew. Chem., Int. Ed.* **2006**, *45*, 2248
- [13] Kobayashi, H.; Owen, M. J. *Trends Polym. Sci.* **1995**, *3*, 5.



- [14] Schmidt, D. L.; Coburn, C. E.; DeKoven, B. M.; Potter, G. E.; Meyers, G. F.; Fischer, D. A. *Nature* **1994**, *368*, 41.
- [15] Owen, M. J. *Comments Inorg. Chem.* **1988**, *7*, 195.
- [16] Sun, T.; Wang, G.; Feng, L.; Liu, B.; Ma, Y.; Jiang, L.; Zhu, D. *Angew. Chem. Int. Ed.* **2004**, *43*, 357-360.
- [17] Ma, K. X.; Chung, T. S. *J. Phys. Chem. B* **2001**, *105*, 4145-4150.
- [18] Tsibouklis, J.; Graham, P.; Eaton, P. J.; Smith, J. R.; Nevell, T. G.; Smart, J. D.; Ewen, R. J. *Macromolecules* **2000**, *33*, 8460.
- [19] Lin, H. C.; Wang, C. F.; Kuo, S. W.; Tung, P. H.; Huang, C. F.; Lin, C. H.; Chang, F. *C. J. Phys. Chem. B* **2007**, *111*, 3404.
- [20] Lin, C. L.; Chen, W. C.; Liao, C. S.; Su, Y. C.; Huang, C. F.; Kuo, S. W.; Chang, F. *C. Macromolecules* **2005**, *38*, 6435.
- [21] Fowkes, F. W. In *Adhesion and Adsorption of Polymers, Polymer Science and Technology*; Lee, L. H., Ed.; Plenum Press: New York, **1980**; Vol. 12A, p 43.
- [22] D. G. LeGrand, G. L. Gaines, Jr., *J. Colloid Interface Sci.* **1969**, *31*, 162.
- [23] D. G. LeGrand, G. L. Gaines, Jr., *J. Colloid Interface Sci.* **1973**, *42*, 181.
- [24] S. Wu, *J. Colloid Interface Sci.* **1969**, *31*, 153.
- [25] Xu, Y.; Graf, J.; Painter, P. C.; Coleman, M. M. *Polymer* **1991**, *32*, 3103.
- [26] Wang, L. F.; Pearce, E. M.; Kwei, T. K. *J. Polym. Sci., Polym. Phys. Ed.* **1991**, *29*, 619.
- [27] Garbassi, F.; Morra, M.; Occhiello, E. *Polymer Surfaces: from Physics to Technology*; John Wiley & Sons: Chichester, 1998; p 291.
- [28] Green, P. F.; Christensen, T. M.; Russell, T. P.; Jerome, R. *J. Chem. Phys.* **1990**, *92*,

1478-1482.

- [29] Yuan, F.; Wang, W.; Yang, M.; Zhang, X.; Li, J.; Li, H.; He, B. Minch, B.; Lieser, G.; Wegner, G. *Macromolecules* **2006**, *39*, 3982.
- [30] Kuo, S. W.; Chang, F. C. *J. Polym. Sci., Part B: Polym. Phys.* **2002**, *40*, 1661.
- [31] Duan, Y.; Pearce, E. M.; Kwei, T. K. Hu, X.; Rafailovich, M.; Sokolov, J.; Zhou, K.; Schwarz, S. *Macromolecules*, **2001**, *34* (19), 6761-6767



Table 6-1. Formulations and thermal properties of PVPh-*co*-PMMA copolymers and corresponding Blends

copolymer	phenol ratio ^a (mol %)	M_n^b	M_w/M_n^b	T_g (°C)	T_d (°C)
PMMA	0	22000	1.29	105.0	346.5
PVPh10-r-PMMA90	10	18000	1.85	130.3	310.7
PVPh30-r-PMMA70	30	18000	1.64	143.0	315.6
PVPh50-r-PMMA50	50	19000	1.68	151.5	325.9
PVPh76-r-PMMA24	76	17000	1.51	166.7	362.0
PVPh92-r-PMMA8	92	16000	1.67	173.7	362.1
PVPh10-b-PMMA90	10	37000	1.15	143.1	373.3
PVPh30-b-PMMA70	30	16000	1.11	155.0	372.0
PVPh44-b-PMMA56	44	16000	1.15	163.4	370.5
PVPh55-b-PMMA45	55	30000	1.10	164.5	368.0
PVPh75-b-PMMA25	75	22000	1.13	176.7	365.0
PVPh10/PMMA90	10			124.4	359.9
PVPh30/PMMA70	30			135.5	353.1
PVPh50/PMMA50	50			147.8	351.8
PVPh70/PMMA30	70			159.2	345.9
PVPh90/PMMA10	90			166.8	343.6
PVPh	100	20000	1.07	186.8	372.1

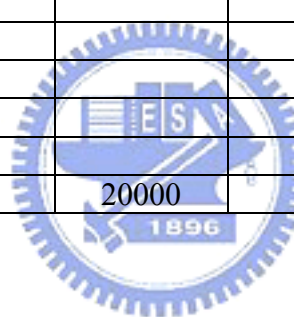


Table 6-2. Results of Curve-Fitting the Data for PVPh-*co*-PMMA and PVPh/PMMA Blends with different process at Room temperature

copolymer	H-bonded C=O			Free C=O			f_b^a
	ν , cm^{-1}	$W_{1/2}$, cm^{-1}	A_b , %	ν , cm^{-1}	$W_{1/2}$, cm^{-1}	A_b , %	
<i>Solvent casting</i>							
PVPh/PMMA=50/50	1707	25	17.2	1732	19	82.8	12.2
PVPh44-b-PMMA56	1707	24	45.8	1735	19	54.2	36.1
PVPh50-r-PMMA50	1704	24	49.2	1731	19	50.8	39.2
<i>Spin coating</i>							
PVPh/PMMA=50/50	1707	25	11.4	1731	19	88.6	7.9
PVPh44-b-PMMA56	1707	24	13.8	1731	19	86.2	9.6
PVPh50-r-PMMA50	1706	25	44.5	1731	19	55.5	34.8
<i>180°C thermal treatment</i>							
PVPh/PMMA=50/50	1708	24	34.7	1731	19	65.3	26.2
PVPh44-b-PMMA56	1708	24	38.9	1732	19	61.1	29.8
PVPh50-r-PMMA50	1707	25	42.5	1732	19	57.5	33.0

^a: fraction of hydrogen bonded carbonyl group.



Table 6-3. Root-mean-square surface roughness, advancing contact angle for water and diiodomethane and surface Free energy of PVPh/PMMA Copolymers

polymer	Before 180°C thermal treatment				After efore 180°C thermal treatment			
	Roughness (nm)	Contact angle (deg)		γ (mJ/m ²)	Roughness (nm)	Contact angle (deg)		γ (mJ/m ²)
H ₂ O		DIM	H ₂ O			DIM		
PVPh	2.1	75.6	47.8	37.9	2.2	107.0	86.6	14.5
PVPh/PMMA=10/90	1.4	103.4	48.4	37.0	1.4	89.5	60.2	28.7
PVPh/PMMA=30/70	2.1	98.7	48.1	36.1	2.3	92.6	66.6	25.4
PVPh/PMMA=50/50	2.0	95.9	48.5	35.4	1.8	96.6	69.3	23.5
PVPh/PMMA=70/30	1.2	92.55	47.5	35.7	1.2	85.8	76.7	23.5
PVPh/PMMA=90/10	1.5	90.2	48.3	35.2	1.5	103.5	80.9	17.3
PVPh10-b-PMMA90	1.8	95.1	52.9	32.7	1.5	100.0	84.9	16.2
PVPh30-b-PMMA70	2.1	91.5	52.3	33.0	1.7	103.0	86.7	15.0
PVPh44-b-PMMA56	1.7	83.4	52.4	33.8	1.7	105.3	87.9	14.2
PVPh55-b-PMMA45	1.3	82.3	53.2	33.7	1.5	105.8	88.2	14.0
PVPh75-b-PMMA25	1.5	80.3	54.6	33.6	1.5	105.9	88.2	13.9
PVPh10-r-PMMA90	2.3	101.3	53.1	33.3	2.1	102.5	82.6	16.6
PVPh30-r-PMMA70	1.1	93.2	53.5	32.3	1.5	104.1	84.8	15.5
PVPh50-r-PMMA50	1.3	91	53.5	32.3	1.3	105.6	88.5	13.9
PVPh76-r-PMMA24	1.4	81.8	53.5	33.7	1.4	106	89	13.7
PVPh92-r-PMMA8	1.2	79.6	53.1	34.4	1.2	106.3	89	13.6
PMMA	2.0	108.4	48.8	38.3				

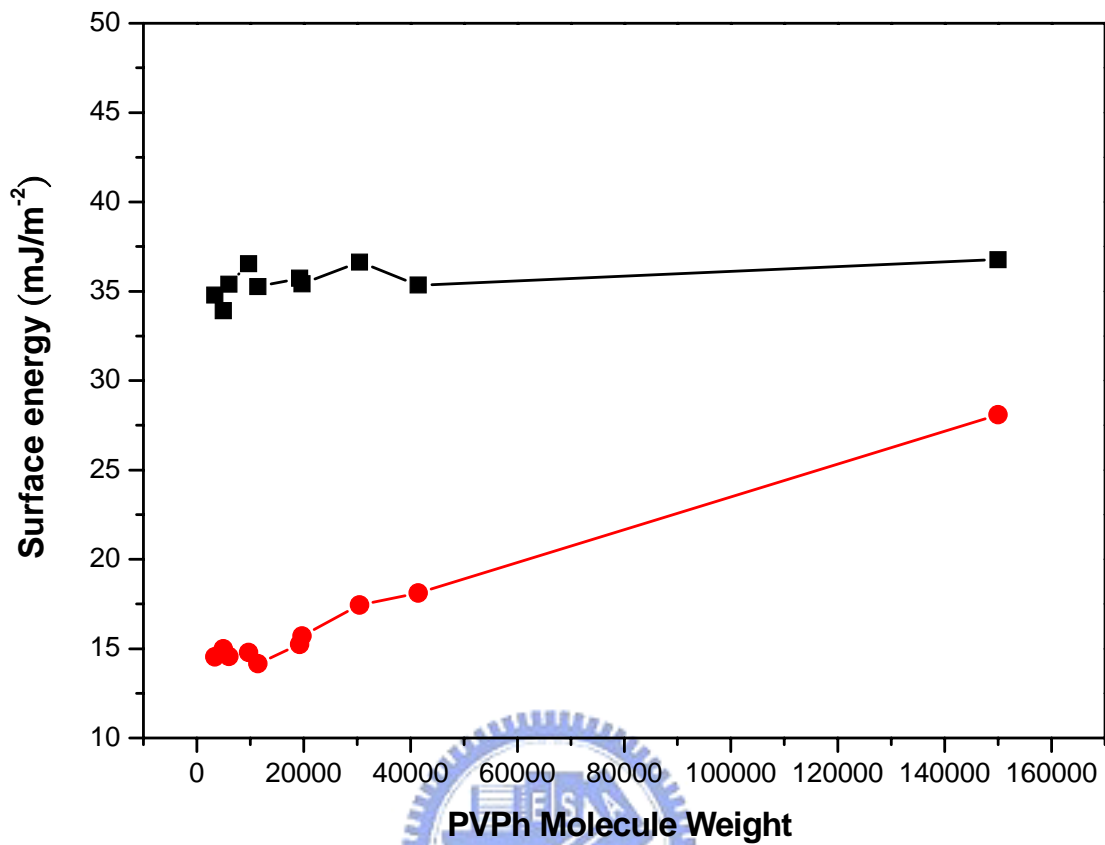


Figure 6-1. Surface energy of PVPh homopolymers with different molecule weight (■) at room temperature and (●) after 180 °C thermal treatment process.

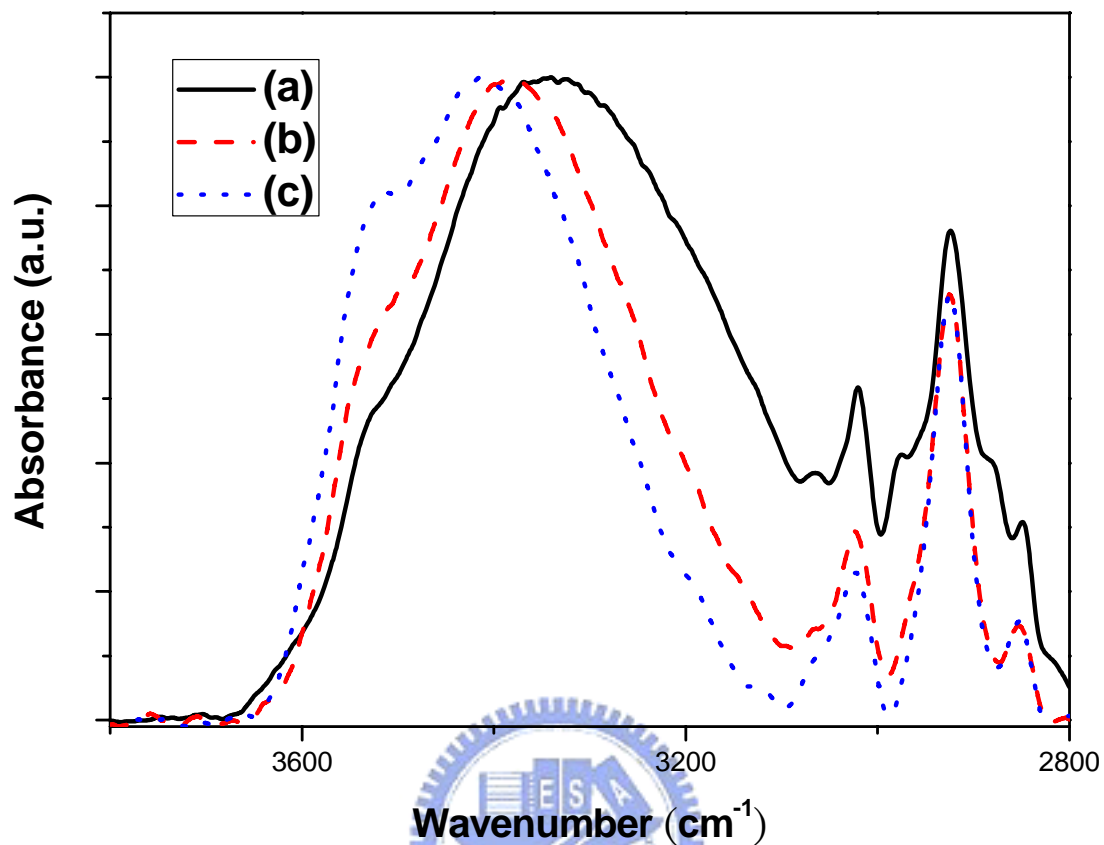


Figure 6-2. The FTIR spectra of pure PVPh homopolymer (M_w = 9697) (a) solvent casting (b) spin coating (c) 180 °C 24h thermal treatment.

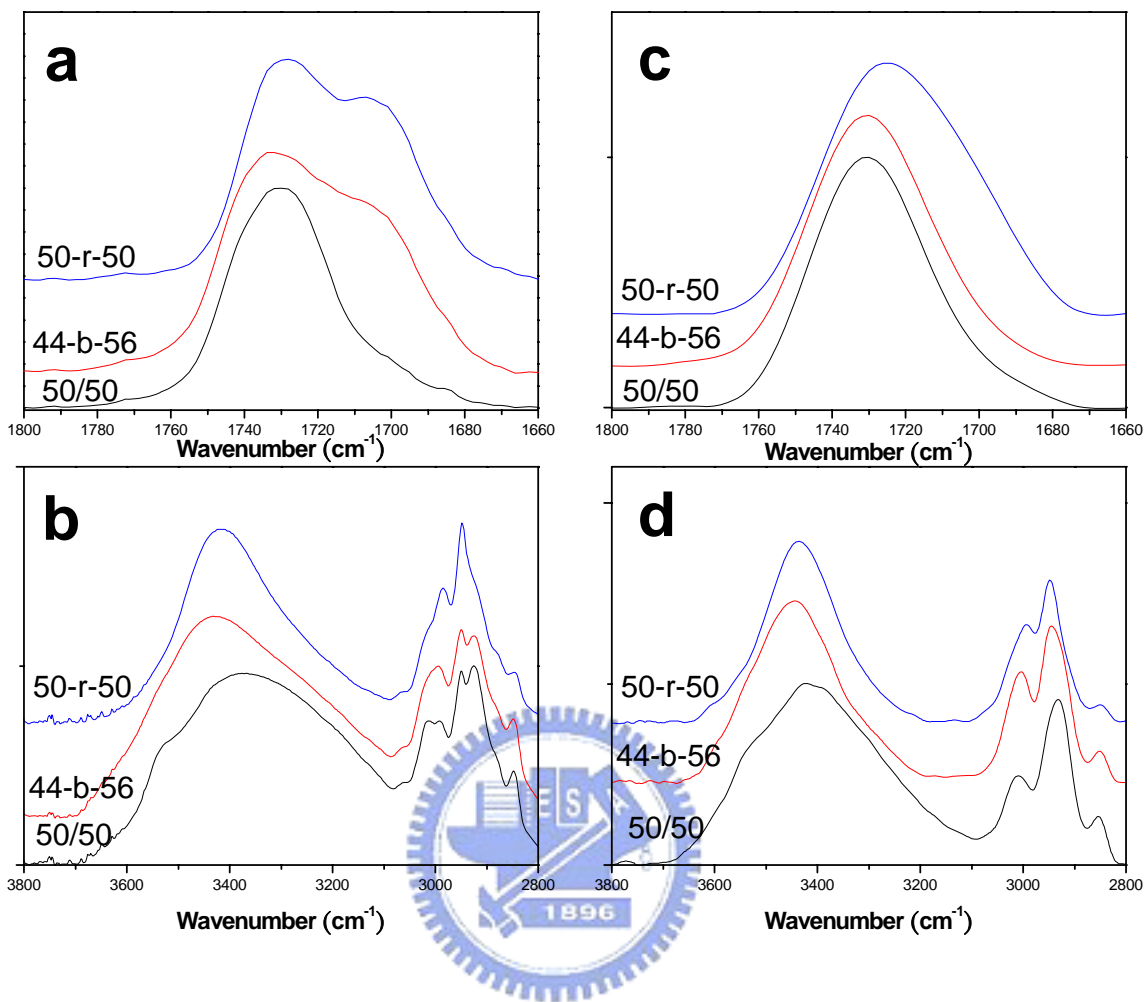


Figure 6-3. The FTIR spectra of samples having similar PVPh contents preparing by different coating process (a) 、(b) solvent casting and (c) 、(d) spin coating.

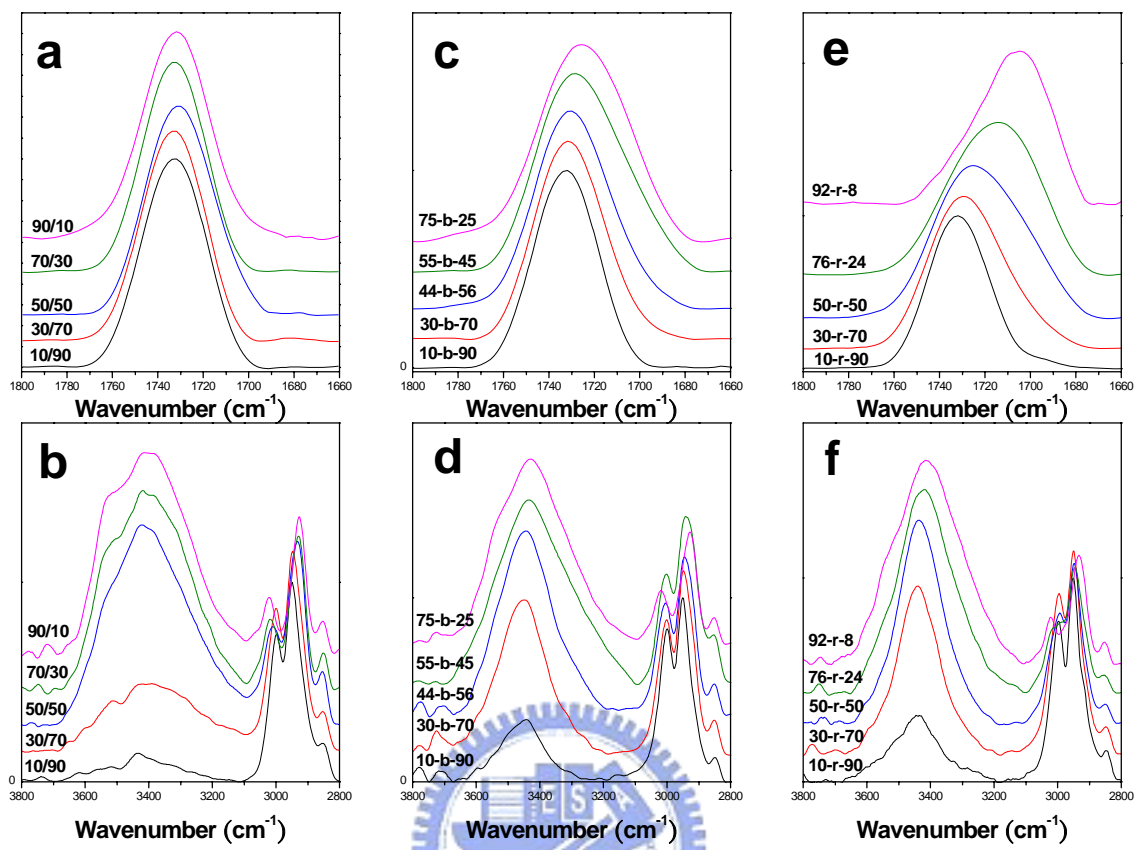


Figure 6-4. FTIR spectra of (a) 、(b) PVPh/PMMA blends, (c) 、(d) PVPh-b-PMMA copolymers and (e) 、(f) PVPh-r-PMMA copolymers at room temperature.

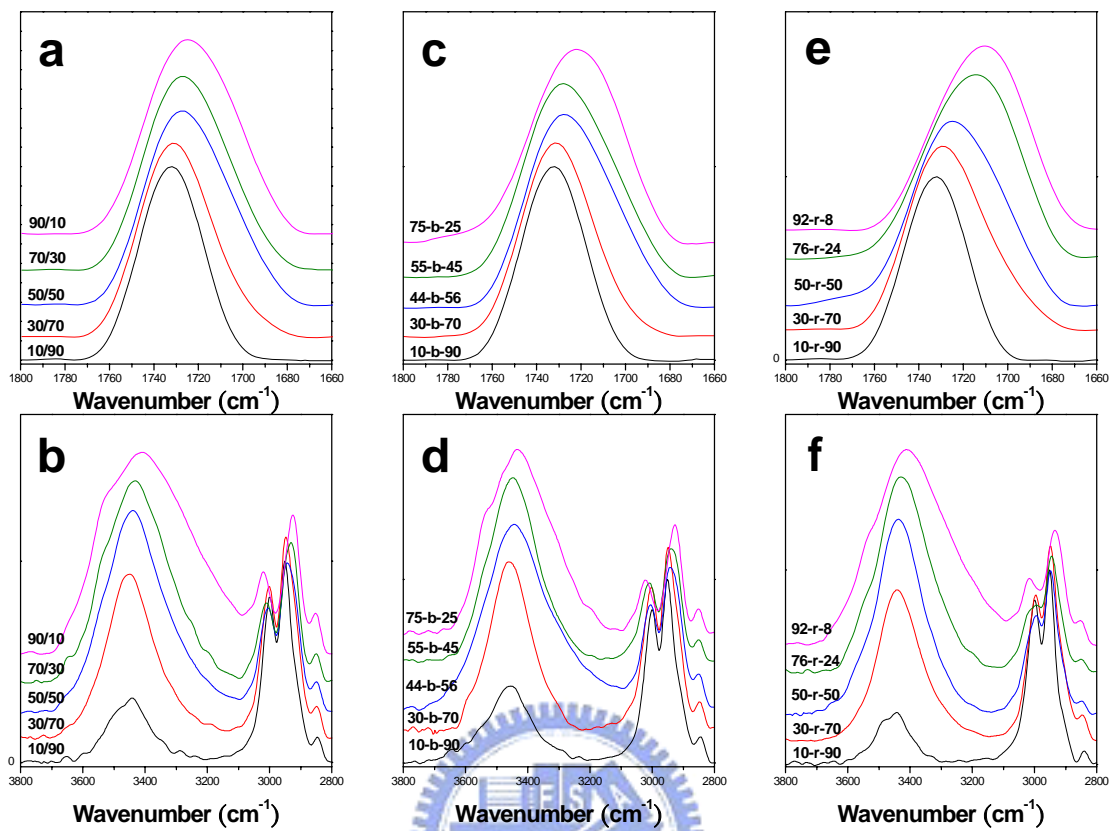


Figure 6-5. FTIR spectra of (a) \ (b) PVPh/PMMA blends, (c) \ (d) PVPh-b-PMMA copolymers and (e) \ (f) PVPh-r-PMMA copolymers after the 180 °C thermal treatment procedure.

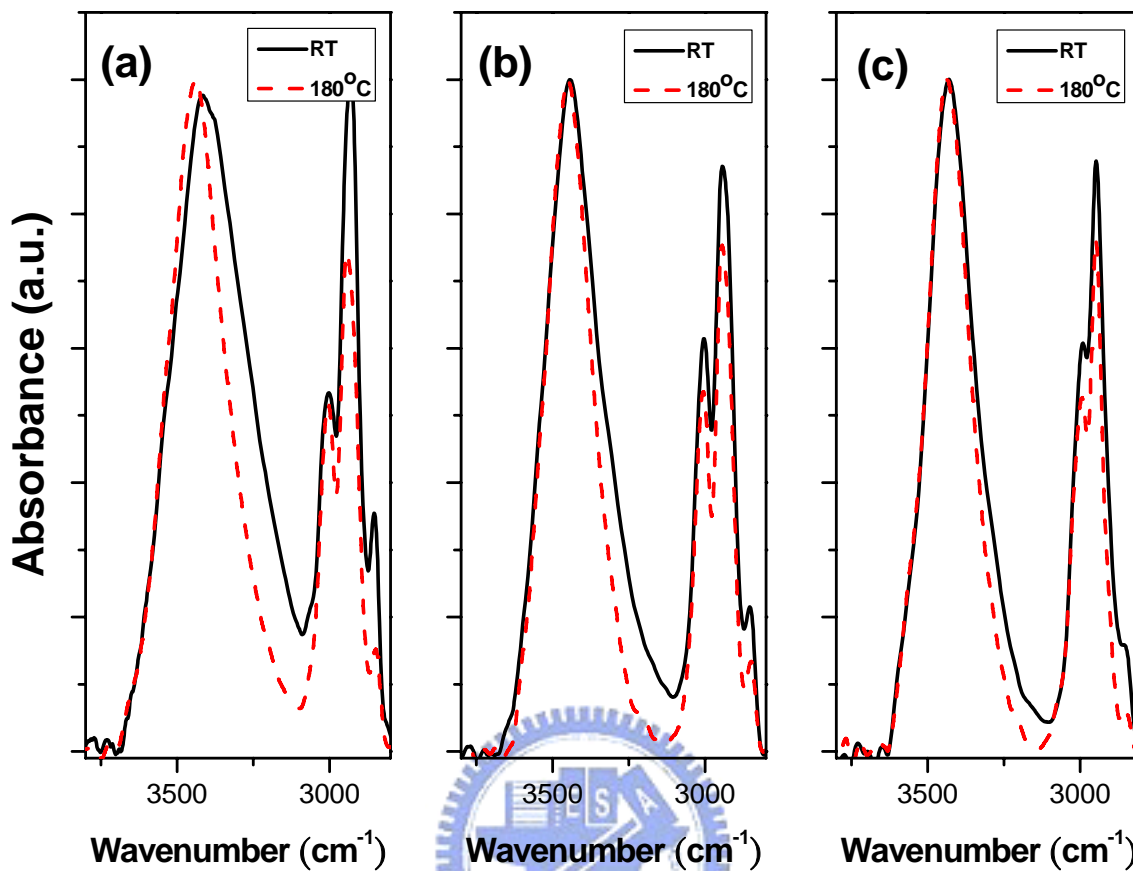


Figure 6-6. FTIR spectra of (a) PVPh/PMMA blends, (b) PVPh-b-PMMA copolymers and (c) PVPh-r-PMMA copolymers in $2800\text{cm}^{-1}\sim 3800\text{cm}^{-1}$.

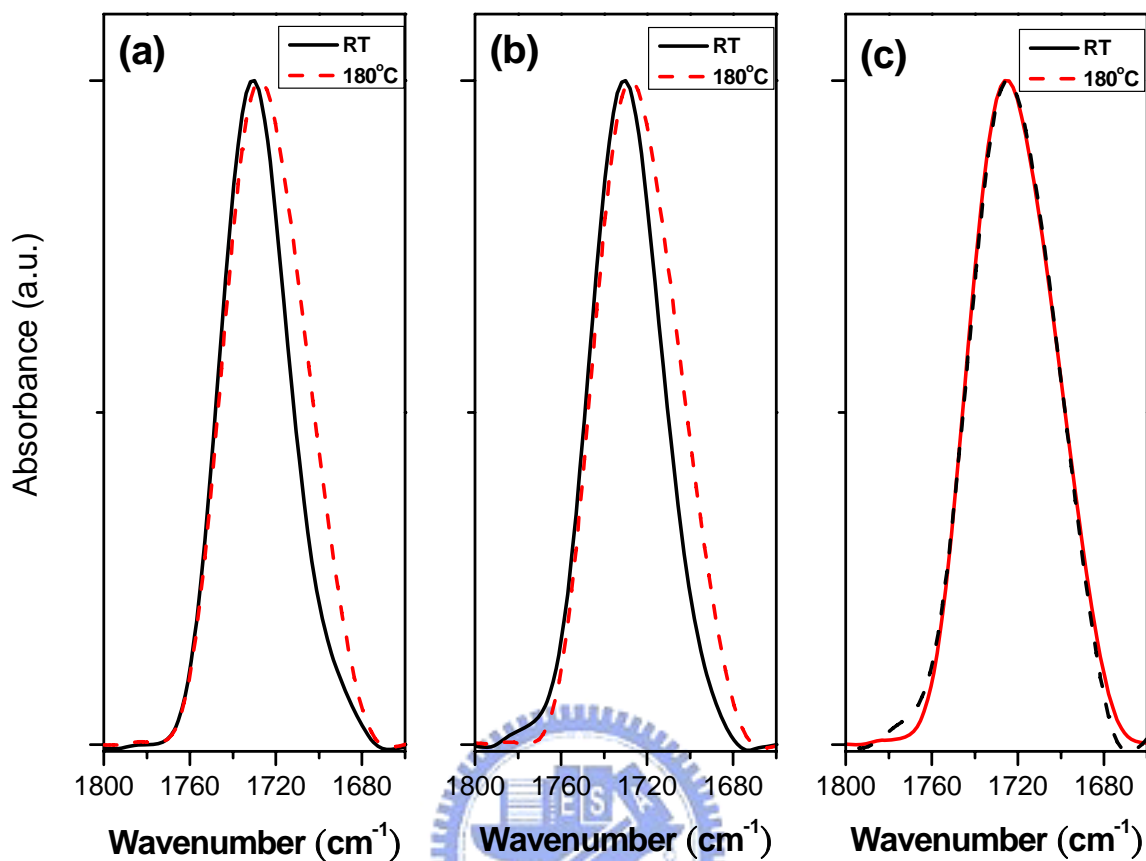


Figure 6-7. FTIR spectra of (a) PVPh/PMMA blends, (b) PVPh-b-PMMA copolymers and (c) PVPh-r-PMMA copolymers 1660cm⁻¹~1800cm⁻¹.

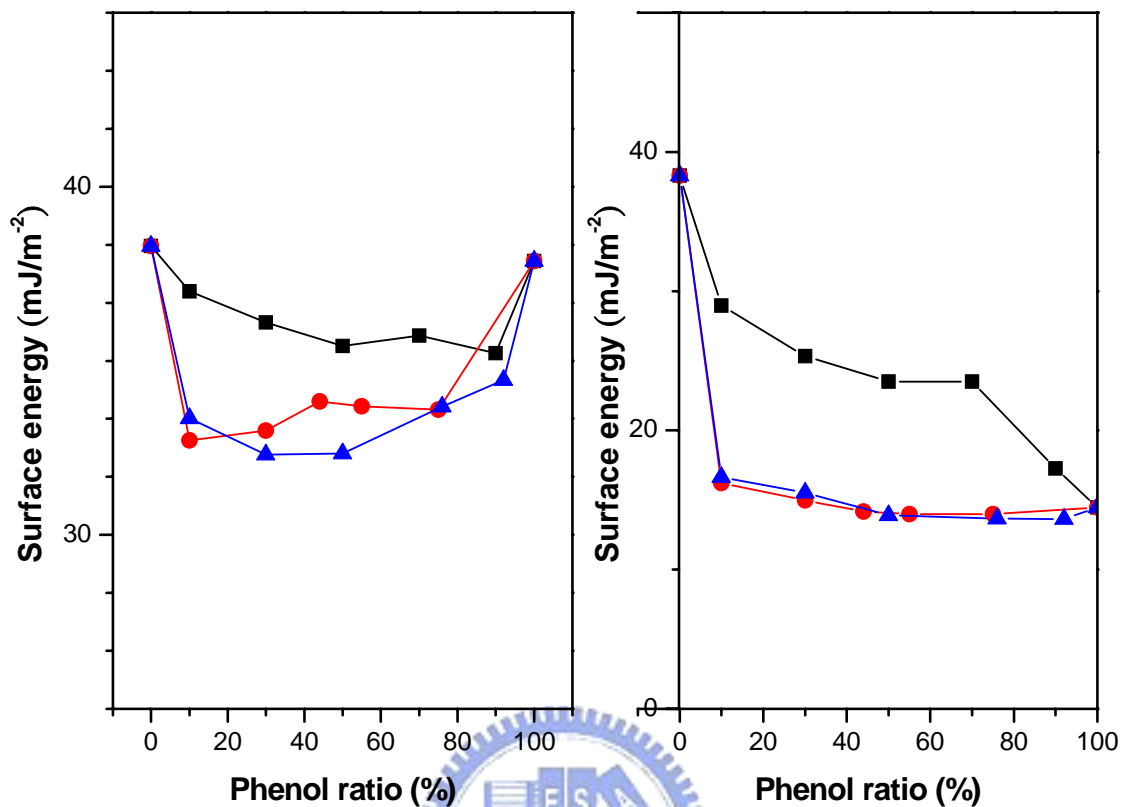


Figure 6-8. Surface energy of PVPh/PMMA random copolymers (▲), block copolymers (●) and their blends (■) (a) before (b) after the thermal treatment process.

Chapter 7

Effect of POSS Nanoparticle on Surface Free Energy and Phase Behavior

Abstract

POSS-PAS copolymer was synthesized by atomic transfer radical polymerization with POSS-Cl initiator as a macroinitiator which was obtained by using corner-capping reaction. POSS-PVPh copolymer was obtained from the hydrolysis of POSS-PAS copolymer. We found that the POSS nanoparticle would decrease the polymer surface free energy in both POSS/PVPh and POSS-PVPh systems. With increasing the content of POSS nanoparticle on polymer thin film surface the surface free energy of polymer thin film would decrease. We also found that the POSS-PVPh copolymers possessed unique phase behavior in solution state and then, the superhydrophobic surface was prepared from POSS-PVPh in a THF/toluene mix solution.

7.1 Introduction

Polymers reinforced with well-defined nanosized inorganic clusters (i.e., polymeric nanocomposites) have attracted a tremendous degree of interest because of their potential applications. Among these systems, polyhedral oligomeric silsesquioxanes (POSSs) compounds, which possess unique cage-like structures and nanoscale dimensions, are of particular interest for use as hybrid materials. POSS compounds embody inorganic/organic hybrid architectures, i.e., they contain an inner inorganic framework composed of silicon and oxygen $(\text{SiO}_{1.5})_x$ and present organic substituents. Because POSS moieties can be readily incorporated into polymer matrices through copolymerization, many types of polymer/POSS nanocomposites have been synthesized. [1–7] In this chapter, PVPh/POSS blends and POSS-PVPh copolymers were prepared to investigate the effect of POSS nanoparticle on surface free energy.

In addition, superhydrophobic materials with a water contact angle (WCA) higher than 150° have attracted great interest in recent years because of their practical applications in water repellency, self-cleaning, and antifouling properties. [8–12] In general, the WCA is based on the water-repellent behavior of the fractal micro-nanometer scale binary structures of the material. Preparation of the rough surface and subsequent coating of the surface with low surface energy materials is an essential process in fabricating superhydrophobic surface. [13, 14] Yabu et al. [15, 16] have reported a microporous honeycomb-patterned film prepared by casting a fluorinated copolymer solution under humid conditions which then exhibits a superhydrophobic surface. In our previous report, [17] we have discovered that honeycomb structures and superhydrophobic surfaces could be prepared simultaneously from poly(vinyl phenol)-block-polystyrene (PVPh-b-PS)

diblock copolymers by carefully controlling the weight composition of the block copolymer and the selective solvent content.

In this chapter, the POSS-poly(vinyl phenol) (POSS-b-PVPh) block copolymer is synthesized by atomic transfer radical polymerization. The block copolymer micelles exhibit superhydrophobic surfaces can be easily formed by the tetrahydrofuran (THF)/toluene mixed solvent.



7.2 Experiment Section

7.2.1 Preparation of PVPh/POSS Block Copolymers and Blends.

The detailed synthesis procedures of PVPh homopolymers have been reported previously. [18] Octakis (dimethylsiloxy) octasilsesquioxane ($Q_8M_8^H$) (Hybrid Plastics) was used without further purification. 0.25g PVPh homopolymer ($M_w = 9697$) was pre-mixed with a certain weight ratio of $Q_8M_8^H$ in 5g tetrahydrofuran (THF) at room temperature. The solution was then filtered through a 0.2 μm syringe filter before spin coating onto a glass slide ($100 \times 100 \times 1 \text{ mm}^3$).

We used the corner-capping reaction to prepare POSS-Cl initiator in which only one corner is functionalized with an atom transfer radical polymerizable group (Scheme 6-1). The initiator, POSS-Cl, was prepared by reacting Trichloro[4-(chloromethyl)phenyl]silane (1.00 mL, 5.61 mmol) with isobutyltrisilanol-POSS (4.05 g, 5.11 mmol) in the presence of triethylamine (2.20 mL, 15 mmol) in 30.0 mL of dry THF under argon. The reaction flask was stirred at room temperature for 7.5 h, followed by filtration to remove the $\text{HNEt}_3\text{-Cl}$ byproduct. The clear THF solution was dropped into a beaker of acetonitrile and rapidly stirred. The resulting product was collected by filtration and dried in a vacuum.

To prepare the POSS-poly (acetoxystyrene) (POSS-PAS) comopolymers, the atom transfer radical polymerization with CuBr/bipyridine was carried out (Scheme 7-1). The length of PAS segment of POSS-PAS was determined by NMR and molecular weight distribution (PDI) was obtained from GPC. POSS-poly (4-vinylphenol) (POSS-PVPh) copolymers were obtained from the hydrolysis of POSS-PAS copolymers. Removal of the acetyl protecting groups from the AS polymers was carried out in 1, 4-dioxane by

treating it with hydrazine hydrate at room temperature. Typically, a block copolymer POSS-b-PAS (7.2 mmol of AS) was added in a flask and solubilized with 1, 4-dioxane (30 mL). Then, hydrazine hydrate (3 ml) was added via a syringe and the ratio of hydrazine hydrate to 1, 4-dioxane was 1:9 by volume. The reaction was allowed to proceed at room temperature under nitrogen for approximately 10 h. The solution was concentrated by evaporation of the solvent and washed with deionized water several times, followed by drying in a vacuum oven at room temperature for 2 days.



7.3 Characterizations

¹H NMR spectra were recorded on a Varian Unity Inova 500 FT NMR spectrometer operated at 500 MHz; deuterated chloroform was used as the solvent. Infrared spectroscopic measurements were conducted on a Nicolet Avatar 320 FTIR spectrophotometer; 32 scans were collected with a spectral resolution of 1 cm⁻¹. All sample preparations were under continuous nitrogen flow to ensure minimal sample oxidation or degradation. Surface roughness profiles of film structures were acquired using a Digital Instruments DI5000 scanning probe microscope in the tapping mode. The values of root-mean-square (rms) roughness were calculated over scan areas of 5 μm × 5 μm. For contact angle measurements, deionized water and diiodomethane (DIM) were chosen as testing liquids because significant amounts of data are available for these liquids. The advancing contact angle measurement of a polymer sample was determined at 25 °C after injection of a liquid drop (5 μL) onto the surface, and a Krüss GH-100 goniometer interfaced to image-capture software was employed to perform the measurement. A two-liquid geometric method was employed to determine the surface energy. [19] Transmission electron microscopy (TEM) images were obtained on a Hitachi H-7500 Electron Microscope operating at 100 kV. A drop of the very dilute solution was placed onto a carbon-coated TEM copper grid. After 3 min, excess solution was blotted away using a strip of filter paper. The samples were allowed to dry in atmosphere at room temperature and then stained with ruthenium tetroxide (RuO₄) for 30 min and air-dried before measurement.

7.4 Results and Discussion

7.4.1 The effect of POSS nanoparticle on surface free energy in PVPh system

In this chapter, PVPh/POSS blends and POSS-PVPh copolymers were prepared to investigate the effect of POSS nanoparticle on surface free energy.

POSS-poly (acetoxystyrene) (POSS-PAS) copolymers were synthesized by the atom transfer radical polymerization with CuBr/bipyridine (Scheme 7-1). The POSS-PAS copolymers were characterized by ^1H NMR and gel permeation chromatography (GPC). The average number of PVPh segment was calculated by ^1H NMR integration (Table 6-2). POSS-poly (4-vinylphenol) (POSS-PVPh) copolymers were obtained from the hydrolysis of POSS-PAS copolymers. The structure of the T7-POSS, POSS-Cl, POSS-PAS copolymer and POSS-PVPh copolymer are confirmed from their FT-IR spectra (Figure 6-1) and ^1H NMR spectra (Figure 6-2).

FT-IR (KBr): 3525 cm^{-1} (free OH), 3350 cm^{-1} (hydrogen bonded OH), 2957 cm^{-1} (CH_2 stretching), 1603 cm^{-1} (in-plane aromatic C–C stretching), $1000\text{--}1200\text{ cm}^{-1}$ (Si–O–Si asymmetric stretching), $2850\text{--}3000\text{ cm}^{-1}$ (Si- CH_2 rocking), $450\text{--}500\text{ cm}^{-1}$ (Si-O-Si bending), 1765 cm^{-1} (C=O stretching) (Figure 6-1),

^1H NMR (500 MHz): $\delta = 6.0\text{--}7.0\text{ ppm}$ (4H, aromatic CH), $\delta = 7.37\text{ ppm}$ (H, –OH), $\delta = 0.55\text{ ppm}$ (2H, $\text{SiCH}_2\text{CH}(\text{CH}_3)_2$), $\delta = 0.91\text{ ppm}$ (6H, $\text{SiCH}_2\text{CH}(\text{CH}_3)_2$) and $\delta = 2.41\text{ ppm}$ (3H, OCOCH_3) (Figure 6-2).

From Table 6-1 and 6-2, we can observe that the surface free energy increases with increasing of POSS content in both POSS-PVPh copolymers and POSS/PVPh blends. It was reported recently that the POSS units in related nanostructures prefer to be oriented toward the air-side, an arrangement that screens out the polar groups (e.g., urethane and

carboxyl units). [20, 21] We anticipated that the POSS moieties in our POSS-PVPh copolymers and POSS/PVPh blends were also oriented toward the air-side to form an inorganic protection layer on the surface of each polymer thin films. To provide evidence in support of this hypothesis, we performed contact angle measurements and XPS analyses to investigate the surface behavior of each polymer thin films.

Table 6-2 and 6-3 list the XPS results and we observed that the atomic percentage of silicon increased dramatically upon increasing the POSS content. Thus, both the contact angle measurements and the XPS results indicate that the POSS moieties were distributed preferably on the surface of the polymer thin film.

7.4.2 The effect of POSS nanoparticle on phase behavior in POSS-PVPh copolymer

Micellization of amphiphilic block copolymers in the solution state is well documented in scientific literature owing to its potential in various applications, such as drug delivery and stimuli-responsive functional materials of nanodevices. [22–25] Amphiphilic block copolymers can self-assemble in solution to form micelles with various morphologies, including spheres, cylinders, vesicles, wormlike, helical, large compound micelles (LCMs), and many others. [26–33] Micelles of block copolymers, which have a long corona and small core, are termed as “starlike”, while the ones with a large core and short corona are termed as “crew-cut”. [34] Generally, starlike micelles present as spherical micelles due to their long corona chain; on the contrary, crew-cut micelles could show a wide range of morphologies. [35, 36] Parameters to control the morphology of the self-assembled micelles can be divided into two categories: molecular and solution parameters. First, the molecular parameters include the copolymer

composition, the chemical characteristics of repeating units, the overall molecular weight, and the molecular structure. In the past decade, manipulating these parameters has been proven to be efficient way of tuning the micelle morphologies. [37, 38] The second category, which has been investigated only recently, includes the type of solvent [39] and solvent quality, the solvent/nonsolvent ratio, [40] the copolymer concentration, the pH value, additives such as salts, ions, and homopolymer, and the temperature. The morphology is mainly controlled by a force balance involving three factors: the core-chain stretching, the interfacial energy between the core and outside solvent, and the repulsion among the corona chains. The morphogenic effects of the abovementioned parameters can, in general, be ascribed to their influence on this force balance during the formation of micelles.

To our knowledge, although micellization of amphiphilic block copolymers in the solution state have been widely discussed, the aggregation behavior of polymers with POSS in the chain end have received less attention. Frey et al. [41] have reported that POSS-poly(ethylene oxide) would self-assemble to micellar and vesicular structures in solution state and an increase of the pH was employed to crosslink the self-assembled structures to spherical vesicles with a silica shell. In addition, He et al. [42] have reported that amphiphilic multiarm CSSQ-PEO would form a core-corona structure of unimolecular and aggregated CSSQ-PEO in aqueous solution. In this chapter, we find POSS-PVPh copolymers also possess unique aggregation behavior in solution state. From Figure 7-3, we find the morphology of POSS-PVPh copolymers in acetonitrile solution changes from sphere to cylinder with the decreasing of PVPh chain length. In addition, the morphologies of POSS-PVPh₁₂₀ in toluene/THF mix solution change from

sphere to vesicle with the increasing of toluene content (Figure 7-4). This phenomenon could be explained that POSS-PVPh copolymers tended to decrease the interfacial energy in solution state which produced from the insoluble segment of POSS-PVPh (eg. acetonitrile is nonsolvent for POSS nanoparticle and toluene is non solvent for PVPh) and solvent. In addition to the change of morphology, we find POSS-PVPh₁₂₀ will not aggregate to form LCMs in acetonitrile solution although the polymer concentration is high (Figure 7-5). Furthermore, a superhydrophobic surface can be obtained from casting a THF/toluene = 5:1 (v/v) mix solution. Figure 7-6 shows the SEM image and corresponding water contact angle of superhydrophobic surface which is prepared from POSS-PVPh₁₂₀ copolymer.



7.5 Conclusions

A novel POSS-PAS copolymer was synthesized by atomic transfer radical polymerization. POSS-PVPh copolymer was obtained from the hydrolysis of POSS-PAS copolymer. The POSS nanoparticle would decrease the polymer surface free energy in both POSS/PVPh and POSS-PVPh systems. With increasing the content of POSS nanoparticle on polymer thin film surface the surface free energy of polymer thin film would decrease. We also found that the POSS-PVPh copolymers possessed unique phase behavior in solution state. Furthermore, the superhydrophobic surface was prepared from POSS-PVPh in a THF/toluene mix solution.

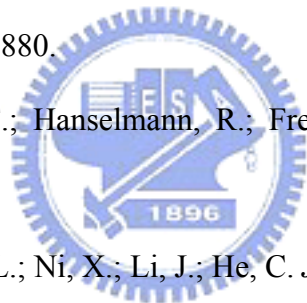


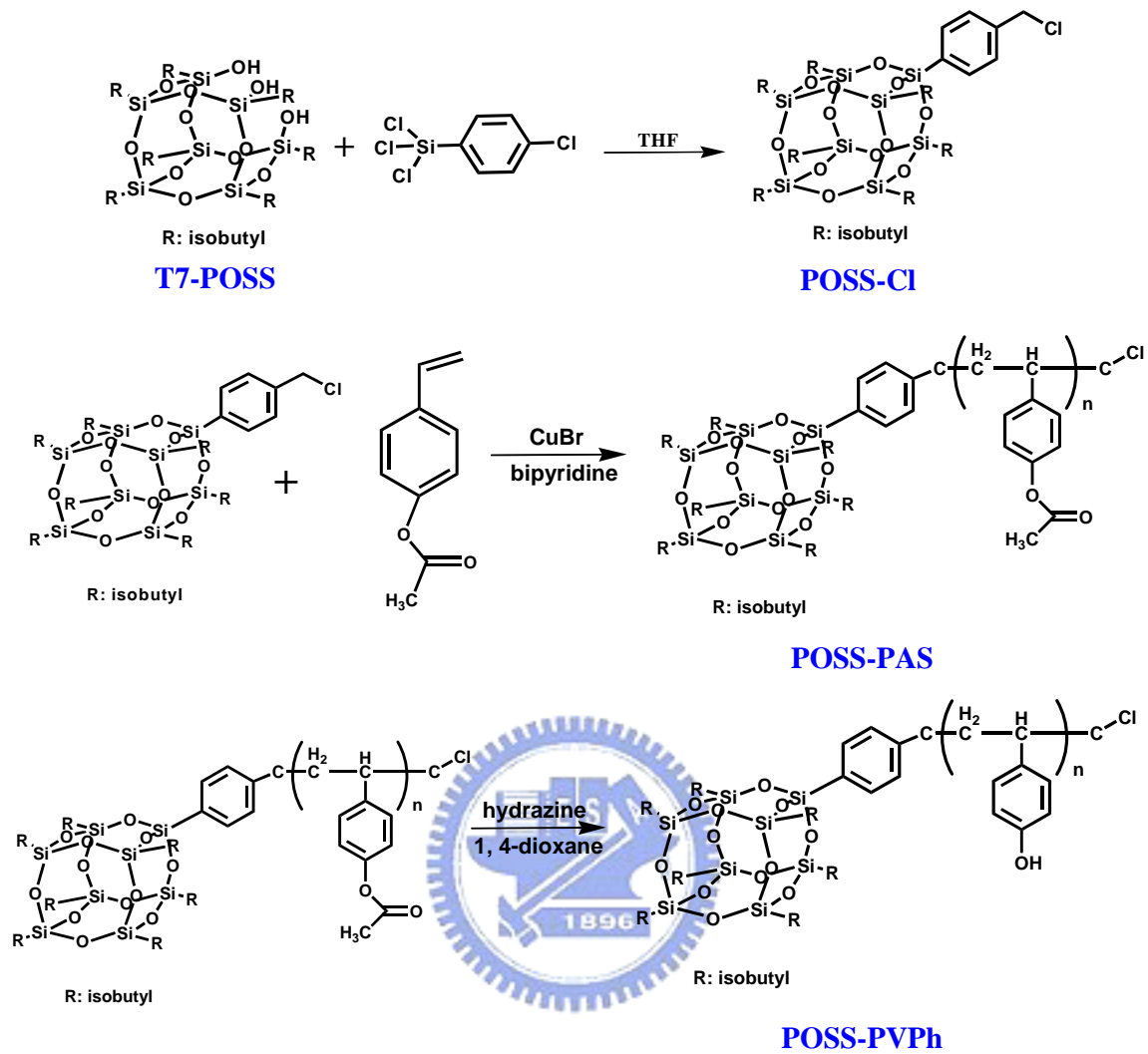
References

- [1] T. S. Haddad, J. D. Lichtenhan, *Macromolecules* **1996**, 29, 7302.
- [2] M. J. Abad, L. Barral, D. P. Fasce, R. J. J. Williams, *Macromolecules* **2003**, 36, 3128.
- [3] Y. Liu, F. Meng, S. Zheng, *Macromol. Rapid Commun.* **2005**, 26, 926.
- [4] H. Li, S. Zheng, *Macromol. Rapid Commun.* **2005**, 26, 196.
- [5] C. M. Leu, Y. T. Chang, K. H. Wei, *Macromolecules* **2003**, 36, 9122.
- [6] Q. Chen, R. Xu, J. Zheng, D. Yu, *Macromol. Rapid Commun.* **2005**, 26, 1878.
- [7] B. X. Fu, W. Zhang, B. S. Hsiao, G. Johansson, B. B. Sauer, S. Phillips, R. Balnski, M. Rafailovich, J. Sokolov, *Polym. Prepr.* **2000**, 41, 587.
- [8] L. Feng, Y. Song, J. Zhai, B. Liu, J. Xu, L. Jiang, B. Zhu, *Angew. Chem. Int. Ed.* **2003**, 42, 800.
- [9] J. Zhang, Y. Lu, W. Huang, Y. Han, *Macromol. Rapid Commun.* **2005**, 26, 477.
- [10] K. Tsujii, T. Yamamoto, T. Onda, S. Shibuichi, *Angew. Chem. Int. Ed.* **1997**, 36, 1011.
- [11] J. P. Youngblood, T. J. McCarthy, *Macromolecules* **1999**, 32, 6800.
- [12] N. Zhao, J. Xu, Q. Xie, L. Weng, X. Guo, X. Zhang, L. Shi, *Macromol. Rapid Commun.* **2005**, 26, 1075.
- [13] L. Feng, S. Li, H. Li, J. Zhai, Y. Song, L. Jiang, D. Zhu, *Angew. Chem. Int. Ed.* **2002**, 41, 1221.
- [14] M. Ma, Y. Mao, M. Gupta, K. K. Gleason, G. C. Rutledge, *Macromolecules* **2005**, 38, 9742.
- [15] H. Yabu, M. Shimomura, *Chem. Mater.* **2005**, 17, 5231.
- [16] H. Yabu, M. Takebayashi, M. Tanaka, M. Shimomura, *Langmuir* **2005**, 21, 3235.

- [17] Tung, P. H.; Kuo, S. W.; Jeong, K. U.; Cheng, S. Z. D.; Huang, C. F.; Chang, F. C. *Macromol. Rapid Commun.* **2007**, *28*, 271.
- [18] Lin, C. L.; Chen, W. C.; Liao, C. S.; Su, Y. C.; Huang, C. F.; Kuo, S. W.; Chang, F. C. *Macromolecules* **2005**, *38*, 6435.
- [19] Fowkes, F. W. In *Adhesion and Adsorption of Polymers, Polymer Science and Technology*; Lee, L. H., Ed.; Plenum Press: New York, **1980**; Vol. 12A, p 43.
- [20] Turri, S.; Levi, M. *Macromolecules* **2005**, *38*, 5569.
- [21] Turri, S.; Levi, M. *Macromol. Rapid Commun.* **2005**, *26*, 1233.
- [22] Gil, E. S.; Hudson, S. A. *Prog. Polym. Sci.* **2004**, *29*, 1173.
- [23] Rodriguez-Hernandez, J.; Checot, F.; Gnanou, Y.; Lecommandoux, S. *Prog. Polym. Sci.* **2005**, *30*, 691.
- [24] Harada, A.; Kataoka, K. *Prog. Polym. Sci.* **2006**, *31*, 949.
- [25] Zhao, Q.; Ni, P. H. *Prog. Chem.* **2006**, *18*, 768.
- [26] Van Hest, J. C. M.; Delnoye, D. A. P.; Baars, M. W. P. L.; Van Genderen, M. H. P.; Meijer, E. W. *Science* **1995**, *268*, 1592.
- [27] Zhang, L.; Eisenberg, A. *Science* **1995**, *268*, 1728.
- [28] Ding, J.; Liu, G. *Macromolecules* **1997**, *30*, 655.
- [29] Chan, S. C.; Kuo, S. W.; Lu, C. H.; Fee, H. F.; Chang, F. C. *Polymer* **2007**, *48*, 5059.
- [30] Discher, B. M.; Won, Y. Y.; Ege, D. S.; Lee, J. C. M.; Bates, F. S.; Discher, D. E.; Hammer, D. A. *Science* **1999**, *284*, 1143.
- [31] Tung, P. H.; Kuo, S. W.; Chen, S. C.; Lin, C. L.; Chang, F. C. *Polymer* **2007**, *48*, 3192.

- [32] Antonietti, M.; Förster, S. *Adv. Mater.* **2003**, *15*, 1323.
- [33] Jain, S.; Bates, F. S. *Science* **2003**, *300*, 460.
- [34] Halperin, A.; Tirrel, M.; Lodge, T. P. *Adv. Polym. Sci.* **1992**, *100*, 31.
- [35] Zhang, L.; Eisenberg, A. *J. Am. Chem. Soc.* **1996**, *118*, 3168.
- [36] Riegel, I. C.; Eisenberg, A. *Langmuir* **2002**, *18*, 3358.
- [37] Chouchair, A.; Eisenberg, A. *Eur. Phys. J. E* **2003**, *10*, 37.
- [38] Chen, E.; Xia, Y.; Graham, M. J.; Foster, M. D.; Mi, Y.; Wu, W.; Cheng, S. Z. D. *Chem. Mater.* **2003**, *15*, 2129.
- [39] Riegel, I. C.; Samios, D.; Petzhold, C. L.; Eisenberg, A. *Polymer* **2003**, *44*, 2117.
- [40] Bhargava, P.; Zheng, J. X.; Li, P.; Quirk, R. P.; Harris, F. W.; Cheng, S. Z. D. *Macromolecules* **2006**, *39*, 4880.
- [41] Knischka, R.; Dietsche, F.; Hanselmann, R.; Frey, H.; Mülhaupt, R.; Lutz P. J. *Langmuir* **1999**, *15*, 4752.
- [42] Mya, K. Y.; Li, X.; Chen, L.; Ni, X.; Li, J.; He, C. *J. Phys. Chem. B* **2005**, *109*, 9455





Scheme 7-1. Procedure of Synthesis of POSS-poly (4-vinyl phenol) copolymer.

Table 5-1. Characterization, root-mean-square surface roughness, advancing contact angle for water and diiodomethane and surface Free energy of POSS-PVPh Copolymers

copolymer	The length of PVPh segment ^a	M_w/M_n^b	Roughness (nm)	Contact angle (deg)		γ (mJ/m ²)	ESCA silicon content (mol%)
				H ₂ O	DIM		
POSS-PVPh ₉	9	1.19					
POSS-PVPh ₃₅	35	1.41	1.05	111.5	68.93	24.60	15.52
POSS-PVPh ₁₂₀	120	1.38	1.26	110.9	68.74	24.62	8.79
POSS-PVPh ₂₆₄	264	1.33	1.06	109.8	67.8	25.06	7.92



Table 5-2. Root-mean-square surface roughness, advancing contact angle for water and diiodomethane and surface Free energy of POSS/PVPh Blends.

Blends	The weight ratio of POSS/PVPh (%)	Roughness (nm)	Contact angle (deg)		γ (mJ/m ²)	ESCA silicon content (mol%)
			H ₂ O	DIM		
POSS/PVPh =1/100	1%		92.6	69.1	24.2	13.54
POSS/PVPh =3/100	3%	1.85	100.6	79.7	18.1	15.04
POSS/PVPh =5/100	5%	1.64	105.5	81.4	16.9	17.14
POSS/PVPh =10/100	10%	1.68	109.9	84.6	15.2	22.01
POSS/PVPh =20/100	20%	1.68	116.6	86.4	14.6	34.85



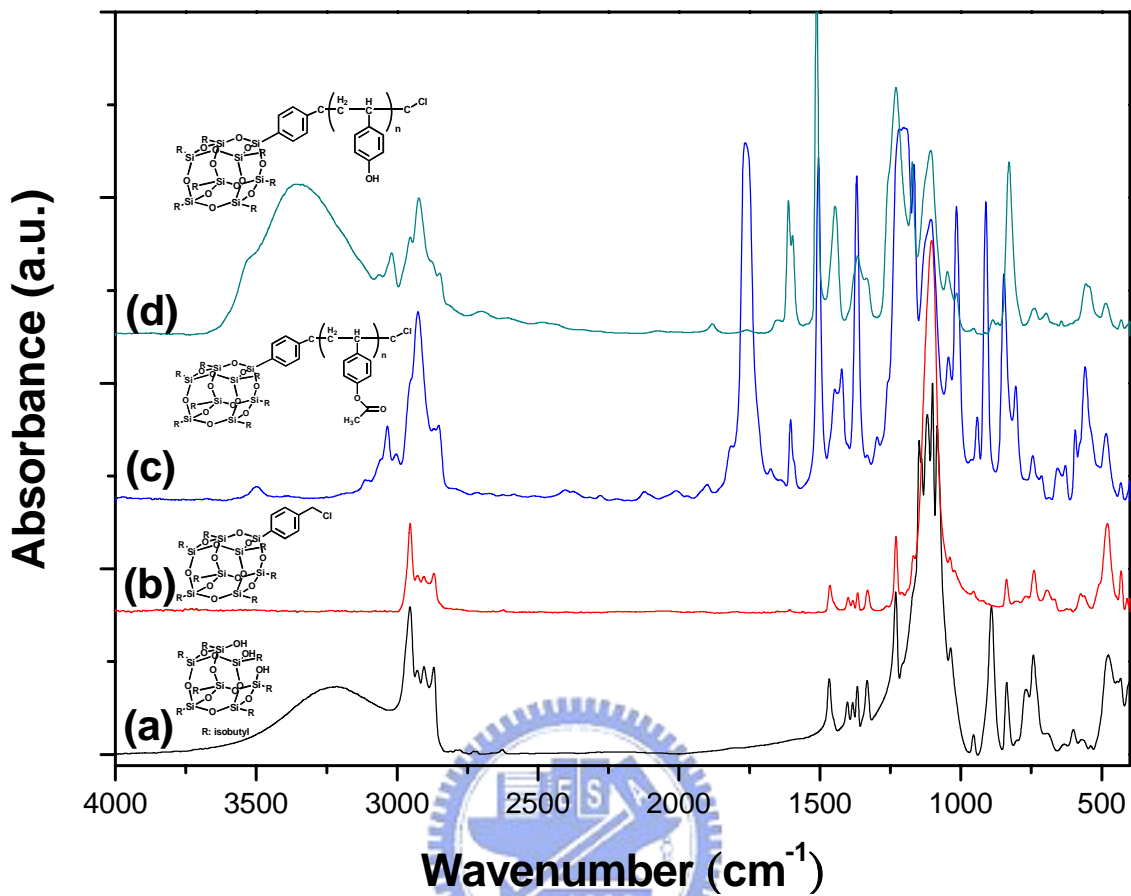


Figure 7-1. Chemical structures and FT-IR spectra of (a)T7-POSS, (b)POSS-Cl, (c)POSS-PAS copolymer and (d) POSS-PVPh copolymer.

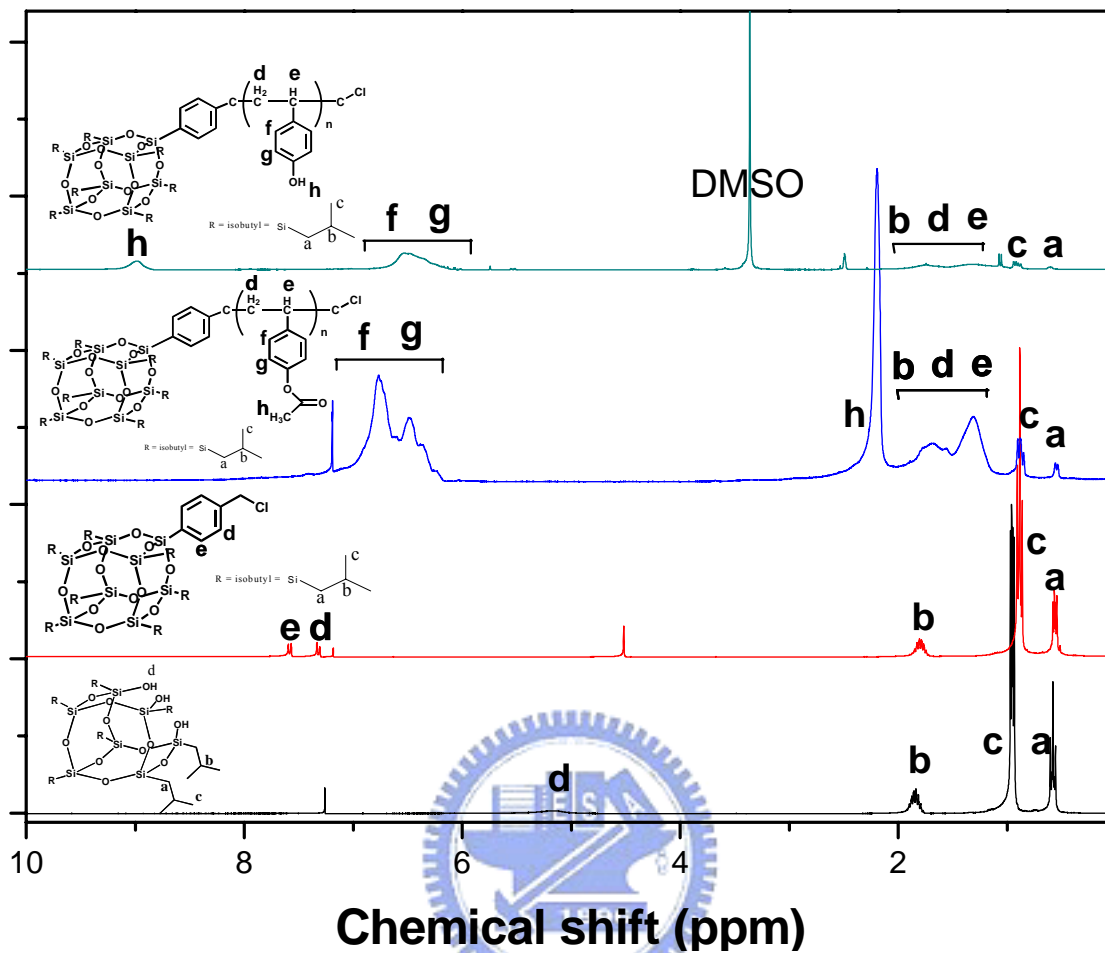


Figure 7-2. ¹H NMR spectra of (a) T7-POSS, (b) POSS-Cl, (c) POSS-PAS copolymer and (d) POSS-PVPh copolymer.

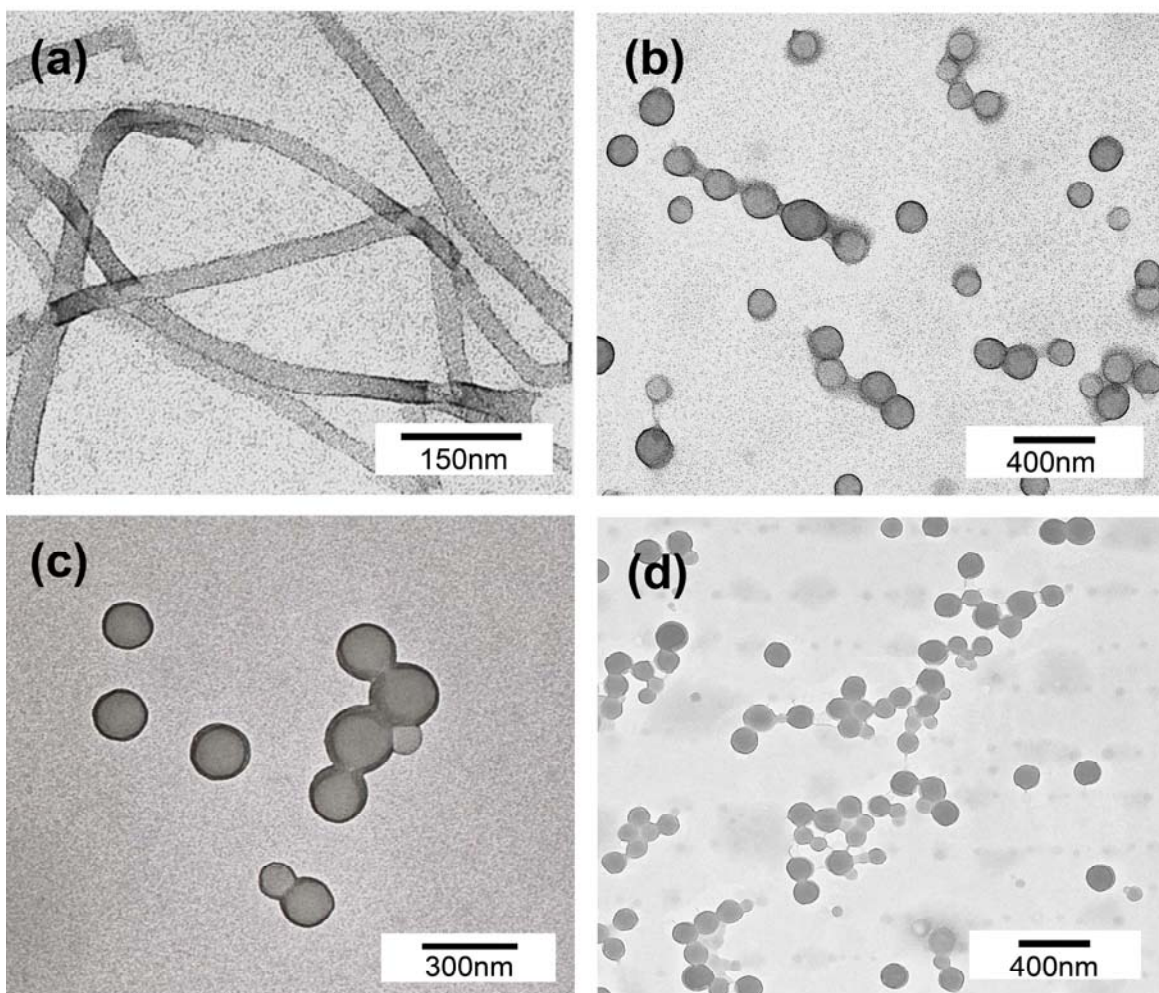


Figure 7-3. Transmission electron micrographs of POSS-PVPh in acetonitrile solution (a) POSS-PVPh₉, (b) POSS-PVPh₃₅, (c) POSS-PVPh₁₂₀ and (d) POSS-PVPh₂₆₄.

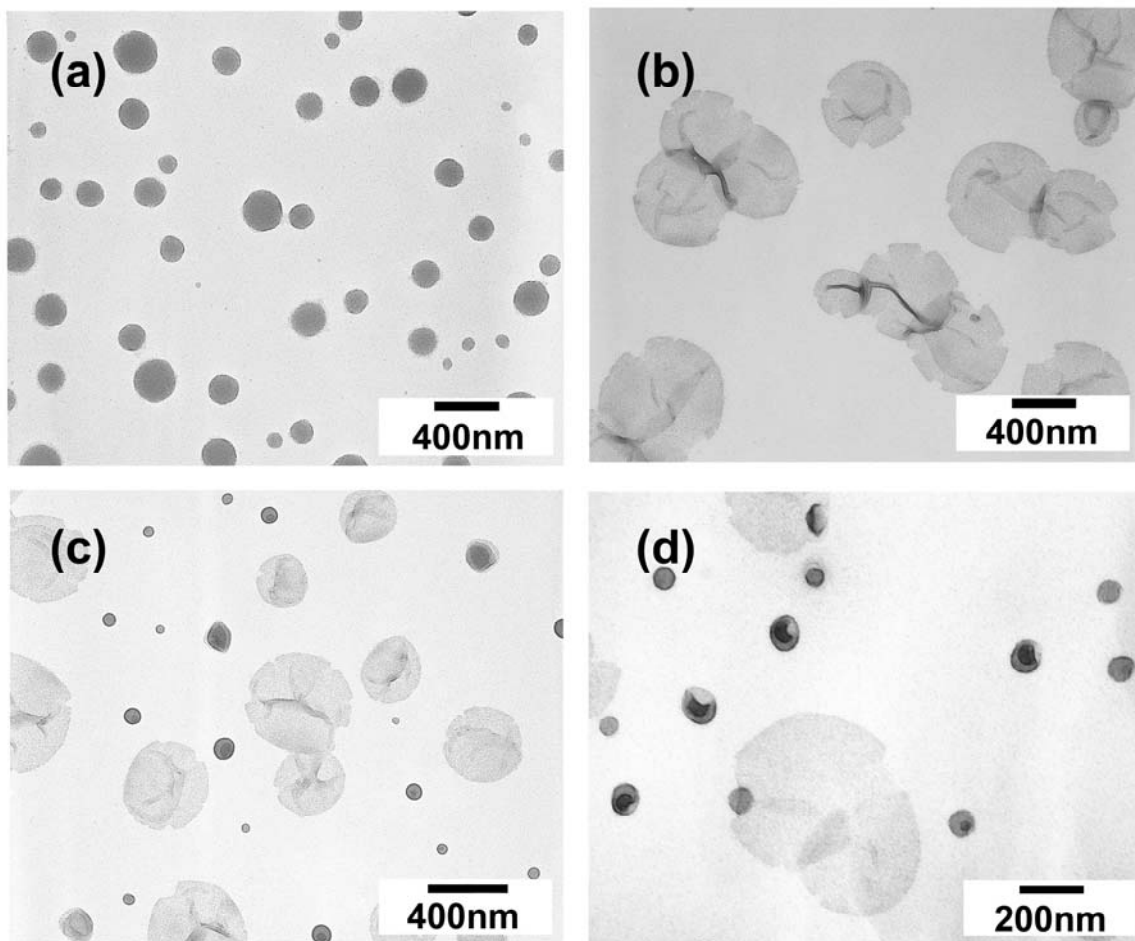


Figure 7-4. Transmission electron micrographs of POSS-PVPh₁₂₀ in different solution (a) 0.1ml toluene + 4.0ml THF, (b) 0.5ml toluene + 4.0ml THF, (c) 1ml toluene + 4.0ml THF and (d) 2ml toluene + 4.0ml THF.

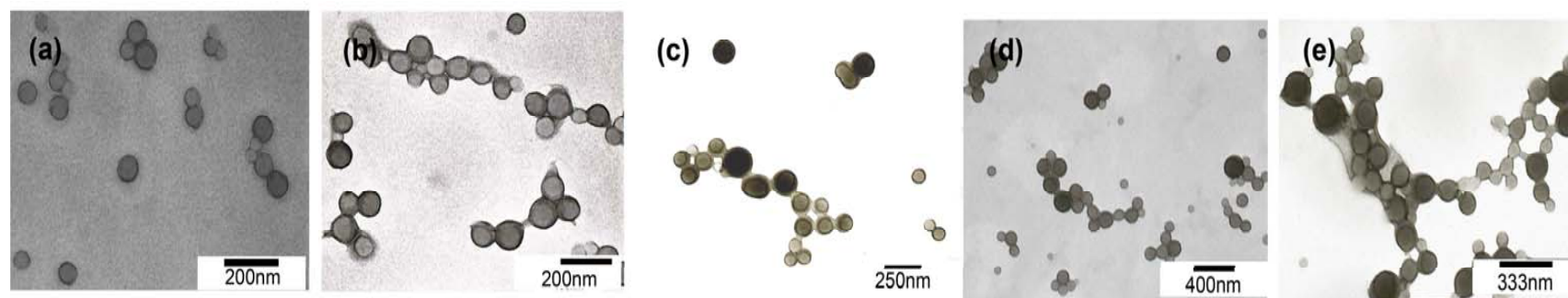


Figure 7-5. Transmission electron micrographs of POSS-PVPh₁₂₀ in acetonitrile at different concentrations:(a) 0.5 mg/mL, (b) 1.0 mg/mL, (c) 2.0 mg/mL, (d) 4.0 mg/mL and (e) 8.0 mg/ml.



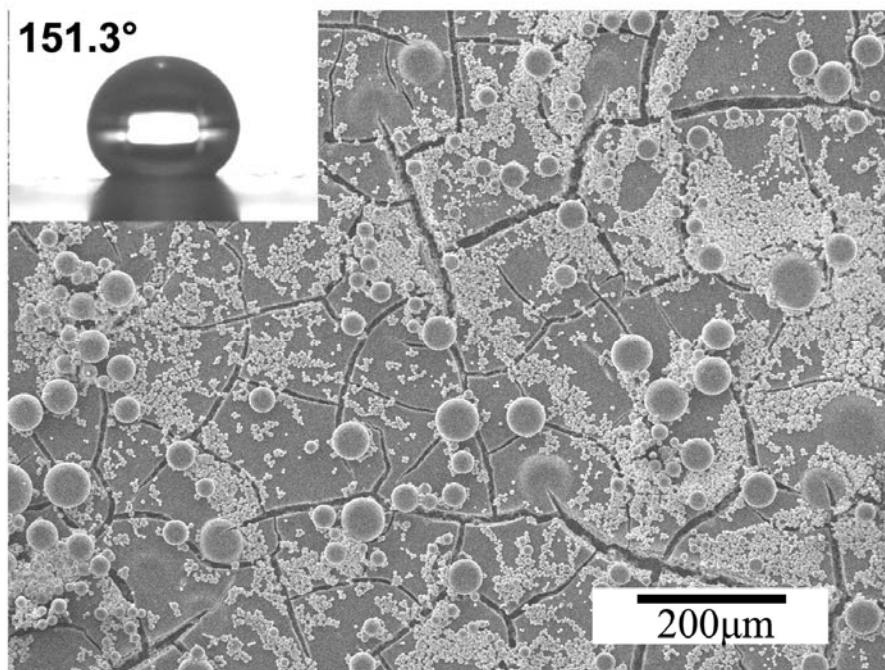


Figure 7-6. SEM image and corresponding water contact angle of POSS-PVPh superhydrophobic surface.



Chapter 8

Conclusions

The free radical initiator, AIBN, induced polymerization of the *N*-allyl group and produced phenol-containing oligomers. These oligomers were able to catalyze the ring opening of the oxazine ring at a relatively lower curing temperature (120°C) to produce polybenzoxazine with stronger intramolecular hydrogen bonding but lower surface energy. B-ala and B-ala/AIBN PBZ thin films both possessed low surface free energy because the strong intramolecular hydrogen bonds were formed during the curing process. B-ala/AIBN PBZ system had a relatively lower surface free energy than the pure B-ala system because of the higher extent of the ring-opening of oxazine. Moreover, it can modify many polymer substrates that are thermally stable at or above 120°C.

The surface free energy and hydrophilicity of PBZ films can be controlled through a combination of thermal treatment and UV exposure to change the ratios of intra- to intermolecular hydrogen bonds. This UV approach provides a simple method to generate wettability patterns or wettability gradients on the surface of polybenzoxazine film and we applied this technique to the preparation of a large-area periodic array of CdTe colloidal nanocrystals on polybenzoxazine thin films.

The superhydrophobic polybenzoxazine-silica hybrid surface can be prepared by an easy two-step coating process and the hydrophilicity of superhydrophobic polybenzoxazine-silica hybrid surface can also be controlled through UV exposure to change the ratio of intra- to intermolecular hydrogen bonds. Through manipulating the hydrophilicity at selected regions on superhydrophobic polybenzoxazine-hybrid surface by UV exposure, we can create patterned surface with superhydrophobic and superhydrophilic regions. Besides, we have found that the superhydrophobic

polybenzoxazine-silica hybrid surface exhibits good adhesion of water droplets after UV exposure which can be served as a “mechanical hand” to transfer water droplets from a superhydrophobic surface to a hydrophilic one.

In addition to PBZ polymer thin films, we have also discovered that a series of poly(vinylphenol-*co*-methylmethacrylate) (PVPh-*co*-PMMA) block and random copolymers possess extremely low surface energy after a simple thermal treatment procedure, even lower than that of poly(tetrafluoroethylene) (22.0 mJ/m^2) calculated on the basis of the two-liquid geometric method. Besides, the effects of molecule weight and POSS nanoparticle on surface free energy were investigated carefully. The decrease of the intermolecular hydrogen-bonding fraction between hydroxyl groups of PVPh in PVPh/PMMA systems through a simple thermal treatment procedure tends to decrease the surface energy. The sequence distribution of the vinylphenol group in PVPh-*co*-PMMA copolymers plays an important role in dictating the final surface energy after thermal treatment. In addition, we also found that the POSS-PVPh amphiphilic copolymers possess unique phase behavior in solution state and a superhydrophobic surface can be carried out by a simple casting process.

List of Publications

1. Chen-Lung Lin, Wan-Chun Chen, Chun-Syong Liao, Yi-Che Su, Chih-Feng Huang, Shiao-Wei Kuo and Feng-Chih Chang “**Sequence Distribution and Polydispersity Index Affect the Hydrogen-Bonding Strength of Poly(vinylphenol-co-methylmethacrylate) Copolymers**” *Macromolecules* 2005, 38, 6435.
2. Chun-Syong Liao, Jiann-Shing Wu, Chih-Feng Wang, and Feng-Chih Chang, “**Modification of Polymer Substrates with Low Surface Free Energy Material by Low-Temperature Cured Polybenzoxazine**” *Macromol. Rapid Commun.* **2008**, 29, 52.
3. Chih-Hao Hsu, Shiao-Wei Kuo, Jem-Kun Chen, Fu-Hsiang Ko, Chun-Syong Liao and Feng-Chih Chang “**Self-Assembly Behavior of A-B Diblock and C-D Random Copolymer Mixtures in the Solution State through Mediated Hydrogen Bonding**” *Langmuir* 2008, 24, 7727.
4. Yuung-Ching Sheen, Yuan-Chang Huang, Chun-Syong Liao, Hsin-Yi Chou and Feng-Chih Chang “**New Approach to Fabricate an Extremely Super-amphiphobic Surface Based on Fluorinated Silica Nanoparticles**” *Journal of Polymer Science: Part B: Polymer Physics* **2008**, 46, 1984.
5. Chun-Syong Liao, Chih-Feng Wang, Han-Ching Lin, Hsin-Yi Chou and Feng-Chih Chang “**Tuning the Surface Free Energy of Polybenzoxazine Thin Films**” *J. Phys. Chem. C* **2008**, 112, 16189.
6. Shih-Chien Chen, Shiao-Wei Kuo, Chun-Syong Liao and Feng-Chih Chang, “**Syntheses, Specific Interactions, and pH-Sensitive Micellization Behavior of Poly[vinylphenol-*b*-2-(dimethylamino)ethyl methacrylate] Diblock Copolymers**” *Macromolecules*, **2008**, 41 (22), 8865–8876

7. **Chun-Syong Liao**, Chih-Feng Wang, Han-Ching Lin, Hsin-Yi Chou and Feng-Chih Chang “**Fabrication of patterned superhydrophobic Polybenzoxazine-hybrid surfaces**” *Langmuir* 2009, in press



Author's Curriculum Vitae

English Name: Chun-Hsiung Liao

Chinese Name: 廖春雄

Birthday: 1981 July 23 (台北)

Address: No.22, Aly. 3, Ln. 81, Yongye Rd., Sindian City, Taipei County 231, Taiwan
(R.O.C.)

Education:

1999.09~2004.06 **B.S.**, Department of Chemical Engineering, National Cheng
Kung University

2004.09~2005.06 **Ph.D.**, Institute of Applied Chemistry, National Chiao Tung
University 指導教授 張豐志 教授

